VOLUMETRIC ARRAY GEOMETRY DESIGN FOR DIRECTION OF ARRIVAL ESTIMATION UNDER ARRAY IMPERFECTIONS

Doktora Tezi

Fesih KESKİN

Eskişehir, 2021

VOLUMETRIC ARRAY GEOMETRY DESIGN FOR DIRECTION OF ARRIVAL ESTIMATION UNDER ARRAY IMPERFECTIONS

Fesih KESKİN

DOKTORA TEZİ

Elektrik-Elektronik Mühendisliği Anabilim Dalı
Danışman: Doç. Dr. Tansu FİLİK

Eskişehir
Eskişehir Teknik Üniversitesi
Lisansüstü Eğitim Enstitüsü
OCAK 2021

ÖZET

DİZİ KUSURLARI ALTINDA VARIŞ YÖNÜ KESTİRİMİ İÇİN HACİMSEL DİZİ GEOMETRİSİ TASARIMI

Fesih KESKİN

Elektrik-Elektronik Mühendisliği Anabilim Dalı
Telekomünikasyon Bilim Dalı
Eskişehir Teknik Üniversitesi, Lisansüstü Eğitim Enstitüsü, OCAK 2021

Danışman: Doç. Dr. Tansu FİLİK

Varış-açısı (DOA) kestirimi birkaç on yıldır kapsamlı bir şekilde incelenmiştir. DOA kestirim performansı birkaç parametreye bağlıdır. Bu parametrelerden önemli olan bazıları kaynakların sayısı, kaynakların yönü, dizideki algılayıcıların sayısı ve konumudur. Pratik DOA kestirim sistemlerinde, yakın aralıklı antenler kaçınılmaz olarak elektromanyetik ortak bağlaşıma (MC) neden olur, ve geniş aralıklı dizi elemanları açı kestirimi belirsizliğine neden olur. Ayrıca yayılan dalgaların yansıma, kırılma, kırınım ve saçılması, iyi bilinen dizi modelini bozmaktadır. Dizi kusurları olarak adlandırılabilecek olan tüm bu pratik etkiler, DOA sistemleri için zorlu konulardır. Günümüzde DOA kestirim sistemleri sadece yerde değillerdir, uçuyorlar, ve ayrıca hedefler de hareketlidirler. Bu dinamik senaryoda, hem yanca hem de yükseklik açı (yani iki boyutlu, 2-B) kestirim performansı yön-bağımsız (izotropik) olmalıdır. Yön-bağımsız diziler, tüm yanca ve yükseklik yönleri için eşit Cramer-Rao alt sınır seviyelerine sahiptir. Bu özellik sadece bazı özel hacimsel dizilerle mümkün olabilmektedir.

Bu çalışmada, yeni hacimsel (yani üç boyutlu, 3-B) algılayıcı dizi geometrisi tasarımları araştırılmış ve dizi kusurları altında analiz edilmiştir. Önerilen yöntemler 2-B yön-bağımsızlık, ortak bağlaşım ve açı belirsizliği kısıtlamaları altında minimum sayıda ek algılayıcı eklemeye dayanmaktadır. Verilen dizilere eklenecek algılayıcıların konumları ve sayıları üzerindeki kısıtlamalar analitik olarak türetilmiştir. İlk olarak, 2-B yön-bağımsız DOA kestirimi için Hacimsel V-şekilli dizilerin potansiyelleri üzerine durulmuştur.

Ardından, merkez simetrik düzlemsel diziler için daha genel bir genişletme düzeni sunulmuştur. Son olarak, 2-B yön-bağımsız DOA kestirimi için rastgele doğrusal ve düzlemsel dizilere uygulanabilen en iyi (optimum) dizi genişletme yaklaşımı önerilmiştir. Tüm bu diziler için analitik sonuçlar çeşitli benzetim sonuçlarıyla doğrulanmıştır. Ayrıca, geleceğin senaryosu olarak, gizli yayıcıların 2-B DOA kestirimi için hacimsel algılayıcı dizisi olarak uçan (dinamik) çoklu İHA'ları ele aldık. Ayrıca, geleceğin uçmakta olan DF sistemi senaryosu olarak, gizli yayıcıların 2-B DOA kestirimi için hacimsel sensör dizisi olarak birden fazla İHA'yı ele aldık.

Anahtar Sözcükler: Varış-yönü kestirimi, Dizi geometrisi tasarımı, 2-B yön-bağımsız diziler, Hacimsel diziler, Dizi sinyal işleme.

ABSTRACT

VOLUMETRIC ARRAY GEOMETRY DESIGN FOR DIRECTION OF ARRIVAL ESTIMATION UNDER ARRAY IMPERFECTIONS

Fesih KESKİN

Department of Electrical and Electronics Engineering
Programme in Telecommunication
Eskişehir Technical University, Institute of Graduate Programs, JANUARY 2021

Supervisor: Assoc. Prof. Tansu FILIK

Direction of arrival (DOA) estimation has been studied comprehensively for several decades. The DOA estimation performance depends on several parameters. Some of these important parameters are the number of sources, the direction of sources, the number and location of the sensors in the array. In practical DOA estimation systems, closely spaced antennas (sensors) inevitably cause electromagnetic mutual coupling (MC), and largely spaced array elements cause angle estimation ambiguity. Also, reflection, refraction, diffraction, and scattering of propagating waves distort the well-known array model. All these practical effects, which can be called as array imperfections, are challenging issues for DOA systems. Nowadays, DOA estimation systems are not located on the ground, they are flying, and the targets are also mobile. In this dynamic scenario, both the azimuth and elevation angles (i.e., two-dimensional, 2-D) estimation performance should be isotropic. The isotropic arrays have equal Cramér-Rao lower bound levels for all azimuth and elevation directions. This can only be possible with some special volumetric arrays.

In this study, new volumetric (i.e., three-dimensional, 3-D) sensor array geometry designs are investigated and analyzed under array imperfections. The proposed methods are based on adding a minimum number of additional sensors under constraints of 2-D isotropy, mutual coupling, and angle ambiguity. The constraints on the sensors' locations and numbers to be added over the given arrays are analytically derived. Firstly, the potentials of volumetric V-shaped arrays are considered for 2-D isotropic DOA estimation. Then more generic extension layout for centrosymmetric planar arrays is presented. Finally, an optimum array extension approach, which can be applicable to arbitrary linear and planar arrays, is proposed for 2-D isotropic DOA estimation. Analytical results have been verified with various simulation results for all these arrays. We also considered multiple UAVs as volumetric sensor array for 2-D DOA estimation of hidden emitters as the future airborne DF system scenario.

Keywords: DOA estimation, Array geometry design, 2-D isotropic arrays, Volumetric arrays, Array signal processing.

ACKNOWLEDGMENTS

First and foremost, I would like to thank my supervisor Assoc. Prof. Dr. Tansu FİLİK for his support, encouragement, guidance, and contributions throughout my Ph.D.

I would also like to thank Prof. Dr. Ömer Nezih GEREK and Assist. Prof. Dr. Gülay ÜNAL for their valuable suggestions during the whole period and for their time during the Progress Committee meetings.

Last but not least, I would like to thank my family and my lovely wife Şeyda for their support and love that keep me eager and hopeful to accomplish this dissertation.

Fesih KESKİN

25/01/2021

25/01/2021

STATEMENT OF COMPLIANCE WITH ETHICAL PRINCIPLES AND RULES

I hereby truthfully declare that this thesis is an original work prepared by me; that I have behaved in accordance with the scientific ethical principles and rules throughout the stages of preparation, data collection, analysis, and presentation of my work; that I have cited the sources of all the data and information that could be obtained within the scope of this study, and included these sources in the references section; and that this study has been scanned for plagiarism with "scientific plagiarism detection program" used by Eskişehir Technical University, and that "it does not have any plagiarism" whatsoever. I also declare that, if a case contrary to my declaration is detected in my work at any time, I hereby express my consent to all the ethical and legal consequences that are involved.

. . . .

Fesih KESKİN

TABLE OF CONTENTS

LIST OF TABLES

Page

LIST OF FIGURES

ABBREVIATIONS

1-D	One Dimensional
2-D	Two Dimensional
3-D	Three Dimensional
CRLB	Cramér Rao Lower Bound
dB	Decibel
DF	Direction Finding
DOA	Direction of Arrival
EVD	Eigen Value Decomposition
FIM	Fisher Information Matrix
GPS	Global Positioning System
LOS	Line of Sight
MC	Mutual Coupling
MIMO	Multiple-input Multiple-output
MUSIC	MUltiple SIgnal Classification
RMSE	Root Mean Squared Error
SLL	Side Lobe Level
SNR	Signal-to-Noise Ratio
UAV	Unmanned Aerial Vehicle
UCA	Uniform Circular Array
ULA	Uniform Linear Array
URA	Uniform Rectangular Array
USA	Uniform Square Array

NOMENCLATURE

$\mathbf{a}$	Vector (bold small letters)
$\mathbf{A}$	Matrix (uppercase boldface letters)
$\mathbf{A}^H$	Complex-conjugate transpose (Hermitian) of a matrix $\mathbf{A}$ or a vector $\mathbf{a}$
$\mathbf{A}^T$	Transpose of a matrix $\mathbf{A}$ or a vector $\mathbf{a}$
$\mathbf{A}^{-1}$	Inverse of a matrix $\mathbf{A}$
$\mathbf{A}_{ij}$	Element in the i^{th} row and j^{th} column of the matrix $\mathbf{A}$
$\mathbf{0}_M$	A row vector of M zeros
$\mathbf{1}_M$	A row vector of M ones
$\mathbf{I}_M$	Identity matrix of size $M \times M$
$tr\left\{\mathbf{A}\right\}$	Trace of a square matrix $\mathbf{A}$
$E\left\{\bullet\right\}$	Expectation operator
$\mathbb{C}^{M \times L}$	Space of $M \times L$-dimensional complex matrices
$\mathbb{R}^n$	Real coordinate space of dimension n
$\mathbb{R}^+$	Sets of positive real numbers
$\mathbb{Z}^+$	Sets of positive integers
$\lVert\bullet\rVert$	2-norm (Euclidean norm)
$\lceil\bullet\rceil$	Ceiling function, the smallest integer no less than the argument
$\lfloor\bullet\rfloor$	Floor function, the largest integer not greater than the argument
$x^{(u)}$	The updated version of the parameter x
ϕ	Azimuth angle
θ	Elevation angle
$\hat{x}$	Estimate of x
$\Re\left\{x\right\}$	Real part of $x \in \mathbb{C}$
$\odot$	Hadamard (or element-wise) product
j	Imaginary unit, $j^2 = -1$

1. INTRODUCTION

1.1. Motivation and Objectives

Direction of arrival (DOA) estimation is an important research field of statistical and array signal processing, which has been studied comprehensively for several decades. It has large application areas such as radar, sonar, acoustics, wireless communications, astronomy, biomedical processing, and recently moving sensors (Unmanned Aerial Vehicles (UAVs)) based applications [1–7].

In practical direction finding (DF) systems, the DOA estimation error of the unknown emitting targets is the most important performance criteria. The sensor array geometry, i.e., the number and location of the sensors in space, play a key role in the overall error performance [8]. In addition, developing the DOA estimation algorithms for optimum performance is another critical parameter [9]. In these DF systems, closely spaced antenna array elements inevitably cause electromagnetic mutual coupling (MC) between antennas. On the other hand, largely spaced array elements cause angle ambiguity. Another important effect is the reflection of the emitting sources from the objects, which is called the multi-path effect. All these practical effects, which can be called as array imperfections, are challenging issues for DF systems.

In the array signal processing literature, the primary effort has mainly focused on developing parameter (angle) estimation algorithms and calibration methods for modeling and mitigating these array imperfections. Recently, DF systems are not located on the ground, they are airborne, and the targets are also mobile. In this scenario, both the azimuth and elevation angles should be accurately and quickly estimated for all directions. This requires both azimuth and elevation isotropic DOA estimation [10]. This can only be possible with volumetric arrays [11, 12]. Therefore, it is critically important to find an optimum three dimensional (3-D), volumetric, array design approach for the best (isotropic and minimum error) 2-D DOA estimation.

The main motivation of this thesis is to find optimum volumetric array design approaches for the practical DF systems. The angle ambiguity problem [13–17], the target frequency band [10, 18], and MC effect [19–22] are jointly investigated for the 2-D isotropic DOA estimation with newly proposed 3-D arrays.

1.2. Literature Overview

Optimal array geometry design studies to improve array performance date back to the early 60s. Unz [23] noted that performance improvement could be achieved by keeping the weights constant and changing the sensor positions. The widely used sensor array geometry is Uniform Linear Array (ULA). In [24], Kumar and Branner presented an analytical method of selecting a linear array geometry for a given set of weights. It was also extended for Uniform Circular Array (UCA) and Spherical arrays in [25]. Linear arrays are easy to analyze and have low complexity. On the contrary, it has a maximum resolution capacity at broadside and zero at the end-fire directions. Linear arrays have non-isotropic performance throughout azimuth angles [26], and it is not possible to estimate both the azimuth and elevation angles using linear arrays [27].

Hence, a variety of planar,i.e., two-dimensional (2-D), array geometries have been designed and studied for several decades. The most commonly studied planar arrays are the UCA, V-shaped, L-shaped, T-shaped, Y-shaped, cross, and uniform rectangular arrays (URA) [15, 28–34]. UCA is the most widely used planar array geometry in practical DF systems. Since UCA itself is symmetric, it has isotropic (same for all directions) performance throughout azimuth angles [26, 35]. There are many efficient DOA estimation algorithms proposed for UCA configuration because of its symmetric and isotropic structure [36–38]. It is shown that the centrosymmetric arrays have both isotropic performance and Toeplitz symmetric MC matrix, which ensures efficient 2-D DOA estimation under the MC effect [39]. In [40], the sensor positions and the opening angle of the V-shaped array have been optimized by using the CRLB for both azimuth and elevation angle estimation. In [30, 31], the azimuth and elevation coupling effects are investigated to obtain the isotropic and directional angle performance for uniform and non-uniform V-shaped planar array geometries. Comparison of V-shaped array with UCA in terms of sensor position errors, source signal correlation, and MC has also been analyzed in [31]. In some cases, it is shown that the V-shaped arrays offer better performance than UCA [32, 33].

As seen, linear and planar arrays have been discussed and studied extensively in the literature. All practical DF systems use almost planar and linear arrays. But the linear and planar arrays do not span the entire 3-D space with equal DOA estimation performance. The planar arrays' elevation estimation performance is very limited [26]. Hence the volumetric array design approaches are also investigated in the literature [8,10, 15,41–43].

In [41] and [42], authors show analytical and simulation results that, besides better angle ambiguity resolution, volumetric sensor arrays have better estimation performance than planar arrays, even for a weaker aperture. It is also shown that many planar array configurations fail to distinguish the DOA of multiple source signals [10], which is known as the ambiguity problem in the literature. Likewise, in [41] and [42], a number of different planar arrays and their 3-D extension, namely, volumetric array configurations, are investigated. These configurations have been compared based on the CRLB of the array geometries. As a result, volumetric array configurations have been shown to outperform planar array configurations in the sense of 2-D DOA estimation and ambiguity resolution.

It is critically important to find the optimum volumetric array geometries for practical DF systems under array imperfections. In [44], the analytic expression of the manifold surface of a nonlinear sensor array has been studied using differential geometry. Furthermore, in [28], the authors present a framework that investigates the significance of each sensor position in a sensor array geometry based on the array manifold and its differential geometry. It is shown in [11] that for any sensor array geometry whose the auto moment-of-inertia of coordinates of sensors are equal, it can be said these arrays have 2-D isotropic DOA estimation performance. For the sensor array to be isotropic, many researchers have studied CRLB expressions that provide the necessary and sufficient conditions for the sensor array geometry and verify these conditions with some planar sensor array geometries [8,10,11,45–47]. In fact, there are several volumetric array designs that are 3-D extensions of the well-known planar arrays. Nevertheless, these designs do not have equal CRLB levels for all azimuth and elevation angles jointly. Both the azimuth and elevation isotropy can be called as fully 2-D isotropic performance. In [41], the authors examined the effect of the third dimension on the 2-D DOA estimation performance with the derived closed-form CRLB expressions for 3-D sensor arrays under both conditional and unconditional observation models. In addition, many 3-D special sensor array geometries constructed from ULAs were analyzed and compared to planar arrays with regard to 2-D isotropic performances in [41]. In [46], the authors present sensor array geometry configuration based on isotropic conditions, which are given in [11] with uncoupled direction estimation for direction-finding multiple-input multiple-output (DF MIMO) radar systems. A sensor selection strategy with adaptive array thinning for isotropic and directional sensor design based on CRLB is proposed in [47]. However, all these volumetric array designs do not have fully 2-D isotropic DOA estimation performance. In this thesis, we have the aim of designing optimum volumetric arrays with fully 2-D isotropic DOA estimation performance under array imperfections.

1.3. Thesis Overview and Contributions

In this thesis, we proposed four different array design approaches for 2-D isotropic DOA estimation. Some important practical challenges of DF systems, such as angle ambiguity and MC effects, are jointly investigated for optimum performance. The proposed 3-D arrays are analytically derived, simulated, and compared with various planar and volumetric benchmark arrays. Besides, as a final study, a 3-D moving sensor array-based swarm UAVs scenario is discussed for tracking of targets.

- In the first design method, both the opening angles between two V-shaped planar arrays and linear sub-arrays are optimized to meet the isotropy conditions using the CRLB, which takes into account the statistical coupling effect of the azimuth and elevation angle estimation [48]. Then finally, a new 3-D V-shaped sensor array with a smaller number of additional sensors is proposed for fully isotropic azimuth and elevation DOA estimation [49]. Then we investigated all the well-known centrosymmetric planar array geometries for 2-D isotropy under MC and angle ambiguity constraints [50].

- Finally, an optimum volumetric sensor array extension method is presented, which can be applicable to all arbitrary linear and planar arrays for the best 2-D isotropic DOA estimation by taking into account MC and angular ambiguity. We analytically analyze these arrays to show that the minimum number of additional sensors are used in an optimum manner. It is shown in various simulations that these arrays can be used in practical DF systems to meet the new requirements [51]. Moreover, we defined a moving (airborne) 3-D sensor array, which is a swarm of UAVs. In this scenario, the formation (geometry) and paths of multiple UAVs are optimized for the best tracking and intervention of an undesired target [52].

1.4. Organization of The Thesis

The structure of this dissertation is as follows: In Chapter 2, some fundamental tools of array signal processing for 2-D DOA estimation are provided. Besides, assumptions used throughout the thesis, DF system model, CRLB expressions, and some other DOA estimation algorithms are overviewed briefly. In Chapter 3, we briefly provide the conditions for an array to have 2-D isotropic DOA estimation performance. Then, a V-shaped volumetric sensor array is designed by combining two planar V-shaped sensor arrays to improve the estimation performance of the sources' elevation angle. This is followed by a 3D V-shaped sensor array design approach for fully 2-D isotropic DOA estimation performance. In Chapter 4, a novel method has been proposed to provide 2-D isotropic DOA estimation performance by adding additional sensors to the well-known centrosymmetric planar arrays in an analytical manner. In Chapter 5, An optimum sensor array design scheme, applicable for all arbitrary linear and planar arrays, has been proposed for 2-D DOA estimation, taking MC and angle ambiguity imperfection into account. Moreover, the effective use of 3-D sensor array-based swarm UAVs is examined in order to estimate the unwanted target's DOA and respond to it. Finally, in Chapter 6, we end with concluding remarks.

2. FUNDAMENTAL CONCEPTS OF 2-D DOA ESTIMATION

This chapter reviews the fundamental backgrounds of array signal processing for DOA estimation. The array data model is reviewed in Section 2.1. In Section 2.2, CRLB expressions, which gives the ultimate performance of an unbiased estimator, are presented for 2-D DOA estimation. Finally, the subspace-based 2-D DOA estimation algorithm, which is used as a benchmark in simulations, MUltiple SIgnal Classification (MUSIC) [53], is briefly reviewed in Section 2.3.

2.1. Array Data Model

It is more convenient to give some basic assumptions on the array elements and the signal model before introducing the array data model. In a practical DF system, isotropic sensors (antennas) that have uniform radiation patterns are used.

Far-field assumption: The source signal's radiation pattern takes various forms depending on exactly how far the region where the source signal is located is from the sensor array. These regions are often referred to as the near-field (Fresnel) region and the far-field (Fraunhofer) region, depending on the sensor's distance. For a sensor with a maximum total size of D, the following two conditions must be met for the far-field region to occur.

$$\frac{2D^2}{\lambda} < R \tag{2.1}$$

$$\lambda < D \ll R \tag{2.2}$$

where λ and R represent the wavelength and distance of the source signal to the sensor, respectively. In this study, the source signal is assumed to be in the far-field (i.e., a large distance from the sensor array). Therefore, the spherical propagating wave can be reasonably approximated as a plane wave.

Narrow-band assumption: The frequency contents of the signals are concentrated in the vicinity of the carrier frequency f_c. Namely, it has a very small bandwidth relative to the carrier angular frequency, $w_c = 2\pi f_c$.

The frequencies of the signals detected by the array elements are important as they determine the constraints on the element spacing. Aliasing may occur in analog to digital conversion when the array's sensors do not meet the Nyquist criteria at the sampling of incident signals in space, i.e., if the sensors are not close enough to each other.

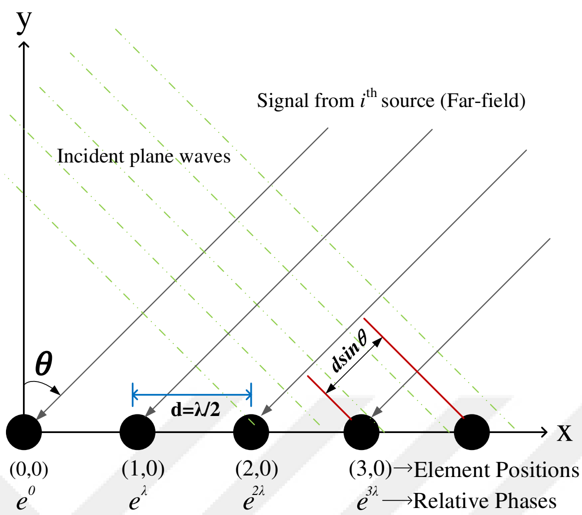

Figure 2.1: A traveling plane wave geometry regarding the array's elements and the l^{th} source signal.

Trigonometry indicates that $d\sin\theta$ is the extra distance between the sensors traveled by the incident plane, as shown in Figure 2.1. The time difference between consecutive sensors is then calculated by,

$$\tau = \frac{d}{c}\sin\theta \tag{2.3}$$

where d is inter-element spacing in terms of λ, and c denotes propagation velocity of the wave.

In order to avoid spatial aliasing, the phase difference between the spatially sampled signals should be less than or equal to π. Otherwise, if there are phase differences greater than π, incorrect time delays may occur between the received signals. To prevent this, the following condition is defined for the highest frequency of the interested narrow-band signal,

$$2\pi f_{max}\tau \leq \pi \tag{2.4}$$

Substituting (2.3) into (2.4) gives,

$$d \leq \frac{c}{2f_{max}\sin\theta} \tag{2.5}$$

For $\theta = 90°$ (i.e., end-fire), the worst delay exists, therefore we get the fundamental condition as follow,

$$d \leq \frac{\lambda_{min}}{2} \tag{2.6}$$

where $\lambda_{min} = c/f_{max}$ represents the minimum wavelength that avoids spatial aliasing.

Let assume that the message, $m\,(t)$, is modulated up to the DF system frequency. Then, the transmitted source signal, $s\,(t)$, to be estimated is narrow-band.

$$s\,(t) = m\,(t)\, e^{jw_c t} \tag{2.7}$$

The narrow-band assumption implies that the envelope, $m\,(t)$, or the amplitude varies much slower than $s\,(t)$. Therefore, for small-time delays, τ,

$$s\,(t-\tau) = m\,(t-\tau)\, e^{jw_c(t-\tau)} \approx m\,(t)\, e^{jw_c t} e^{-jw_c \tau} = s\,(t)\, e^{-jw_c \tau} \tag{2.8}$$

In the scope of this thesis, since the 2-D DOA estimation will be made under the 3-D sensor array geometries and the presence of multiple sources, the general sensor array data model will be used.

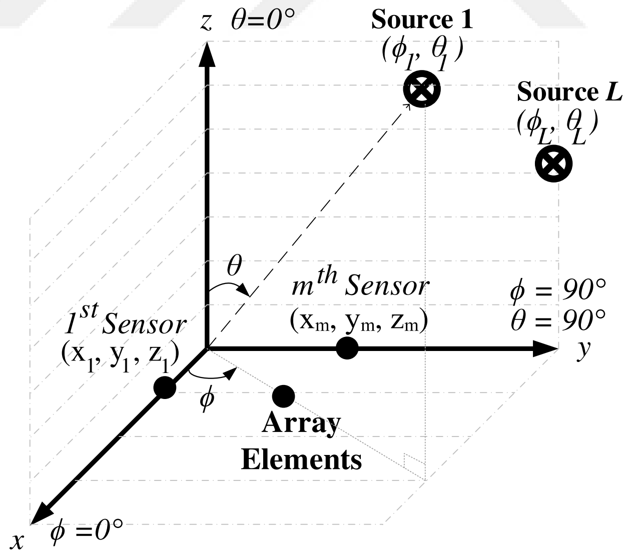

Figure 2.2: Coordinate system for 2-D DOA estimation

Throughout this thesis, unless stated otherwise, it will be assumed that a sensor array geometry consisting of isotropic and identical *M* sensors is positioned at $\mathbf{p}_m = [x_m\; y_m\; z_m]^T,\; m = 1, \ldots, M$. Further, we consider that *L* far-field and narrow-band source signals impinge on the sensor array from the directions $(\phi_l,\, \theta_l)\,,\; l = 1, \ldots, L$, where $\phi \in [0°,\ 180°]$ and $\theta \in [0°,\ 90°]$ represent azimuth and elevation angles of the source signals, respectively, as shown in Figure 2.2. Note that ϕ is measured counter-clockwise from the positive *x*-axis on the *x*-*y* plane, whilst θ is the clockwise angle made with the positive *z*-axis. In general, the sensor array output, $\mathbf{y}(t) \in \mathbb{C}^{M\times 1}$, at time t can be written as,

$$\mathbf{y}(t) = \mathbf{A}\mathbf{s}(t) + \mathbf{n}(t)\,,\ \ t = 1, \ldots, T \tag{2.9}$$

where *T* is the number of snapshots. It is assumed that the signal, $\mathbf{s}(t) \in \mathbb{C}^{L\times 1}$ and noise, $\mathbf{n}(t) \in \mathbb{C}^{M\times 1}$, are uncorrelated, zero-mean, spatially, and temporally white Gaussian complex random processes. Array manifold (steering) matrix $\mathbf{A} \in \mathbb{C}^{M\times L}$ is

$$\mathbf{A} = \left[\mathbf{a}(\phi_1, \theta_1)\,,\ \mathbf{a}(\phi_2, \theta_2)\,,\ \cdots\,,\ \mathbf{a}(\phi_L, \theta_L)\right] \tag{2.10}$$

where $\mathbf{a}(\phi_l,\ \theta_l) \in \mathbb{C}^{M\times 1}$ is the steering vector of the sensor array in direction $(\phi_l,\ \theta_l)$ as,

$$\mathbf{a}(\phi_l,\ \theta_l) = \left[e^{\left\{j\mathbf{k}_l{}^T\mathbf{p}_1\right\}}\ \ldots\ e^{\left\{j\mathbf{k}_l{}^T\mathbf{p}_M\right\}}\right]^T \tag{2.11}$$

where $\mathbf{k}_l = (2\pi f_c \mathbf{u}_l)/c = (2\pi\mathbf{u}_l)/\lambda$ is the wave-number vector of the l^{th} source in the direction $(\phi_l,\ \theta_l)$ and the unit vector pointing towards the source signal directions (ϕ_l, θ_l) is,

$$\mathbf{u}_l = \begin{bmatrix} \sin\theta_l \cos\phi_l \\ \sin\theta_l \sin\phi_l \\ \cos\theta_l \end{bmatrix} \tag{2.12}$$

The challenge is to find DOA angles, (ϕ, θ), of the given array output (2.9). Owing to the fact that the DOA angles are spatial parameters, a covariance matrix between the sensors is required. Thus, the output covariance matrix, $\mathbf{R} \in \mathbb{C}^{M\times M}$, is

$$\begin{aligned}
\mathbf{R} &= E\left\{\mathbf{y}(t)\,\mathbf{y}(t)^H\right\} = E\left\{(\mathbf{A}\mathbf{s}(t) + \mathbf{n}(t))\,(\mathbf{A}\mathbf{s}(t) + \mathbf{n}(t))^H\right\} \\
&= E\left\{(\mathbf{A}\mathbf{s}(t) + \mathbf{n}(t))\left(\mathbf{s}(t)^H\mathbf{A}^H + \mathbf{n}(t)^H\right)\right\} \\
&= E\left\{\mathbf{A}\mathbf{s}(t)\,\mathbf{s}(t)^H\mathbf{A}^H\right\} + E\left\{\mathbf{A}\mathbf{s}(t)\,\mathbf{n}(t)^H\right\} \\
&+ E\left\{\mathbf{n}(t)\,\mathbf{s}(t)^H\mathbf{A}^H\right\} + E\left\{\mathbf{n}(t)\,\mathbf{n}(t)^H\right\} \\
&= \mathbf{A}\mathbf{R}_s\mathbf{A}^H + \sigma_n^2\mathbf{I}_M
\end{aligned} \tag{2.13}$$

where σ_n^2 and $\mathbf{R}_s \in \mathbb{C}^{L\times L}$ represent noise variance and the source correlation matrix, respectively. Note that $\mathbf{R}_s$ is a diagonal matrix if the source signals are uncorrelated.

2.2. CRLB for 2-D DOA Estimation

In this section, we present a brief derivation of the CRLB, which gives the ultimate performance of any unbiased estimator whose variance matrix attains the lower bound. The variances of the azimuth and elevation angle estimators should satisfy the following inequalities, respectively.

$$var\left(\widehat{\phi}\right) \geq \left[\mathbf{F}^{-1}\right]_{11} \tag{2.14}$$

$$var\left(\widehat{\theta}\right) \geq \left[\mathbf{F}^{-1}\right]_{22} \tag{2.15}$$

where Fisher Information Matrix (FIM), $\mathbf{F}$, is given in [54] as,

$$\mathbf{F} = \begin{bmatrix} \mathbf{F}_{\phi\phi} & \mathbf{F}_{\phi\theta} \\ \mathbf{F}_{\theta\phi} & \mathbf{F}_{\theta\theta} \end{bmatrix} \tag{2.16}$$

The FIM's elements are calculated as,

$$\mathbf{F}_{\phi\phi} = T \times tr\left\{\mathbf{R}^{-1}\frac{\partial\mathbf{R}}{\partial\phi}\mathbf{R}^{-1}\frac{\partial\mathbf{R}}{\partial\phi}\right\} \tag{2.17}$$

$$\mathbf{F}_{\phi\theta} = T \times tr\left\{\mathbf{R}^{-1}\frac{\partial\mathbf{R}}{\partial\phi}\mathbf{R}^{-1}\frac{\partial\mathbf{R}}{\partial\theta}\right\} \tag{2.18}$$

where $tr\left\{\cdot\right\}$ denotes trace of the matrix. Thus,

$$\mathbf{F}_{\phi\phi} = \frac{2T}{\sigma_n^2}\Re\left\{\left(\mathbf{R}_s\mathbf{A}^H\mathbf{R}^{-1}\mathbf{A}\mathbf{R}_s\right)\odot\left(\dot{\mathbf{A}}_\phi^H\mathbf{P}_{\mathbf{A}}^{\perp}\mathbf{R}^{-1}\dot{\mathbf{A}}_\phi\right)\right\} \tag{2.19}$$

$$\mathbf{F}_{\phi\theta} = \frac{2T}{\sigma_n^2}\Re\left\{\left(\mathbf{R}_s\mathbf{A}^H\mathbf{R}^{-1}\mathbf{A}\mathbf{R}_s\right)\odot\left(\dot{\mathbf{A}}_\phi^H\mathbf{P}_{\mathbf{A}}^{\perp}\mathbf{R}^{-1}\dot{\mathbf{A}}_\theta\right)\right\} \tag{2.20}$$

where $\Re\left\{x\right\}$ denotes the real part of x and $\odot$ is the Hadamard (or element-wise) product. Note that $\mathbf{F}_{\theta\theta} \in \mathbb{C}^{L\times L}$ can be written similar to (2.19). $\mathbf{F}_{\theta\phi} = \mathbf{F}_{\phi\theta}$ and,

$$\mathbf{P}_{\mathbf{A}}^{\perp} = \mathbf{I}_M - \mathbf{A}\left(\mathbf{A}^H\mathbf{A}\right)^{-1}\mathbf{A}^H,\ \ \dot{\mathbf{A}}_\phi = \sum_{l=1}^{L}\frac{\partial\mathbf{A}}{\partial\phi_l} \tag{2.21}$$

where $\dot{\mathbf{A}}_\phi \in \mathbb{C}^{M\times L}$ and $\dot{\mathbf{A}}_\theta \in \mathbb{C}^{M\times L}$ denote the sum of derivatives of $\mathbf{A}$ regarding the l^{th} element of ϕ and θ, respectively. $\mathbf{P}_{\mathbf{A}}^{\perp} \in \mathbb{C}^{M\times M}$ represents the orthogonal projection of column space of steering matrix $\mathbf{A}$. Normalized CRLB expressions for azimuth and elevation performances are given in [11] as,

$$CRLB(\phi) = \frac{1}{J_{\phi\phi}}\left(1 - \frac{J_{\phi\theta}^2}{J_{\phi\phi}J_{\theta\theta}}\right)^{-1} \tag{2.22}$$

$$CRLB(\theta) = \frac{1}{J_{\theta\theta}}\left(1 - \frac{J_{\phi\theta}^2}{J_{\phi\phi}J_{\theta\theta}}\right)^{-1} \tag{2.23}$$

where $J_{\phi\phi} = \sqrt{tr\left\{\mathbf{F}_{\phi\phi}\right\}/L}$. $J_{\phi\theta}$, $J_{\theta\phi}$, and $J_{\theta\theta}$ can be written similarly.

2.3. The MUSIC Algorithm

In this section, we briefly give DOA estimation based on the MUSIC algorithm, which is one of the earliest and most popular DOA estimation algorithm proposed for super-resolution DF systems [55]. The basic idea behind the MUSIC algorithm is to perform Eigen Value Decomposition (EVD) for the covariance matrix (2.13) of the sensor array output (2.9). Since any signal vector, $\mathbf{a}$, in the signal subspace $\mathbf{a} \in \mathbf{S}_s$ must be orthogonal to the noise subspace $\mathbf{a} \perp \mathbf{S}_\eta$, spanning the noise subspace must be $\mathbf{a} \perp \mathbf{v}_i$ for all eigenvectors $\mathbf{v}_i,\ i = L+1,\ldots,M$. After the noise subspace has been estimated, a search is done for angle pairs in the range by searching for steering vectors that are as orthogonal to the noise subspace as possible. This is accomplished simply through a 2-D MUSIC pseudo spectrum search for *L* peaks, which is given as,

$$\mathbf{P}_{MU}\left(\phi,\theta\right) = \frac{1}{\mathbf{a}^H\left(\phi_l,\theta_l\right)\mathbf{S}_\eta\mathbf{S}_\eta^H\mathbf{a}\left(\phi_l,\theta_l\right)} \tag{2.24}$$

where $\mathbf{S}_\eta$ represents the noise subspace of the eigenvector matrix. *L* highest peaks of $\mathbf{P}_{MU}\left(\phi,\theta\right)$ will be DOA angles of source signals.

3. ARRAY DESIGN FOR 2-D ISOTROPIC DOA ESTIMATION

In recent years, the positioning and tracking of multiple mobile users for the next generation's dense radio access networks are becoming important requirements [56]. Similarly, the UAVs, also known as drones, have been a high concern for public safety. Hence the geo-localization and tracking of these drones are critical [57–59]. In all these problems, the sources are mobile. Modern DF systems are not fixed on the ground, they are also mobile. In this scenario, both the azimuth and elevation angles should be accurately and quickly estimated for all directions. This requires both azimuth and elevation isotropic DOA estimation [10]. This can only be possible with volumetric arrays [8, 11, 12, 45]. Therefore, it is critically important to find an optimum three dimensional (3-D), volumetric, array design approach for the best (isotropic and minimum error) 2-D DOA estimation.

In the following sections, we briefly give 2-D isotropic conditions for an arbitrary sensor array geometry. Then, in Section 3.2, a new V-shaped volumetric array is presented by combining two planar V-shaped arrays. Later in Section 3.3, another V-shaped volumetric array with fully 2-D isotropic DOA estimation performance is proposed by analytically adding fewer sensors.

3.1. Isotropic Arrays

In this section, we give both azimuth and elevation isotropy conditions for any given arbitrary array. We assume that any arbitrary array with M sensors is located in Cartesian coordinates as follows,

$$\mathbf{x} = [x_1\, x_2 \dots\, x_M], \quad \mathbf{y} = [y_1\, y_2 \dots\, y_M], \quad \mathbf{z} = [z_1\, z_2 \dots\, z_M] \tag{3.1}$$

In [11], Nielsen proposed that if the moment-of-inertia tensor of an array is a scalar matrix, then this array has both azimuth and elevation isotropic, which is also called in this thesis as fully 2-D isotropic, DOA estimation performance. The moment-of-inertia tensor of an array is, [60, 61],

$$\mathbf{I_p} = \begin{bmatrix} I_{xx} & I_{xy} & I_{xz} \\ I_{xy} & I_{yy} & I_{yz} \\ I_{xz} & I_{yz} & I_{zz} \end{bmatrix} \tag{3.2}$$

where $\mathbf{I_p} = c\mathbf{I}_3$, c is a constant, and $\mathbf{I}_3$ is 3×3 identity matrix [8]. Thus, 2-D isotropic constraints are, [11, 46],

$$I_{xy} = I_{xz} = I_{yz} = 0 \tag{3.3}$$

$$I_{xx} = I_{yy} = I_{zz} \tag{3.4}$$

where I_{xy}, I_{xz}, and I_{yz} represent the cross moment-of-inertia between coordinates, namely off-diagonal elements of the array's moment-of-inertia tensor and can be written by,

$$I_{xy} = \sum_{m=1}^{M} (x_m - \mu_{\mathbf{x}}) (y_m - \mu_{\mathbf{y}}) = (\mathbf{x} - \mu_{\mathbf{x}}\mathbf{1}_M) (\mathbf{y} - \mu_{\mathbf{y}}\mathbf{1}_M)^T \tag{3.5}$$

$$I_{xz} = \sum_{m=1}^{M} (x_m - \mu_{\mathbf{x}}) (z_m - \mu_{\mathbf{z}}) = (\mathbf{x} - \mu_{\mathbf{x}}\mathbf{1}_M) (\mathbf{z} - \mu_{\mathbf{z}}\mathbf{1}_M)^T \tag{3.6}$$

$$I_{yz} = \sum_{m=1}^{M} (y_m - \mu_{\mathbf{y}}) (z_m - \mu_{\mathbf{z}}) = (\mathbf{y} - \mu_{\mathbf{y}}\mathbf{1}_M) (\mathbf{z} - \mu_{\mathbf{z}}\mathbf{1}_M)^T \tag{3.7}$$

I_{xx}, I_{yy}, and I_{zz} denote the auto moment-of-inertia of x, y, and z coordinates, respectively, namely diagonal elements of the array's moment-of-inertia tensor.

$$I_{xx} = \sum_{m=1}^{M} (x_m - \mu_{\mathbf{x}})^2 = \|\mathbf{x} - \mu_{\mathbf{x}}\mathbf{1}_M\|^2 \tag{3.8}$$

$$I_{yy} = \sum_{m=1}^{M} (y_m - \mu_{\mathbf{y}})^2 = \|\mathbf{y} - \mu_{\mathbf{y}}\mathbf{1}_M\|^2 \tag{3.9}$$

$$I_{zz} = \sum_{m=1}^{M} (z_m - \mu_{\mathbf{z}})^2 = \|\mathbf{z} - \mu_{\mathbf{z}}\mathbf{1}_M\|^2 \tag{3.10}$$

where the mean of coordinates is defined by,

$$\mu_{\mathbf{x}} = \frac{1}{M}\sum_{m=1}^{M} x_m = \left(\mathbf{x}\mathbf{1}_M^T\right)/M \tag{3.11}$$

$$\mu_{\mathbf{y}} = \frac{1}{M}\sum_{m=1}^{M} y_m = \left(\mathbf{y}\mathbf{1}_M^T\right)/M \tag{3.12}$$

$$\mu_{\mathbf{z}} = \frac{1}{M}\sum_{m=1}^{M} z_m = \left(\mathbf{z}\mathbf{1}_M^T\right)/M \tag{3.13}$$

3.2. Two V-shaped Planar Arrays

In this section, a new V-shaped volumetric sensor array is designed by combining two planar V-shaped sensor arrays for improving the elevation estimation performance of the array. The planar V-shaped sensor arrays given in Figure 3.1(a) are combined as in Figure 3.1(b). In the resulting volumetric sensor array, the γ_1 and γ_2 angles between the arms of the two V-shaped planar arrays and the β angle between the planes of these planar arrays are optimized under the constraint of (3.3) and (3.4).

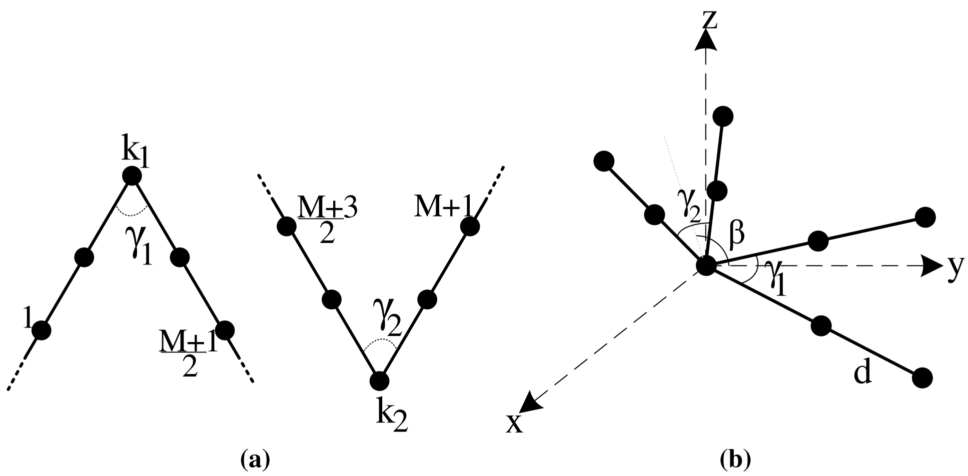

Figure 3.1: (a) The planar V-shaped arrays (b) The proposed V-shaped volumetric array

3.2.1. Design Procedure

Here, we propose a piece-wise function to create coordinates of the V-shaped volumetric sensor array. Let $M+1$, where $M = 1+4a$ and $a \in \mathbb{Z}^+$, be the total number of sensors of the two planar V-shaped arrays and, $k_1 = \frac{M+3}{4}$ and $k_2 = \frac{3M+5}{4}$ be the reference sensor index of the first and second planar V-shaped sensor arrays, respectively. Then the functions that create the sensor position of the planar sensor arrays (see Figure 3.1(a)) can be written as follows,

$$\begin{aligned} x_m &= (m - k_1)\, d \sin\left(\frac{\gamma_1}{2}\right) \\ y_m &= |m - k_1|\, d \cos\left(\frac{\gamma_1}{2}\right) \\ z_m &= 0 \qquad m = 1, \ldots, \frac{M+1}{2} \end{aligned} \tag{3.14}$$

$$\begin{aligned} x_m &= (m - k_2)\, d \sin\left(\frac{\gamma_2}{2}\right) \\ y_m &= |m - k_2|\, d \cos\left(\frac{\gamma_2}{2}\right) \cos(\beta) \\ z_m &= |m - k_2|\, d \cos\left(\frac{\gamma_2}{2}\right) \sin(\beta) \quad m = \frac{M+3}{2}, \ldots, M+1 \end{aligned} \tag{3.15}$$

Here, we optimize γ_1, γ_2, and β angles so that the new volumetric sensor array obtained by combining the functions of (3.14) and (3.15) provides isotropic constraints as given in (3.4). The mean of *x*, *y*, and *z* coordinates are derived as follows,

$$\begin{aligned} \mu_{\mathbf{x}} &= \frac{1}{M+1}\left(\sum_{m=1}^{\frac{M+1}{2}} (m - k_1)\, d\sin\left(\frac{\gamma_1}{2}\right) + \sum_{m=\frac{M+3}{2}}^{M+1} (m - k_2)\, d\sin\left(\frac{\gamma_2}{2}\right)\right) \\ &= \frac{1}{M+1}\left(d\sin\left(\frac{\gamma_1}{2}\right) \sum_{m=1}^{\frac{M+1}{2}} (m - k_1)\ + d\sin\left(\frac{\gamma_2}{2}\right) \sin(\beta) \sum_{m=\frac{M+3}{2}}^{M+1} (m - k_2)\right) \end{aligned} \tag{3.16}$$

We substitute the reference sensors index equations given in Appendix for k_1 and k_2, (A.1) and (A.2), respectively into (3.16), and we get mean of *x* coordinate as,

$$\mu_{\mathbf{x}} = 0 \tag{3.17}$$

The mean of *y* coordinates of the combined V-shaped volumetric array is,

$$\begin{aligned} \mu_{\mathbf{y}} &= \frac{1}{M+1}\left(\sum_{m=1}^{\frac{M+1}{2}} |m - k_1|\, d\cos\left(\frac{\gamma_1}{2}\right) + \sum_{m=\frac{M+3}{2}}^{M+1} |m - k_2|\, d\cos\left(\frac{\gamma_2}{2}\right) \cos(\beta)\right) \\ &= \frac{1}{M+1}\left(d\cos\left(\frac{\gamma_1}{2}\right) \sum_{m=1}^{\frac{M+1}{2}} |m - k_1|\ + d\cos\left(\frac{\gamma_2}{2}\right) \cos(\beta) \sum_{m=\frac{M+3}{2}}^{M+1} |m - k_2|\right) \end{aligned} \tag{3.18}$$

Substituting (A.3) and (A.4) into (3.18) gives,

$$\mu_{\mathbf{y}} = \frac{d\,(M-1)\,(M+3)}{16\,(M+1)}\left(\cos\left(\frac{\gamma_1}{2}\right) + \cos\left(\frac{\gamma_2}{2}\right)\cos\left(\beta\right)\right) \tag{3.19}$$

The mean of z coordinates of the combined V-shaped volumetric array is,

$$\mu_{\mathbf{z}} = \frac{1}{M+1}\sum_{m=\frac{M+3}{2}}^{M+1} |m-k_2|\, d\cos\left(\frac{\gamma_2}{2}\right)\sin\left(\beta\right) \tag{3.20}$$

Substituting (A.4) into (3.20) gives,

$$\mu_{\mathbf{z}} = \frac{1}{M+1} d\cos\left(\frac{\gamma_2}{2}\right)\sin\left(\beta\right)\frac{(M-1)\,(M+3)}{16} \tag{3.21}$$

The auto moment-of-inertia expressions for x, y, and z coordinates which depend on γ_1, γ_2, and M are obtained as follows;

$$I_{xx} = d^2\sin^2\left(\frac{\gamma_1}{2}\right)\sum_{m=1}^{\frac{M+1}{2}}(m-k_1)^2 + d^2\sin^2\left(\frac{\gamma_2}{2}\right)\sum_{m=\frac{M+3}{2}}^{M+1}(m-k_2)^2 \tag{3.22}$$

Substituting (A.5) and (A.6) into (3.22) gives,

$$I_{xx} = \frac{d^2}{96}\,(M-1)\,(M+1)\,(M+3)\left(\sin^2\left(\frac{\gamma_1}{2}\right) + \sin^2\left(\frac{\gamma_2}{2}\right)\right) \tag{3.23}$$

$$\begin{aligned} I_{yy} &= \sum_{m=1}^{M+1} {y_m}^2 + (M+1)\,{\mu_{\mathbf{y}}}^2 - 2\mu_{\mathbf{y}}\sum_{m=1}^{M+1} y_m \\ &= \sum_{m=1}^{M+1} {y_m}^2 + (M+1)\left(\frac{1}{(M+1)}\sum_{m=1}^{M+1} y_m\right)^2 - 2\frac{1}{(M+1)}\sum_{m=1}^{M+1} y_m \sum_{m=1}^{M+1} y_m \\ &= \sum_{m=1}^{M} {y_m}^2 - (M+1)\,{\mu_{\mathbf{y}}}^2 \end{aligned} \tag{3.24}$$

Substituting (A.8) and (3.19) into (3.24) gives,

$$\begin{aligned} I_{yy} = &\frac{d^2}{96}\,(M-1)\,(M+1)\,(M+3)\left(\cos^2\left(\frac{\gamma_1}{2}\right) + \cos^2\left(\frac{\gamma_2}{2}\right)\cos^2\left(\beta\right)\right) \\ &- \frac{1}{(M+1)}\left(d\cos\left(\frac{\gamma_1}{2}\right)\frac{(M-1)\,(M+3)}{16} + d\cos\left(\frac{\gamma_2}{2}\right)\cos\left(\beta\right)\frac{(M-1)\,(M+3)}{16}\right)^2 \end{aligned} \tag{3.25}$$

I_{zz} can be obtained similar to (3.24) as,

$$I_{zz} = \sum_{m=1}^{M+1} {z_m}^2 - (M+1)\, {\mu_{\mathbf{z}}}^2 \tag{3.26}$$

Substituting (A.10) and (3.21) into (3.26) gives,

$$\begin{aligned} I_{zz} = & \frac{d^2}{96}(M-1)(M+1)(M+3)\cos^2\left(\frac{\gamma_2}{2}\right)\sin^2(\beta) \\ & - \frac{1}{(M+1)}\left(d\cos\left(\frac{\gamma_2}{2}\right)\sin(\beta)\frac{(M-1)(M+3)}{16}\right)^2 \end{aligned} \tag{3.27}$$

The auto moments of *x*, *y*, and *z* coordinates obtained by (3.23), (3.25), and (3.27), respectively, are applied to (3.4) and (3.3). The angles $\gamma_1 = 58.9°$, $\gamma_2 = 58.05°$, and $\beta = 89.85°$, which approximates (3.4) and (3.3), were obtained by brute-force search. The auto and cross moment-of-inertia inequalities of this array are as follows,

$$I_{xx} \approx I_{yy} = I_{zz} \tag{3.28}$$

$$I_{xy} = I_{xz} = 0,\ I_{yz} \approx 0 \tag{3.29}$$

When the volumetric array is created with these angles obtained, the azimuth isotropy structure is not degraded. The elevation estimation performance is improved to a great extent, although it is not fully isotropic.

3.2.2. Experimental Results

In this section, performance improvements are illustrated by simulations for the designed new V-shaped volumetric array. The proposed volumetric array can be easily designed by a combination of equations (3.14) and (3.15) for a specified number of sensors, *M*. For example, if $M = 9$, then the optimum angles are obtained as $\gamma_1 = 58.9°$, $\gamma_2 = 58.05°$, and $\beta = 89.85°$, as shown in Figure 3.2.

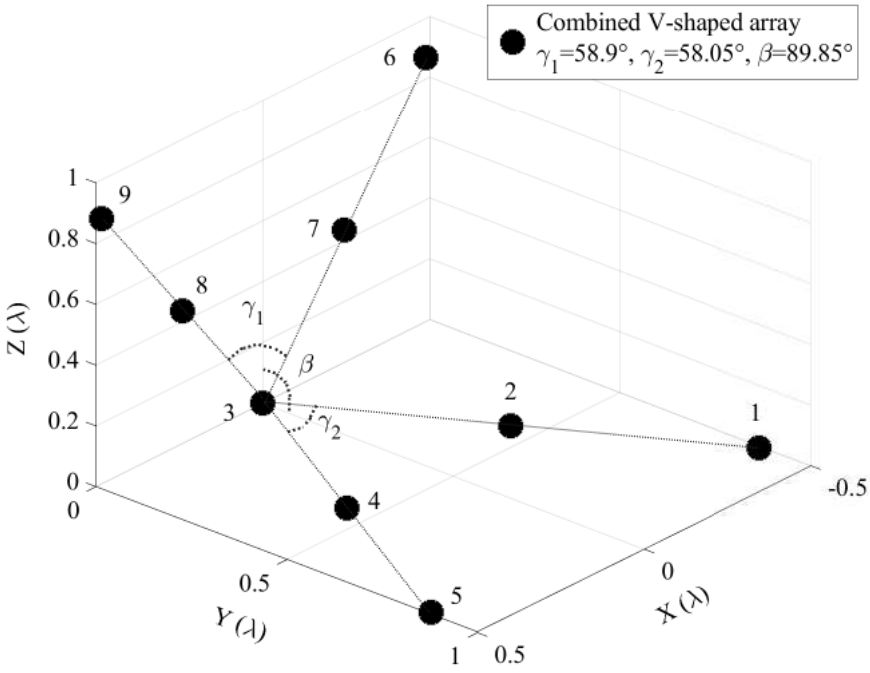

Figure 3.2: V-shaped volumetric array by combining two planar V-shaped sensor arrays

The performance of this V-shaped volumetric array is compared with the planar V-shaped array and UCA, consisting of the same number of sensors. All simulations are realized by taking the number of sensors $M = 9$ and the frequency of the source signal $f_c = 500$ MHz. CRLB values are obtained for the signal-to-noise ratio (SNR) of 20 dB. CRLB expressions given by (2.22) and (2.23) state the lower achievable error variance of the unbiased azimuth and elevation estimators, respectively [54].

While the azimuth performance of the tested array is obtained, the elevation angle of the source is kept at a certain angle, and the azimuth angle is scanned from $0°$ to $180°$. Similarly, while obtaining elevation performance, the azimuth angle of the source is kept at a certain angle, and the elevation angle is scanned from $0°$ to $90°$. Figure 3.3 shows the azimuth performance of the arrays when the elevation angle of the source is fixed at $80°$, and Figure 3.4 shows the elevation performance of the arrays when the azimuth angle of the source is fixed at $20°$.

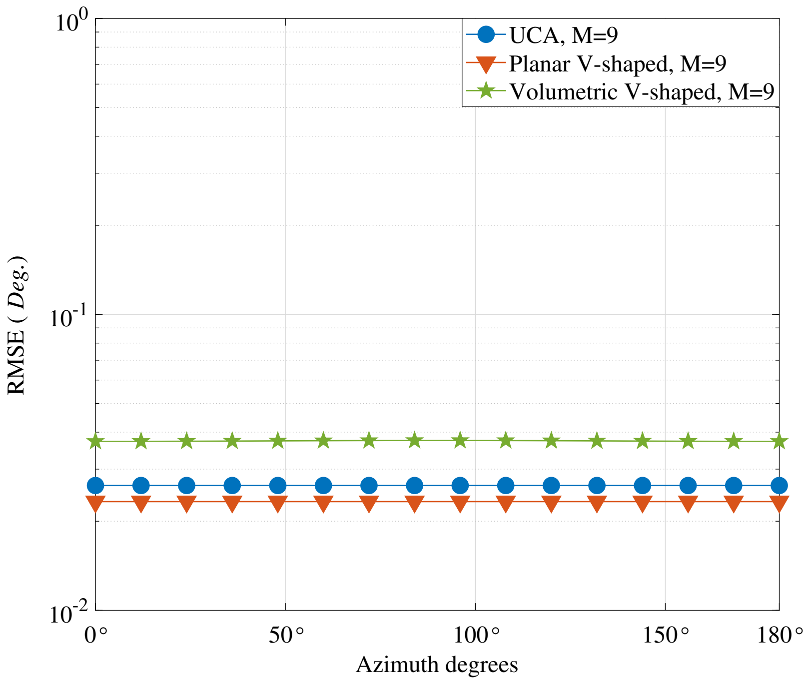

Figure 3.3: Azimuth CRLB DOA performance of UCA, Planar V-shaped, and V-shaped volumetric array for single-source when azimuth angle swept between 0° and 180° while elevation angle is fixed to 80°.

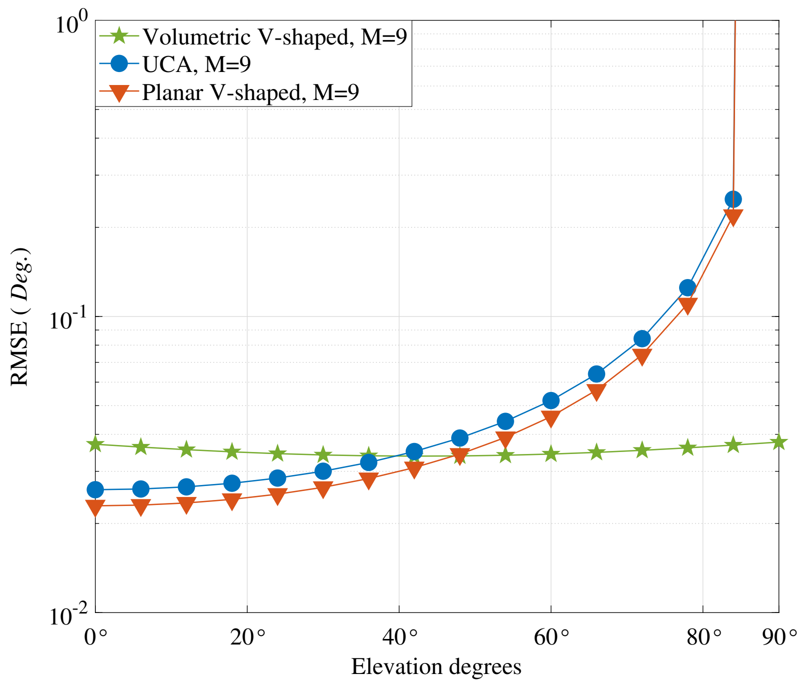

Figure 3.4: Elevation CRLB DOA performance of UCA, Planar V-shaped, and V-shaped volumetric array for single-source when elevation angle swept between 0° and 90° while azimuth angle is fixed to 20°.

In Figure 3.3, it is observed that the azimuth performance of the proposed V-shaped volumetric array is slightly worse than the UCA and planar V-shaped array. Because it has fewer sensors and hence a narrower sector on its *x-y* plane. Nevertheless, the UCA and planar V-shaped arrays have the isotropic DOA estimation performance on the azimuth angles because they hold azimuth isotropic conditions ($I_{xx} = I_{yy},\ \ I_{zz} = 0$). However, these planar arrays fail to distinguish the elevation angle after a certain elevation degree due to $I_{zz} = 0$. In addition to a small deterioration in azimuth angle estimation, an important improvement is made in elevation angle estimation for the proposed V-shaped volumetric array, as can be seen in Figure 3.4. It can be easily seen that elevation angle estimation errors go to infinity when the elevation angle approaches $90°$ for the UCA and planar V-shaped arrays. However, the proposed V-shaped volumetric array can estimate the target source for all elevation angle with almost equal CRLB levels, as shown in Figure 3.4.

3.3. V-shaped Volumetric Array Design for Fully 2-D Isotropy

In the previous section, two uniform planar V-shaped arrays are used for the 2-D isotropic volumetric array design. The three angles are optimized for both azimuth and elevation isotropic performance. But no closed-form solutions can be derived for fully 2-D isotropic performance. In this section, a new approach is proposed to design a V-shaped volumetric array, which has fully isotropic azimuth and elevation DOA estimation performance. To emphasize again, the 2-D fully isotropy conditions, which are defined in [11], both (3.3) and (3.4), should be satisfied. In this context, it should be possible to extend the existing planar arrays to provide isotropy conditions by adding new additional sensors. The proposed method results in a 3-D array by adding additional sensors on the given planar V-shaped array to hold the constraints of equalizing the auto moment-of-inertia and setting the cross moment-of-inertia to zero.

3.3.1. Design Procedure

Let the number of sensors in a given planar V-shaped array be $M = 1 + 2a$, where $a \in \mathbb{Z}^+$, and the reference sensor index is $k = \frac{M+1}{2}$. In this case, the function that creates the positions of the *d* spaced sensors in the array can be written as follows,

$$\begin{aligned} x_m &= (m-k)\, d \sin\left(\frac{\gamma}{2}\right) \\ y_m &= |m-k|\, d \cos\left(\frac{\gamma}{2}\right) \\ z_m &= 0, \qquad m = 1, \ldots, M \end{aligned} \tag{3.30}$$

Note that in our proposed V-shaped array extension method, the given planar V-shaped array does not need to be azimuth isotropic. Namely, γ does not have to be equal to γ_{iso}, which satisfies the 1-D isotropy conditions proposed in [31]. Since the given planar V-shaped sensor array geometry is on the *x*-*y* plane and symmetrical with respect to the *y*-axis, $\mu_{\mathbf{x}}$, $\mu_{\mathbf{z}}$, I_{zz}, I_{xz}, and I_{yz} will be zero. By substituting (A.11) into (3.31), we obtain the mean of *x* and *z* coordinates as,

$$\mu_{\mathbf{x}} = \frac{1}{M}\sum_{m=1}^{M}(m-k)\, d \sin\left(\frac{\gamma}{2}\right) = \frac{1}{M} d \sin\left(\frac{\gamma}{2}\right)\sum_{m=1}^{M}(m-k) = 0 \tag{3.31}$$

$$\mu_{\mathbf{z}} = 0 \tag{3.32}$$

The mean of *y* coordinate is obtained as follow,

$$\mu_{\mathbf{y}} = \frac{1}{M}\sum_{m=1}^{M}|m-k|\, d \cos\left(\frac{\gamma}{2}\right) = \frac{1}{M} d \cos\left(\frac{\gamma}{2}\right)\sum_{m=1}^{M}|m-k| \tag{3.33}$$

Substituting (A.12) into (3.33) gives,

$$\mu_{\mathbf{y}} = \frac{1}{M} d \cos\left(\frac{\gamma}{2}\right)\left\lceil \frac{M^2-1}{4} \right\rceil \tag{3.34}$$

The auto moment-of-inertia for *x*, *y*, and *z* coordinates are obtained as follows,

$$\begin{aligned} I_{xx} &= \sum_{m=1}^{M}(x_m - \mu_{\mathbf{x}})^2 = d^2 \sin^2\left(\frac{\gamma}{2}\right)\sum_{m=1}^{M}(m-k)^2 \\ &= \frac{1}{12} M \left(M^2-1\right) d^2 \sin^2\left(\frac{\gamma}{2}\right) \end{aligned} \tag{3.35}$$

$$I_{yy} = \sum_{m=1}^{M} (y_m - \mu_{\mathbf{y}})^2 = \sum_{m=1}^{M} \left(|m-k|\, d\cos\left(\frac{\gamma}{2}\right) - \frac{1}{M} d\cos\left(\frac{\gamma}{2}\right) \sum_{m=1}^{M} |m-k| \right)^2$$
$$= d^2 \cos^2\left(\frac{\gamma}{2}\right) \left(\frac{1}{12} M \left(M^2 - 1\right) - \frac{1}{M} \left\lceil \frac{M^2-1}{4} \right\rceil^2 \right) \tag{3.36}$$

$$I_{zz} = \sum_{m=1}^{M} (z_m - \mu_{\mathbf{z}})^2 = 0 \tag{3.37}$$

Owing to the fact that the mean of the *y* coordinates of the sensors in the array is not zero (see (3.34)). Therefore to obtain a centrosymmetric structure, the following procedure is applied to make the mean of *y* coordinates of the updated sensor array zero by adding *N* new additional sensors whose *y* coordinates are d_y. Let us suppose that the *y* coordinates of *M* sensors of the given planar V-shaped array is,

$$\mathbf{y} = [y_1, y_2, \ldots, y_M] \tag{3.38}$$

If the *y* coordinates of the added *N* sensors are d_y, then the *y* coordinates of the updated sensor array are,

$$\mathbf{y}^{(u)} = [y_1, y_2, \ldots, y_M, d_y \mathbf{1}_N] \tag{3.39}$$

where $(\bullet)^{(u)}$ represents the updated parameter. In order for the mean of the updated *y* coordinates to be zero as a result of the added sensors, d_y is obtained as follows,

$$\mu_{y^{(u)}} = \frac{1}{M+N} \sum_{m=1}^{M+N} y_m^{(u)} = \frac{1}{M+N} \left(\sum_{m=1}^{M} y_m + \sum_{m=1}^{N} d_y \right) \tag{3.40}$$

Substitute (3.39) into (3.40) and recall (3.13) as $\sum_{m=1}^{M} y_m = M\mu_{\mathbf{y}}$, then equate to zero,

$$\mu_{y^{(u)}} = \frac{M\mu_{\mathbf{y}} + N d_y}{M+N} = 0 \tag{3.41}$$

$$d_y = -\frac{M\mu_{\mathbf{y}}}{N} \tag{3.42}$$

Thus, the auto moment-of-inertia of the *y* coordinates will also be updated due to the added sensors. The coordinates of the sensors added on the *y*-axis can be generated by the substitution of (3.42) into (3.39). The auto moment-of-inertia of *y* coordinates of the given planar V-shaped array is,

$$
\begin{aligned}
I_{yy} &= \sum_{m=1}^{M} \left(y_m - \mu_{\mathbf{y}}\right)^2 = \left(y_1 - \mu_{\mathbf{y}}\right)^2 + \cdots + \left(y_M - \mu_{\mathbf{y}}\right)^2 \\
&= {y_1}^2 + \cdots + {y_M}^2 - 2\mu_{\mathbf{y}} \left(y_1 + \cdots + y_M\right) + M{\mu_{\mathbf{y}}}^2
\end{aligned} \tag{3.43}
$$

The auto moment-of-inertia of the updated *y* coordinates is obtained by,

$$
I_{yy}^{(u)} = \sum_{m=1}^{M} \left(y_m^{(u)} - \mu_{y^{(u)}}\right)^2, \;\; where\; \mu_{y^{(u)}} = 0 \tag{3.44}
$$

$$
\begin{aligned}
I_{yy}^{(u)} &= {y_1}^2 + {y_2}^2 + \cdots + {y_M}^2 + N{d_y}^2 \\
&= I_{yy} + 2\mu_{\mathbf{y}} \left(y_1 + y_2 + \cdots + y_M\right) - M{\mu_{\mathbf{y}}}^2 + N{d_y}^2 \\
&= I_{yy} + 2\mu_{\mathbf{y}} \sum_{m=1}^{M} |m-k|\, d\cos\left(\frac{\gamma}{2}\right) - M{\mu_{\mathbf{y}}}^2 + N{d_y}^2
\end{aligned} \tag{3.45}
$$

Substituting (3.34), (3.36), and (3.42) into (3.45) gives,

$$
\begin{aligned}
I_{yy}^{(u)} &= N\left(\frac{M\mu_{\mathbf{y}}}{N}\right)^2 + I_{yy} + 2M{\mu_{\mathbf{y}}}^2 - M{\mu_{\mathbf{y}}}^2 = \left(\frac{M^2}{N} + M\right){\mu_{\mathbf{y}}}^2 + I_{yy} \\
&= \left(\frac{M^2}{N} + M\right)\frac{1}{M^2} d^2\cos^2\left(\frac{\gamma}{2}\right)\left\lceil\frac{M^2-1}{4}\right\rceil^2 \\
&+ d^2\cos^2\left(\frac{\gamma}{2}\right)\left(\frac{1}{12}M\left(M^2-1\right) - \frac{1}{M}\left\lceil\frac{M^2-1}{4}\right\rceil^2\right) \\
&= d^2\cos^2\left(\frac{\gamma}{2}\right)\left(\frac{1}{N}\left\lceil\frac{M^2-1}{4}\right\rceil^2 + \frac{1}{12}M\left(M^2-1\right)\right)
\end{aligned} \tag{3.46}
$$

The *x* and *z* coordinates of the *N* sensors added to ensure $I_{xx}^{(u)} = I_{yy}^{(u)} = I_{zz}^{(u)}$, and keep the mean of *x* and *z* coordinates at zero are updated as follows.

$$
\mathbf{x}^{(u)} = \left[x_1, x_2, \ldots, x_M, d_x\mathbf{1}_{\frac{N}{2}}, -d_x\mathbf{1}_{\frac{N}{2}}\right] \tag{3.47}
$$

$$
\mathbf{z}^{(u)} = \left[z_1, z_2, \ldots, z_M, d_z(-1)^i\right], \;\; i = 1, 2, \ldots, N \tag{3.48}
$$

In order to hold the $I_{xx}^{(u)} = I_{yy}^{(u)} = I_{zz}^{(u)}$ condition while still keeping the cross moment-of-inertia at zero, we should update the *x* and *z* coordinates of the added sensors as in (3.47) and (3.48). Now we bring the auto moment-of-inertia of *x* and *z* to the $I_{yy}^{(u)}$ by updating the *x* and *z* coordinates of the added sensors. Accordingly, the auto moment-of-inertia of the *x* and *z* coordinates will be updated as follows,

$$I_{xx}^{(u)} = {x_1}^2 + {x_2}^2 + \cdots + {x_M}^2 + N{d_x}^2 = I_{xx} + N{d_x}^2 \tag{3.49}$$

$$I_{xx} + N{d_x}^2 = I_{yy}^{(u)} \tag{3.50}$$

where d_x is,

$$d_x = \sqrt{\frac{I_{yy}^{(u)} - I_{xx}}{N}} \tag{3.51}$$

The auto moment-of-inertia of the *z* coordinate, $I_{zz}^{(u)}$, and inter-element spacing on the *z*-axis, d_z, can be written similarly as (3.49)-(3.51) just by replacing the subscript *x* with *z*. Thus,

$$d_z = \sqrt{\frac{I_{yy}^{(u)} - I_{zz}}{N}} \tag{3.52}$$

The coordinates of the sensors added on *x* and *z*-axes can be generated by substituting (3.51) and (3.52) into (3.47) and (3.48), respectively. In fact, here, (3.51) and (3.52) give the inter-element sensor spacing that will increase the auto moments-of-inertia of the *x* and *z* coordinates to the auto moments-of-inertia of the *y* coordinates. Thus, the volumetric array obtained as a result of the procedure will fulfill the 2-D isotropy conditions given in (3.3) and (3.4). Table 3.1 presents the distance between array elements for the proposed V-shaped volumetric array. The mutual coupling between two sensors depends on the array element spacing. The coupling coefficient's magnitude decreases as the array element spacing increases. Consequently, the MC between two sufficiently far apart array elements (i.e., $\lambda \leq d$) can generally be assumed to be zero. Table 3.2 is built on this assumption. In other words, when the distance between the sensors is equal or larger than a wavelength, the MC coefficient is taken as zero. Since the proposed V-shaped volumetric array's MC matrix has a complex circulant matrix with a Toeplitz banded structure (see Table 3.2), the proposed array suits many MC compensation algorithms presented in the literature [39].

Table 3.1: Distance between sensors for $M = 5$, $N = 4$ elements V-shaped volumetric array (Figure 3.7) in terms of λ.

3-D V-shaped	*1st*	*2nd*	*3rd*	*4th*	*5th*	*6th*	*7th*	*8th*	*9th*
1st	0	0.5	1	0.83	0.935	2.272	2.272	1.87	1.87
2nd	0.5	0	0.5	0.467	0.83	1.846	1.846	1.605	1.605
3rd	1	0.5	0	0.5	1	1.47	1.47	1.47	1.47
4th	0.83	0.467	0.5	0	0.5	1.605	1.605	1.846	1.846
5th	0.935	0.83	1	0.5	0	1.87	1.87	2.272	2.272
6th	2.272	1.846	1.47	1.605	1.87	0	1.926	1.778	2.622
7th	2.272	1.846	1.47	1.605	1.87	1.926	0	2.622	1.778
8th	1.87	1.605	1.47	1.846	2.272	1.778	2.622	0	1.926
9th	1.87	1.605	1.47	1.846	2.272	2.622	1.778	1.926	0

Table 3.2: Mutual coupling matrix for $M = 5$, $N = 4$ elements V-shaped volumetric array.

3-D V-shaped	*1st*	*2nd*	*3rd*	*4th*	*5th*	*6th*	*7th*	*8th*	*9th*
1st	1	v_1	0	v_3	v_4	0	0	0	0
2nd	v_1	1	v_1	v_2	v_3	0	0	0	0
3rd	0	v_1	1	v_1	0	0	0	0	0
4th	v_3	v_2	v_1	1	v_1	0	0	0	0
5th	v_4	v_3	0	v_1	1	0	0	0	0
6th	0	0	0	0	0	1	0	0	0
7th	0	0	0	0	0	0	1	0	0
8th	0	0	0	0	0	0	0	1	0
9th	0	0	0	0	0	0	0	0	1

In simulations, it is found that the proposed V-shaped volumetric array performs better than planar and other designed V-shaped volumetric arrays in the literature. In the following section, the performance comparisons of the arrays are provided.

3.3.2. Experimental Results

In this section, the improvements in the 2-D DOA estimation performance of the planar V-shaped array, which has been expanded analytically to make a fully isotropic array in both azimuth and elevation DOA estimation by adding new sensors, are shown with the simulation results by using the azimuth and elevation CRLB expressions given in (2.22) and (2.23), respectively.

The proposed fully isotropic V-shaped volumetric sensor array's performance is compared to the planar V-shaped array given in [31], the volumetric V-shaped given in [41], and the volumetric V-shaped array that we proposed in Section 3.2. In [31], the authors optimized the sensor positions and the opening angle of the V-shaped array to obtain the only azimuth isotropic DOA performance for a uniform planar V-shaped array, as shown in Figure 3.5.

In [41], the authors designed a 3-D V-shaped array with two symmetric orthogonal branches on the z-axis, as shown in Figure 3.6, to improve elevation estimation of the single far-field source signal. In the previous section, we designed a V-shaped volumetric array by combining two planar V-shaped sensor arrays, as shown in Figure 3.2. Since the sensor array given in Figure 3.5 is planar, it has only azimuth isotropic DOA estimation performance. When the elevation angle increases, it fails to estimate the elevation DOA of the source signals. On the other hand, there is an improvement in the elevation DOA estimation performance as new sensors are added to the z-axis of the sensor arrays given in the previous section and [41], as shown in Figures 3.2 and 3.6, respectively. However, the disadvantage of these arrays is that both sensor array designs do not fully fulfill the isotropy conditions. In contrast to these designs, our proposed V-shaped volumetric array design (Figure 3.7) that we have obtained analytically provides fully 2-D isotropic performance.

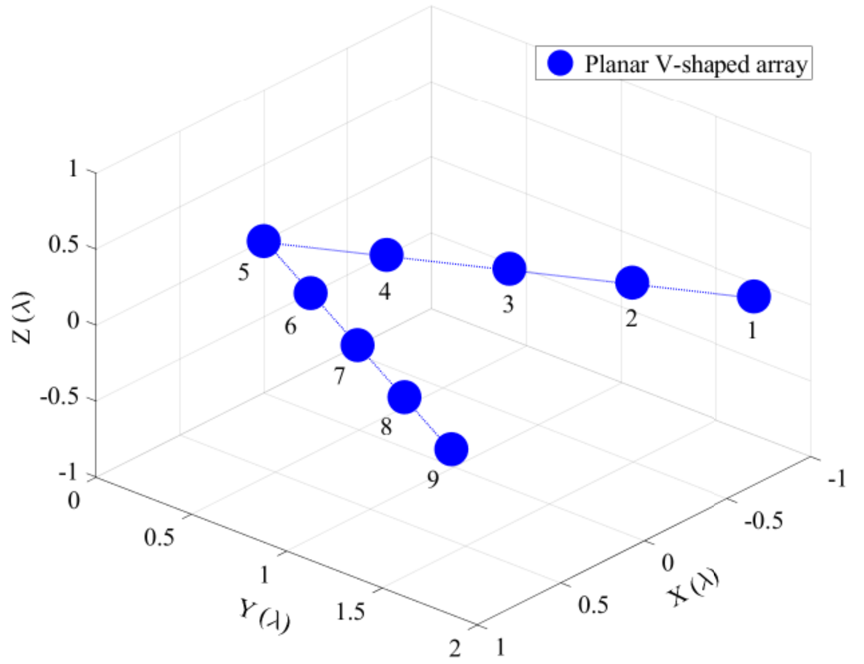

Figure 3.5: 1-D isotropic planar V-shaped array [31]

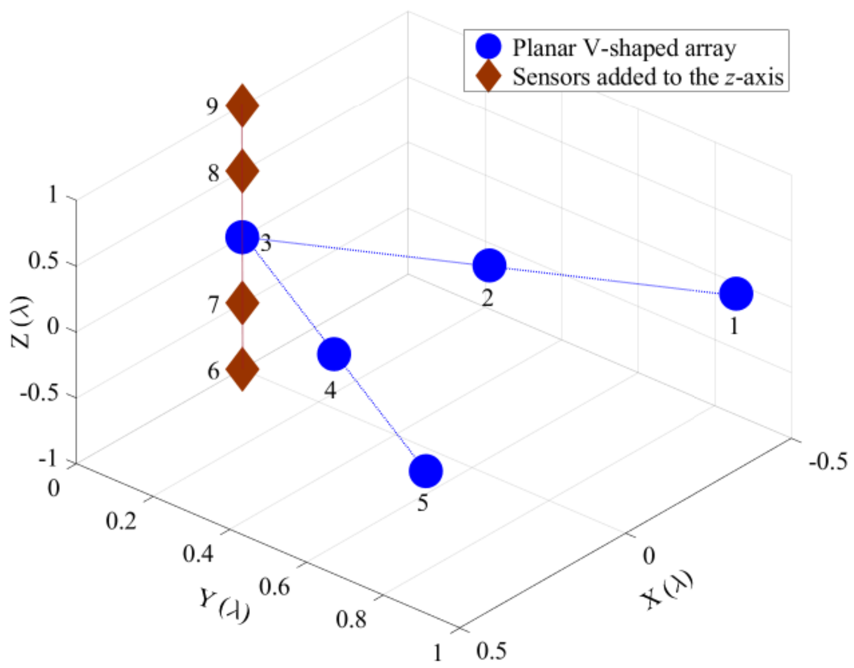

Figure 3.6: 3-D V-shaped array with orthogonal branch [41]

In order to show the effectiveness of the proposed sensor array, computer simulations are done. For this purpose, simulations are realized by taking the overall number of sensors $M = 9$. The operating frequency of the single far-field source signal is $f_c = 500$ MHz, and the corresponding wavelength is $\lambda = 0.6$ m. CRLB values are obtained for the 256 snapshots (i.e., $T = 256$) and SNR of 20 dB. Note that all the sensors have an isotropic pattern.

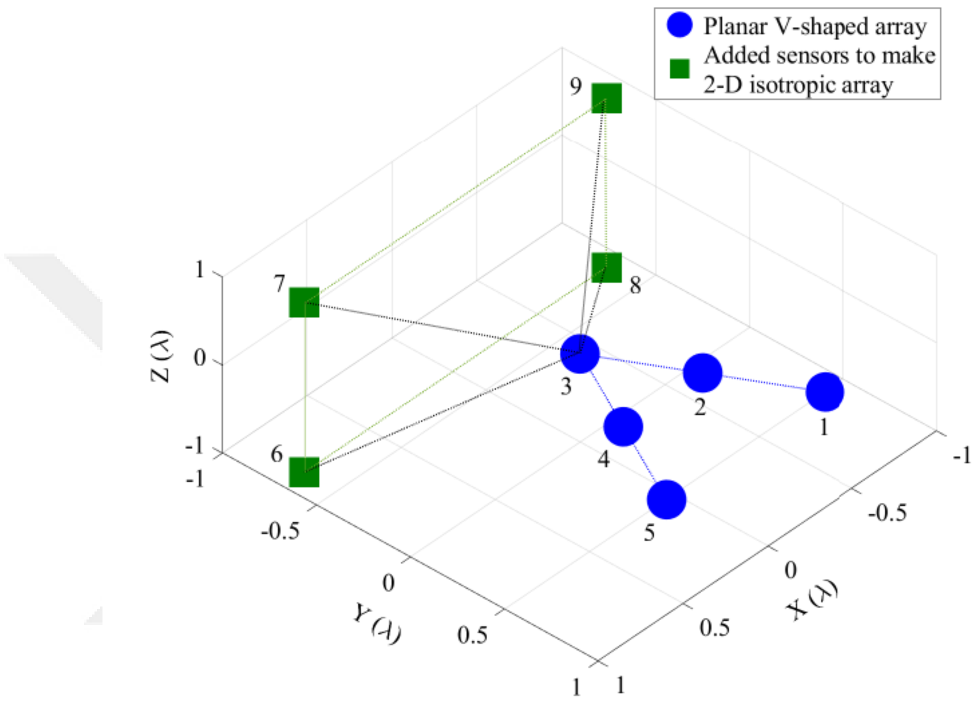

Figure 3.7: The proposed V-shaped volumetric sensor array

Azimuth and elevation DOA estimation performance comparison of planar V-shaped array (Figure 3.5) proposed in [31], 3-D V-shaped array (Figure 3.6) proposed in [41], V-shaped volumetric array that we proposed in the previous section (Figure 3.2), and the proposed fully isotropic V-shaped volumetric array (Figure 3.7) is made as shown in Figure 3.8 and 3.9, respectively.

As can be seen in Figure 3.8, the proposed 3-D sensor array has the best isotropic azimuth performance. Note that although we added sensors to an already azimuth isotropic planar V-shaped array, it continues to provide azimuth isotropy conditions with the lowest CRLB level. On the other hand, azimuth isotropy conditions are violated if sensors are added only to orthogonal branches of the planar V-shaped array as proposed in [41]. For planar arrays, as the source's elevation angle increases toward $90°$, the elevation DOA estimation error gradually worsens towards infinity, as shown in Figure 3.9. On the other hand, one can see that the elevation isotropy conditions could not be fulfilled only by adding sensors to orthogonal branches of the planar V-shaped array as proposed in [41] or the combination of the two V-shaped arrays as proposed in the previous section.

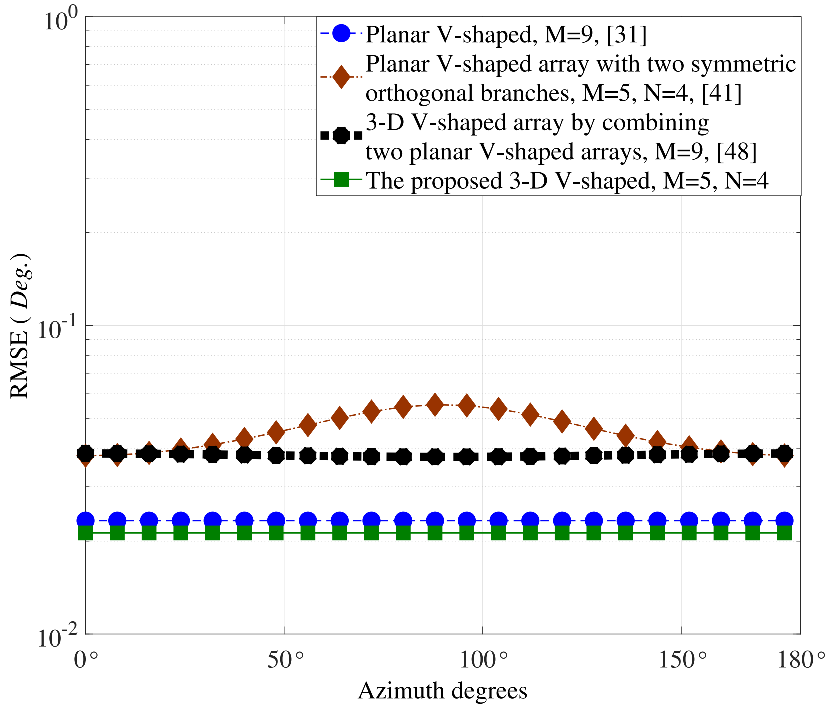

Figure 3.8: Azimuth CRLB DOA performance of Planar V-shaped [31], 3-D V-shaped with two symmetric orthogonal branches [41], V-shaped volumetric by combining two planar V-shaped, and the proposed V-shaped volumetric arrays for single-source when azimuth angle swept between 0° and 180° while elevation angle is fixed to 80°.

Although the 3-D V-shaped arrays proposed in [41] and the V-shaped volumetric array proposed in the previous section improve the elevation DOA estimation performance over the planar arrays, they can not perform fully isotropic DOA estimation performances. Contrary to these arrays, the proposed V-shaped volumetric sensor array has isotropic elevation DOA estimation performance with a lower CRLB level, as shown in Figure 3.9.

Figure 3.10 shows the 2-D DOA performance comparison for different SNR levels when the single-source at $\phi = 20°, \theta = 80°$. Both azimuth and elevation DOA performances are presented in this figure. It is shown that the proposed array is able to estimate both azimuth and elevation angles better than others.

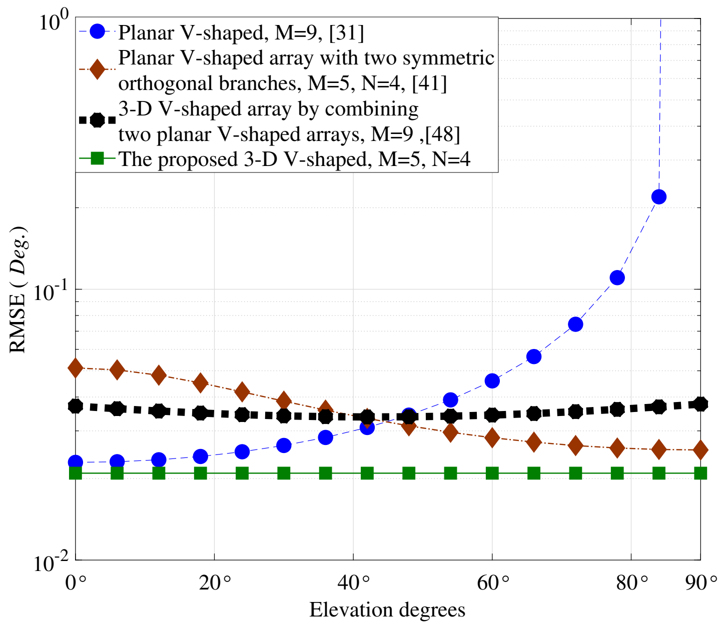

Figure 3.9: Elevation CRLB DOA performance of Planar V-shaped [31], 3-D V-shaped with two symmetric orthogonal branches [41], V-shaped volumetric by combining two planar V-shaped, and the proposed V-shaped volumetric arrays for single-source when elevation angle swept between $0°$ and $90°$ while azimuth angle is fixed to $20°$.

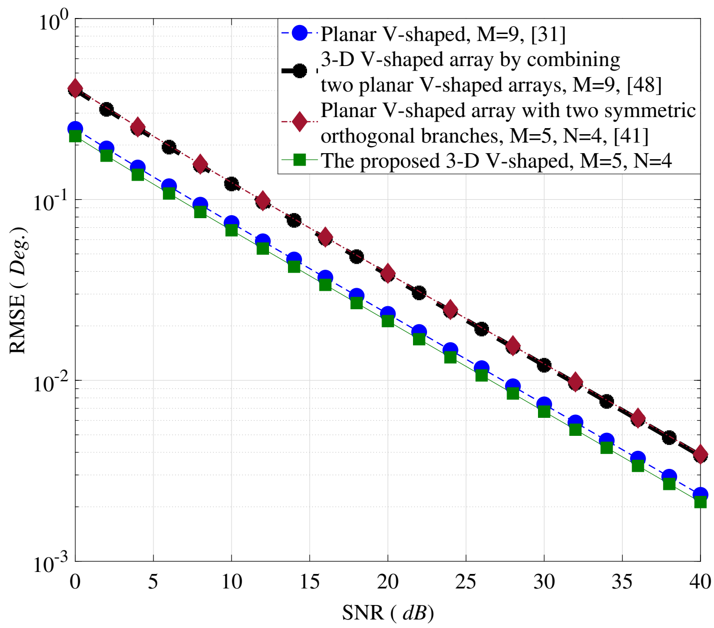

Figure 3.10: SNR CRLB 2-D DOA performance of Planar V-shaped [31], 3-D V-shaped with two symmetric orthogonal branches [41], V-shaped volumetric by combining two planar V-shaped, and the proposed V-shaped volumetric arrays for single-source at $(\phi = 80°, \theta = 20°)$.

4. CENTROSYMMETRIC VOLUMETRIC ARRAY DESIGN

In this chapter, some well-known planar array geometries, which are symmetrical to both the *x* and *y*-axes, are considered. These arrays already have azimuth isotropic performance [11] and are called as centrosymmetric arrays. It is aimed to make these arrays fully 2-D isotropic by adding the minimum number of sensors. We try to find closed-form sensor locations, which will transform centrosymmetric planar arrays into a 3-D array with 2-D isotropic DOA estimation performance.

An arbitrary centrosymmetric planar array with M sensors is assumed to be positioned on the *x*-*y* plane as,

$$\mathbf{x} = [x_1\, x_2 \ldots\, x_M], \quad \mathbf{y} = [y_1\, y_2 \ldots\, y_M], \quad \mathbf{z} = [\mathbf{0}_M] \tag{4.1}$$

Since planar arrays are assumed to be on the *x*-*y* plane, $\mu_{\mathbf{z}}, I_{zz}, I_{xz}$, and I_{yz} are zero. Note that I_{xy} is also zero for linear and centrosymmetric planar arrays. In [11], it has been proven that a planar array has azimuth isotropic performance if it holds the following conditions.

$$I_{xx} = I_{yy}, \;\; I_{zz} = 0 \tag{4.2}$$

$$I_{xy} = I_{xz} = I_{yz} = 0 \tag{4.3}$$

The conditions given in (3.3) and (3.4) should be satisfied while keeping the center of gravity of the array same. The only way is to add sensors on the *z*-axis, which should be symmetrical about the origin and located with equal d_z distances along the *z*-axis. Moreover, adding new additional sensors symmetrically to the origin ensures that the MC matrix structure of the array remains Toeplitz symmetric after the centrosymmetric planar arrays are extended to the volumetric arrays. Therefore, with these Toeplitz symmetric structures, it will still be possible to find 2-D DOA estimation without estimating unknown mutual coupling coefficients [39]. This is an important advantage for the practical DF systems. The MC matrix structure of the proposed volumetric arrays is analyzed and presented in Section 4.4.

We locate N sensors symmetrically with respect to the origin and with equal d_z

distances along the *z*-axis.

$$
\begin{aligned}
I_{zz} &= \sum_{m=1}^{M+N} (z_m - \mu_{\mathbf{z}})^2 = \sum_{m=1}^{M+N} {z_m}^2 \\
&= \left(-\frac{N-1}{2} d_z\right)^2 + \cdots + (-2d_z)^2 + (-d_z)^2 + 0 \\
&+ {d_z}^2 + (2d_z)^2 + \cdots + \left(\frac{N-1}{2} d_z\right)^2
\end{aligned}
\tag{4.4}
$$

By using Sums of Squares of Consecutive Integers formula, we obtain,

$$
2\sum_{i=1}^{\frac{N+1}{2}} \left(\frac{N-(2i-1)}{2}\right)^2 {d_z}^2 = \frac{1}{12} N \left(N^2 - 1\right) {d_z}^2 \tag{4.5}
$$

In order to make I_{zz} equal to I_{xx} or I_{yy}, sensor spacing d_z on the *z*-axis should be as follow,

$$
I_{zz} = \frac{1}{12} N \left(N^2 - 1\right) {d_z}^2 = I_{xx} \tag{4.6}
$$

$$
d_z = \sqrt{\frac{I_{xx}}{\frac{1}{12} N \left(N^2 - 1\right)}} \tag{4.7}
$$

Then the coordinates of the *N* sensor added on the *z*-axis can be generated by,

$$
\begin{aligned}
x_{i+M} &= 0 \\
y_{i+M} &= 0 \\
z_{i+M} &= \left(\frac{(N+1)}{2} - i\right) d_z \quad i = 1, \ldots, N
\end{aligned}
\tag{4.8}
$$

Since the given centrosymmetric arrays are already azimuth isotropic, they hold (3.3). After adding new sensors by substituting (4.7) into (4.8), the obtained arrays become both azimuth and elevation isotropic. One should note that the proposed array extension approach adds those new sensors symmetrical about the origin, as can be seen in (4.8). Hence, although the auto moments-of-inertia are equalized after extension, the cross moments-of-inertia will remain at zero.

This method satisfies all planar arrays that are symmetrical to both the *x* and *y*-axes, given on the *x*-*y* plane. In the following sections, there will be examples of well-known planar arrays that satisfy the proposed method. In order to apply the proposed method to these given arrays, we propose novel functions that generate their coordinates. After that, we will obtain the moment-of-inertia tensor matrix elements of the given arrays using these functions generated for each array through the equations given in Section 3.1. Then we add new sensors with the array extension method found as in (4.7) and (4.8). We extended UCA, USA, and Uniform Cross Array analytically, respectively. It is also shown by simulations that new these extended 3-D arrays provide 2-D isotropic performance. The mutual coupling structure of these 3-D arrays is also analyzed and presented.

4.1. 3-D Extension of Uniform Circular Array (UCA)

Let M be the number of sensors on planar UCA and N be the number of sensors on the orthogonal branch (z-axis). Then, we can express the sensor position of UCA (see Figure 4.1) as,

$$\alpha = \frac{2\pi}{M}, \ \ r = \frac{d}{\sqrt{2\left(1-\cos\alpha\right)}} \tag{4.9}$$

$$\begin{aligned} x_m &= r\cos\left(\left(m-1\right)\alpha\right) \\ y_m &= r\sin\left(\left(m-1\right)\alpha\right), \quad m = 1,\ldots,M \\ z_m &= 0 \end{aligned} \tag{4.10}$$

Since UCA itself has a symmetrical structure, it has isotropic performance across all azimuth angles and holds azimuth isotropy conditions (4.2) and (4.3). Evaluating the terms between (3.8) and (3.10) for this array given by (4.10), it is found as in Appendix B.1.2 the auto moment-of-inertia for *x*, *y*, and *z* coordinates as follows,

$$I_{xx} = \frac{1}{8}d^2 M\csc^2\left(\frac{\pi}{M}\right) \tag{4.11}$$

$$I_{yy} = \frac{1}{8}d^2 M\csc^2\left(\frac{\pi}{M}\right) \tag{4.12}$$

$$I_{zz} = 0 \tag{4.13}$$

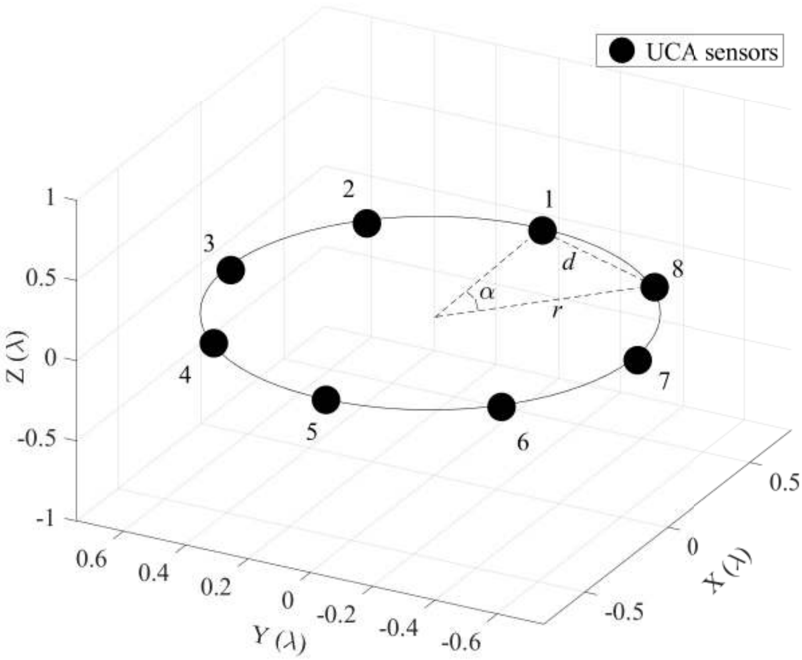

Figure 4.1: Centrosymmetric UCA.

where the mean of *x*, *y*, and *z* coordinates are found in Appendix B.1.1 as follows,

$$\mu_{\mathbf{x}} = \frac{1}{M}\sum_{m=1}^{M} \frac{d\cos\left(\frac{2\pi(m-1)}{M}\right)}{\sqrt{2\left(1-\cos\left(\frac{2\pi}{M}\right)\right)}} = 0 \tag{4.14}$$

$$\mu_{\mathbf{y}} = \frac{1}{M}\sum_{m=1}^{M} \frac{d\sin\left(\frac{2\pi(m-1)}{M}\right)}{\sqrt{2\left(1-\cos\left(\frac{2\pi}{M}\right)\right)}} = 0 \tag{4.15}$$

$$\mu_{\mathbf{z}} = 0 \tag{4.16}$$

In order to satisfy (3.4), let assume that we locate N sensors symmetrically with respect to the origin and with equal d_z distances along the *z*-axis as (4.8) to make I_{zz} equal to I_{xx}. Thus, substitute (4.11) into the proposed (4.7) as,

$$d_z = \sqrt{\frac{\frac{1}{8}d^2 M \csc^2\left(\frac{\pi}{M}\right)}{\frac{1}{12}N\left(N^2-1\right)}} = d\sqrt{\frac{3M}{2N\left(N^2-1\right)}}\csc\left(\frac{\pi}{M}\right) \tag{4.17}$$

The coordinates of the sensors added on the *z*-axis can be generated by (4.8) with

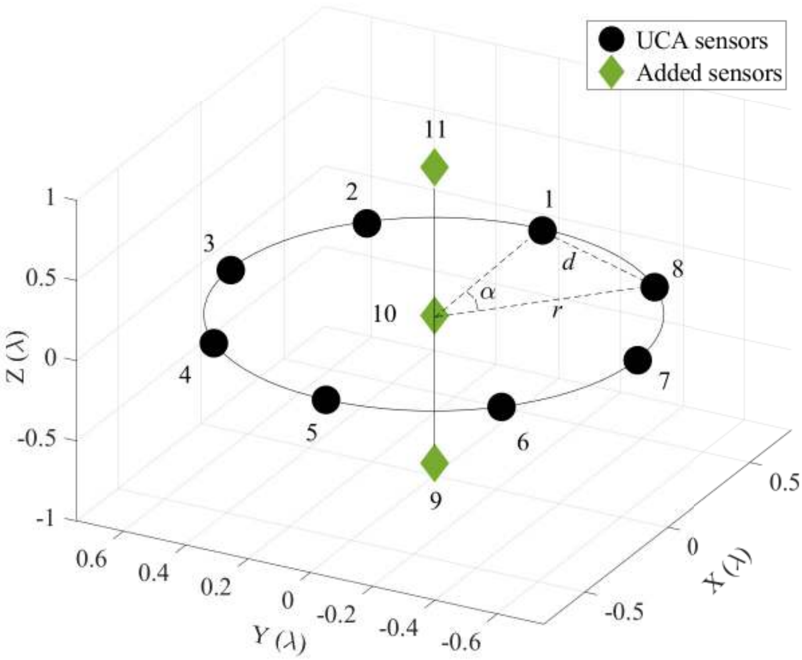

Figure 4.2: The proposed 3-D UCA.

calculated d_z in (4.17), as shown in Figure 4.2. Since we add sensors on the z-axis symmetrically about the origin, $\mu_{\mathbf{x}}$, $\mu_{\mathbf{y}}$, I_{xx}, and I_{yy} will not change. $\mu_{\mathbf{z}}$ will remain zero, and I_{zz} will be equal to I_{xx}. After some computational efforts detailed in Appendix B.1.3 and B.1.4, the mean and auto moment-of-inertia of the z-axis will be as follows,

$$\mu_{\mathbf{z}} = \frac{1}{M+N} \sum_{i=1}^{N} \left(d \left(\frac{(N+1)}{2} - i \right) \sqrt{\frac{3M}{2N\left(N^2-1\right)}} \csc\left(\frac{\pi}{M}\right) \right) = 0 \tag{4.18}$$

$$I_{zz} = \sum_{i=1}^{N} \left(d \left(\frac{(N+1)}{2} - i \right) \sqrt{\frac{3M}{2N\left(N^2-1\right)}} \csc\left(\frac{\pi}{M}\right) \right)^2 = \frac{1}{8} d^2 M \csc^2\left(\frac{\pi}{M}\right) \tag{4.19}$$

Now the new 3-D extension of UCA has 2-D isotropic DOA estimation performance since (4.19) is equal to (4.11) and (4.12). Therefore new array geometry holds both (3.3) and (3.4).

4.2. 3-D Extension of Uniform Square Array (USA)

We also apply the proposed extension approach to another popular centrosymmetric array, USA. Let M be a square number of sensors on planar USA and $u_d = \frac{\sqrt{M}-1}{2}$ be a unit distance of two neighbor sensors on the planar array. Then, we can express the sensor positions of USA (see Figure 4.3) with *d* distances as,

$$
\begin{aligned}
x_m &= \left(-u_d + m - 1 - \left(\left\lfloor \frac{m-1}{\sqrt{M}} \right\rfloor \sqrt{M}\right)\right) d \\
y_m &= \left(u_d - \left\lfloor \frac{m-1}{\sqrt{M}} \right\rfloor\right) d, \qquad m = 1, \ldots, M \\
z_m &= 0
\end{aligned}
\tag{4.20}
$$

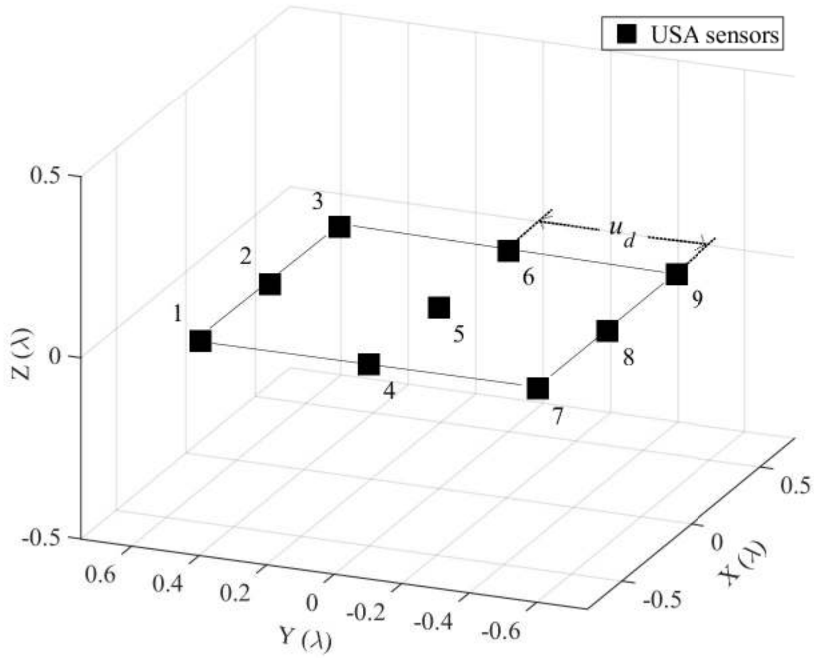

Figure 4.3: Centrosymmetric USA.

Since USA holds (4.2) and (4.3) conditions, it has azimuth isotropic performance for a square number M. The mean of *x*, *y*, and *z* coordinates are zero (without proof, but conjectured because of numerical evidence) as follows,

$$\mu_{\mathbf{x}} = \frac{1}{M} \sum_{m=1}^{M} \left(-u_d + m - 1 - \left(\left\lfloor \frac{m-1}{\sqrt{M}} \right\rfloor \sqrt{M}\right)\right) d = 0 \tag{4.21}$$

$$\mu_{\mathbf{y}} = \frac{1}{M} \sum_{m=1}^{M} \left(u_d - \left\lfloor \frac{m-1}{\sqrt{M}} \right\rfloor\right) d = 0 \tag{4.22}$$

$$\mu_{\mathbf{z}} = 0 \tag{4.23}$$

where the auto moment-of-inertia for *x*, *y*, and *z* coordinates are as follows,

$$I_{xx} = d^2 \sum_{m=1}^{M} \left(-u_d + m - 1 - \left(\left\lfloor \frac{m-1}{\sqrt{M}} \right\rfloor \sqrt{M} \right) \right)^2 = \frac{1}{12} d^2 M \left(M - 1 \right) \tag{4.24}$$

$$I_{yy} = d^2 \sum_{m=1}^{M} \left(u_d - \left\lfloor \frac{m-1}{\sqrt{M}} \right\rfloor \right)^2 = \frac{1}{12} d^2 M \left(M - 1 \right) \tag{4.25}$$

$$I_{zz} = 0 \tag{4.26}$$

In order to satisfy (3.3) and (3.4), we locate N sensors symmetrically with respect to the origin and with equal d_z distances along the *z*-axis to make I_{zz} equal to I_{xx}. If we substitute (4.24) into (4.7), we get the d_z sensor spacing as,

$$d_z = \sqrt{\frac{\frac{1}{12} d^2 M \left(M - 1 \right)}{\frac{1}{12} N \left(N^2 - 1 \right)}} = d \sqrt{\frac{M \left(M - 1 \right)}{N \left(N^2 - 1 \right)}} \tag{4.27}$$

The coordinates of the sensors added on the *z*-axis can be generated by (4.8) with found d_z in (4.27), as shown in Figure 4.4. The mean and auto moment-of-inertia of the *z*-axis will be as follows,

$$\mu_{\mathbf{z}} = \frac{1}{M+N} \sum_{i=1}^{N} \left(d \left(\frac{(N+1)}{2} - i \right) \sqrt{\frac{M \left(M - 1 \right)}{N \left(N^2 - 1 \right)}} \right) = 0 \tag{4.28}$$

$$I_{zz} = \sum_{i=1}^{N} \left(d \left(\frac{(N+1)}{2} - i \right) \sqrt{\frac{M \left(M - 1 \right)}{N \left(N^2 - 1 \right)}} \right)^2 = \frac{1}{12} d^2 M \left(M - 1 \right) \tag{4.29}$$

In the end, the new 3-D extended USA becomes both azimuth and elevation isotropic since it holds both (3.3) and (3.4).

4.3. 3-D Extension of Uniform Cross Array

Another important centrosymmetric planar array is the Uniform Cross Array. We also analyzed this array to extend the volumetric version for 2-D isotropic DOA estimation. Let $M = 1 + 4a$, where $a \in \mathbb{Z}^+$, be the number of sensors of the uniform cross array and $k = \frac{M+1}{2}$ be the reference sensor number. We can then propose a function states the

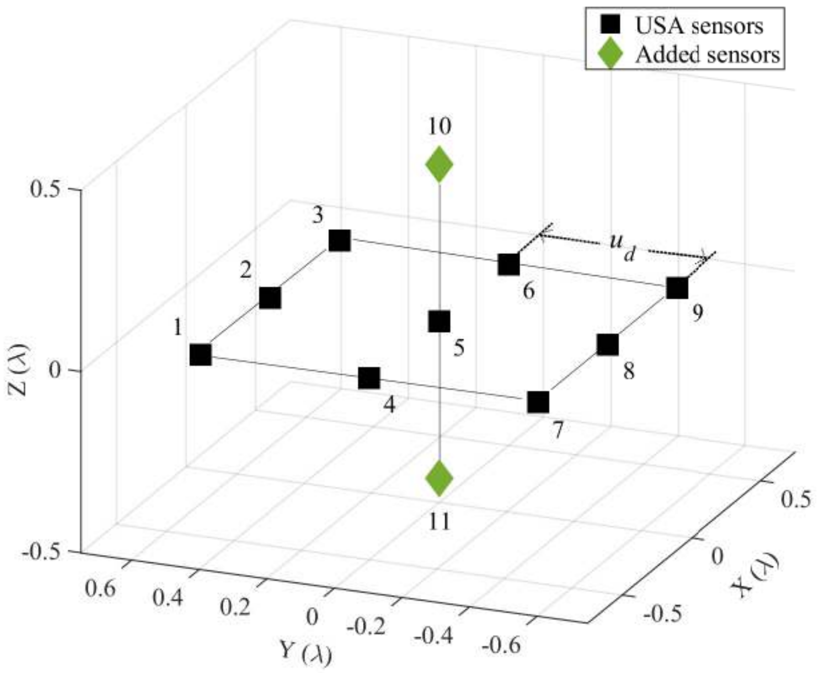

Figure 4.4: The proposed 3-D USA.

sensor positions on the planar (see Figure 4.5) with d distances as,

$$\begin{aligned} x_m &= (-1)^m \left\lceil \frac{|m-k|}{2} \right\rceil \frac{d}{\sqrt{2}}, \\ y_m &= (-1)^{\lceil \frac{m}{k} \rceil} \left\lceil \frac{|m-k|}{2} \right\rceil \frac{d}{\sqrt{2}}, \quad m = 1, \ldots, M \\ z_m &= 0 \end{aligned} \tag{4.30}$$

The cross array has azimuth isotropic performance as it holds (4.2) and (4.3) conditions. And the mean of its coordinates are zero as follows,

$$\mu_{\mathbf{x}} = \frac{1}{M} \sum_{m=1}^{M} (-1)^m \left\lceil \frac{|m-k|}{2} \right\rceil \frac{d}{\sqrt{2}} = 0 \tag{4.31}$$

$$\mu_{\mathbf{y}} = \frac{1}{M} \sum_{m=1}^{M} (-1)^{\lceil \frac{m}{k} \rceil} \left\lceil \frac{|m-k|}{2} \right\rceil \frac{d}{\sqrt{2}} = 0 \tag{4.32}$$

$$\mu_{\mathbf{z}} = 0 \tag{4.33}$$

The closed-form expressions of the auto moment-of-inertia for x, y, and z coordi-

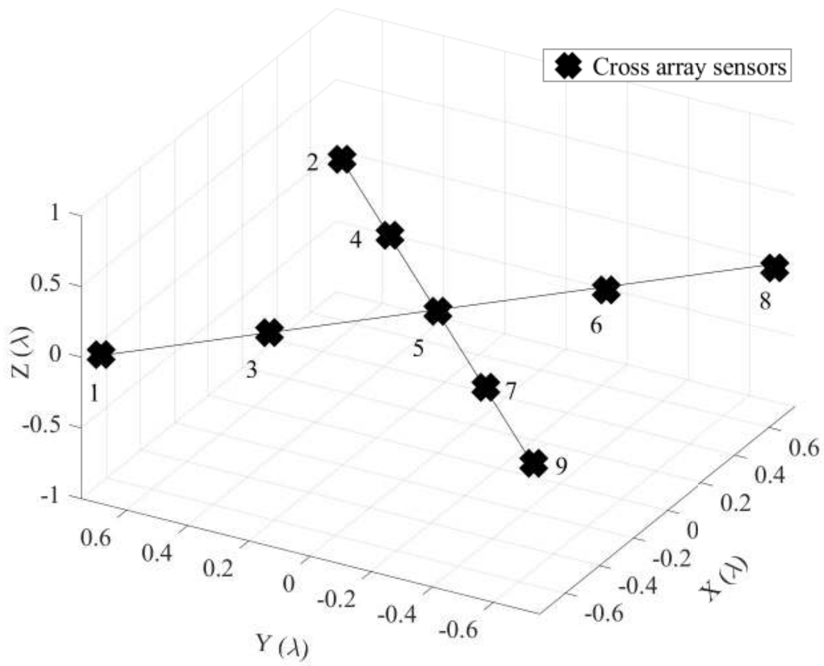

Figure 4.5: Centrosymmetric Cross array.

nates are as follows,

$$I_{xx} = \frac{d^2}{2}\sum_{m=1}^{M}\left((-1)^m\left\lceil\frac{|m-k|}{2}\right\rceil\right)^2 = \frac{1}{96}d^2\left(M-1\right)\left(M+1\right)\left(M+3\right) \tag{4.34}$$

$$I_{yy} = \frac{d^2}{2}\sum_{m=1}^{M}\left((-1)^{\left\lceil\frac{m}{k}\right\rceil}\left\lceil\frac{|m-k|}{2}\right\rceil\right)^2 = \frac{1}{96}d^2\left(M-1\right)\left(M+1\right)\left(M+3\right) \tag{4.35}$$

$$I_{zz} = 0 \tag{4.36}$$

Now if we substitute back (4.34) into (4.7), we get the d_z sensor spacing as,

$$d_z = d\sqrt{\frac{1}{8}\frac{\left(M-1\right)\left(M+1\right)\left(M+3\right)}{N\left(N^2-1\right)}} \tag{4.37}$$

The mean and auto moment-of-inertia of the z-axis of the 3-D Cross array will be as follows,

$$\mu_{\mathbf{z}} = \frac{1}{M+N}\sum_{m=1}^{M+N} z_m = \frac{1}{M+N}\sum_{i=1}^{N}\left(\left(\frac{(N+1)}{2}-i\right)\sqrt{\frac{I_{xx}}{\frac{1}{12}N\left(N^2-1\right)}}\right) = 0 \tag{4.38}$$

$$I_{zz} = \sum_{m=1}^{N} \left(\left(\frac{(N+1)}{2} - i \right) \sqrt{\frac{I_{xx}}{\frac{1}{12} N \left(N^2 - 1\right)}} \right)^2 = \frac{1}{96} d^2 \left(M-1\right)\left(M+1\right)\left(M+3\right) \tag{4.39}$$

Finally, (4.39) became equal to (4.34). Therefore, the new 3-D Cross array becomes both azimuth and elevation isotropic because it holds both (3.3) and (3.4).

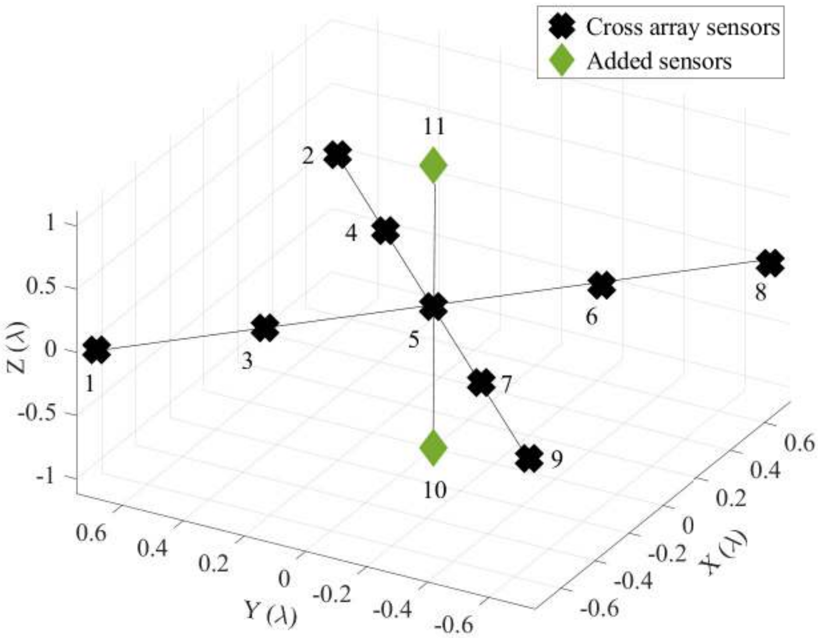

Figure 4.6: The proposed 3-D Cross array.

In the following section, we analyze the elevation ambiguity and MC effect in terms of *M* and *N* for the proposed 3-D arrays.

4.4. Elevation Ambiguity and MC Analysis

In practical DF systems, the spacing between array elements is chosen as less than a half-wavelength of the upper (biggest) frequency of the propagating target signals. This is a prerequisite to avoid angular ambiguity, but this does not always guarantee ambiguity free DOA estimation in practical DF systems. In our approach, the number of sensors added to the *z*-axis does not affect the azimuth ambiguity, it greatly affects the elevation ambiguity. Therefore, one can find that in order to avoid the elevation angle ambiguity problem, the distance between the sensors added to the *z*-axis must be less than a wavelength for the proposed sensor arrays. By choosing a wavelength of the distance between the added sensors, the distance of the $+d_z$ and $-d_z$ sensors on the z-axis to the sensor on the center satisfies the condition of half-wavelength. In addition to the ambiguity problem, the MC effect can not be neglected as the distance between sensors decreases due to the increase of N. If we choose N too small, the elevation ambiguity problem arises when the inter-element spacing of the sensors increases too much. Contrarily, if we choose N too large, the sensors on the z-axis will be very close to each other. Hence, when the inter-element spacing is less than $\lambda/4$, the unknown MC effect occurs on the array, and the assumed array model will be distorted. Due to this unknown MC distortion, the DOA estimation will be affected, and it is not possible to come near to CRLB. In this case, the selection of N is a very critical design parameter. In order to avoid angle ambiguity and MC effect, the number of the sensors added to the orthogonal branch of a centrosymmetric planar array must hold the following condition,

$$\frac{\lambda}{4} \leq d_z \leq \lambda, \quad \text{where } d = \frac{\lambda}{2} \tag{4.40}$$

As mentioned above, the unknown MC between array elements heavily affects DOA estimation performance, especially for the closely located compact arrays. There are a considerable number of studies in the literature for the accurate estimation of DOA angles in the presence of unknown MC [20, 22, 27, 38, 39, 62–64]. The MC coefficients are inversely proportional to array elements' spacing (see Tables 4.1–4.6). Consequently, the MC between two sufficiently far apart array elements (i.e., $\lambda \leq d$) can generally be assumed to be zero. Since the proposed volumetric arrays' MC matrices have a complex circulant matrix with a banded Toeplitz structure (see Tables 4.2,4.4, and 4.6), this makes the proposed arrays suitable for DOA estimation algorithms in [20, 22, 27, 38, 39, 62–64], which take the advantage of the symmetric electromagnetic coupling structure. Note that, in the MC matrices given in the tables, those with the distance between sensors greater than a wavelength are left empty since it is assumed that there is no MC effect between them.

Table 4.1: Distance between sensors for $M = 8$, $N = 3$ elements 3-D UCA in terms of λ.

3-D UCA	1^{st}	2^{nd}	3^{rd}	4^{th}	5^{th}	6^{th}	7^{th}	8^{th}	9^{th}	10^{th}	11^{th}
1^{st}	0	0.5	0.923	1.207	1.306	1.207	0.923	0.5	1.131	0.653	1.131
2^{nd}	0.5	0	0.5	0.923	1.207	1.306	1.207	0.923	1.131	0.653	1.131
3^{rd}	0.923	0.5	0	0.5	0.923	1.207	1.306	1.207	1.131	0.653	1.131
4^{th}	1.207	0.923	0.5	0	0.5	0.923	1.207	1.306	1.131	0.653	1.131
5^{th}	1.306	1.207	0.923	0.5	0	0.5	0.923	1.207	1.131	0.653	1.131
6^{th}	1.207	1.306	1.207	0.923	0.5	0	0.5	0.923	1.131	0.653	1.131
7^{th}	0.923	1.207	1.306	1.207	0.923	0.5	0	0.5	1.131	0.653	1.131
8^{th}	0.5	0.923	1.207	1.306	1.207	0.923	0.5	0	1.131	0.653	1.131
9^{th}	1.131	1.131	1.131	1.131	1.131	1.131	1.131	1.131	0	0.923	1.847
10^{th}	0.653	0.653	0.653	0.653	0.653	0.653	0.653	0.653	0.923	0	0.923
11^{th}	1.131	1.131	1.131	1.131	1.131	1.131	1.131	1.131	1.847	0.923	0

Table 4.2: Mutual coupling matrix for $M = 8$, $N = 3$ elements 3-D UCA.

3-D UCA	1^{st}	2^{nd}	3^{rd}	4^{th}	5^{th}	6^{th}	7^{th}	8^{th}	9^{th}	10^{th}	11^{th}
1^{st}	1	c_1	c_2				c_2	c_1		c_3	
2^{nd}	c_1	1	c_1	c_2				c_2		c_3	
3^{rd}	c_2	c_1	1	c_1	c_2					c_3	
4^{th}		c_2	c_1	1	c_1	c_2				c_3	
5^{th}			c_2	c_1	1	c_1	c_2			c_3	
6^{th}				c_2	c_1	1	c_1	c_2		c_3	
7^{th}	c_2				c_2	c_1	1	c_1		c_3	
8^{th}	c_1	c_2				c_2	c_1	1		c_3	
9^{th}									1	c_2	
10^{th}	c_3	c_3	c_3	c_3	c_3	c_3	c_3	c_3	c_2	1	c_2
11^{th}										c_2	1

Table 4.3: Distance between sensors for $M = 9$, $N = 2$ elements 3-D USA in terms of λ.

3-D USA	1^{st}	2^{nd}	3^{rd}	4^{th}	5^{th}	6^{th}	7^{th}	8^{th}	9^{th}	10^{th}	11^{th}
1^{st}	0	0.5	1	0.5	0.707	1.118	1	1.118	1.414	1.118	1.118
2^{nd}	0.5	0	0.5	0.707	0.5	0.707	1.118	1	1.118	1	1
3^{rd}	1	0.5	0	1.118	0.707	0.5	1.414	1.118	1	1.118	1.118
4^{th}	0.5	0.707	1.118	0	0.5	1	0.5	0.707	1.118	1	1
5^{th}	0.707	0.5	0.707	0.5	0	0.5	0.707	0.5	0.707	0.866	0.866
6^{th}	1.118	0.707	0.5	1	0.5	0	1.118	0.707	0.5	1	1
7^{th}	1	1.118	1.414	0.5	0.707	1.118	0	0.5	1	1.118	1.118
8^{th}	1.118	1	1.118	0.707	0.5	0.707	0.5	0	0.5	1	1
9^{th}	1.414	1.118	1	1.118	0.707	0.5	1	0.5	0	1.118	1.118
10^{th}	1.118	1	1.118	1	0.866	1	1.118	1	1.118	0	1.732
11^{th}	1.118	1	1.118	1	0.866	1	1.118	1	1.118	1.732	0

Table 4.4: Mutual coupling matrix for $M = 9$, $N = 2$ elements 3-D USA.

3-D USA	1^{st}	2^{nd}	3^{rd}	4^{th}	5^{th}	6^{th}	7^{th}	8^{th}	9^{th}	10^{th}	11^{th}
1^{st}	1	s_1		s_1	s_2						
2^{nd}	s_1	1	s_1	s_2	s_1	s_2					
3^{rd}		s_1	1		s_2	s_1					
4^{th}	s_1	s_2		1	s_1		s_1	s_2			
5^{th}	s_2	s_1	s_2	s_1	1	s_1	s_2	s_1	s_2	s_3	s_3
6^{th}		s_2	s_1		s_1	1		s_2	s_1		
7^{th}				s_1	s_2		1	s_1			
8^{th}				s_2	s_1	s_2	s_1	1	s_1		
9^{th}					s_2	s_1		s_1	1		
10^{th}					s_3					1	
11^{th}					s_3						1

Table 4.5: Distance between sensors for $M = 9$, $N = 2$ elements 3-D Cross array in terms of λ.

3-D Cross	*1st*	*2nd*	*3rd*	*4th*	*5th*	*6th*	*7th*	*8th*	*9th*	*10th*	*11th*
1st	0	1.414	0.5	1.118	1.0	1.5	1.118	2.0	1.414	1.5	1.5
2nd	1.414	0	1.118	0.5	1.0	1.118	1.5	1.414	2.0	1.5	1.5
3rd	0.5	1.118	0	0.707	0.5	1.0	0.707	1.5	1.118	1.224	1.224
4th	1.118	0.5	0.707	0	0.5	0.707	1.0	1.118	1.5	1.224	1.224
5th	1.0	1.0	0.5	0.5	0	0.5	0.5	1.0	1.0	1.118	1.118
6th	1.5	1.118	1.0	0.707	0.5	0	0.707	0.5	1.118	1.224	1.224
7th	1.118	1.5	0.707	1.0	0.5	0.707	0	1.118	0.5	1.224	1.224
8th	2.0	1.414	1.5	1.118	1.0	0.5	1.118	0	1.414	1.5	1.5
9th	1.414	2.0	1.118	1.5	1.0	1.118	0.5	1.414	0	1.5	1.5
10th	1.5	1.5	1.224	1.224	1.118	1.224	1.224	1.5	1.5	0	2.236
11th	1.5	1.5	1.224	1.224	1.118	1.224	1.224	1.5	1.5	2.236	0

Table 4.6: Mutual coupling matrix for $M = 9$, $N = 2$ elements 3-D Cross array.

3-D Cross	*1st*	*2nd*	*3rd*	*4th*	*5th*	*6th*	*7th*	*8th*	*9th*	*10th*	*11th*
1st	1		x_1								
2nd		1		x_1							
3rd	x_1		1	x_2	x_1		x_2				
4th		x_1	x_2	1	x_1	x_2					
5th			x_1	x_1	1	x_1	x_1				
6th				x_2	x_1	1	x_2	x_1			
7th			x_2		x_1	x_2	1		x_1		
8th						x_1		1			
9th							x_1		1		
10th										1	
11th											1

In the following parts, we present the trade-off between *M* and *N* for the proposed 3-D arrays.

4.4.1. *M* and *N* Trade-off for 3-D UCA

In order to obtain a trade-off between *M* and *N* for UCA, (4.17) is substituted into (4.40) as follows,

$$\frac{d}{2} \leq d\sqrt{\frac{3M}{2N\left(N^2-1\right)}}\csc\left(\frac{\pi}{M}\right) \leq 2d \tag{4.41}$$

thus,

$$\frac{N\left(N^2-1\right)}{6} \leq 3M\csc^2\left(\frac{\pi}{M}\right) \leq \frac{8N\left(N^2-1\right)}{3}, \quad \text{where } 2 \leq M \text{ and } 2 \leq N \tag{4.42}$$

The graphical representation of the trade-off between M and N for 3-D UCA is given in Figure 4.7.

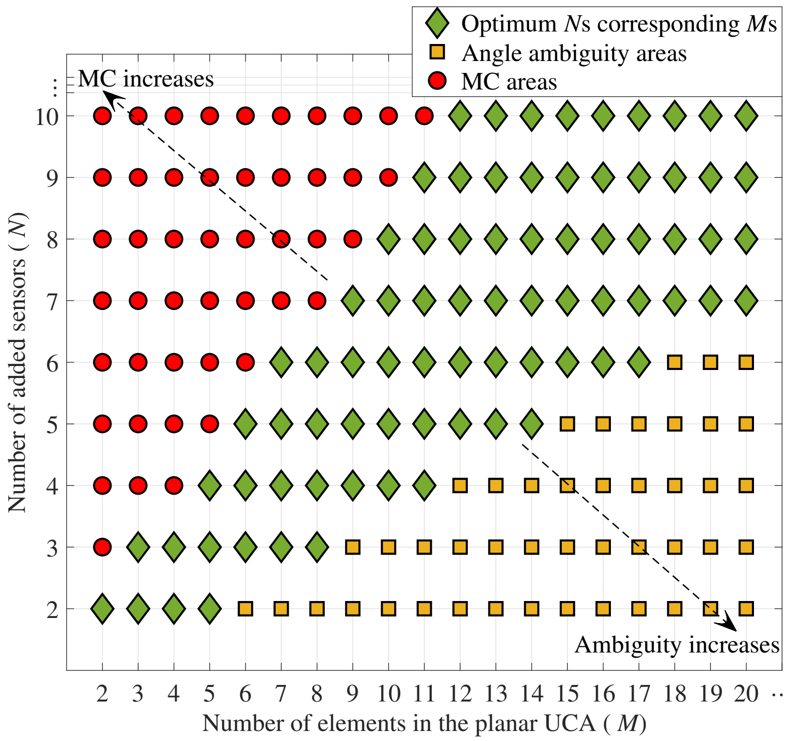

Figure 4.7: Trade-off between M and N for 3-D UCA

4.4.2. *M* and *N* Trade-off for 3-D USA

Substituting (4.27) into (4.40) yields,

$$\frac{d}{2} \leq d\sqrt{\frac{M\left(M-1\right)}{N\left(N^2-1\right)}} \leq 2d \tag{4.43}$$

thus, the relation between the number of sensors on the planar array M and the orthogonal branch N must hold the following conditions,

$$\frac{N\left(N^2-1\right)}{4} \leq M(M-1) \leq 4N\left(N^2-1\right) \quad \text{where } M=a^2,\ 1<a \text{ and } 2 \leq N \tag{4.44}$$

The graphical representation of the trade-off between M and N for 3-D USA is given in Figure 4.8.

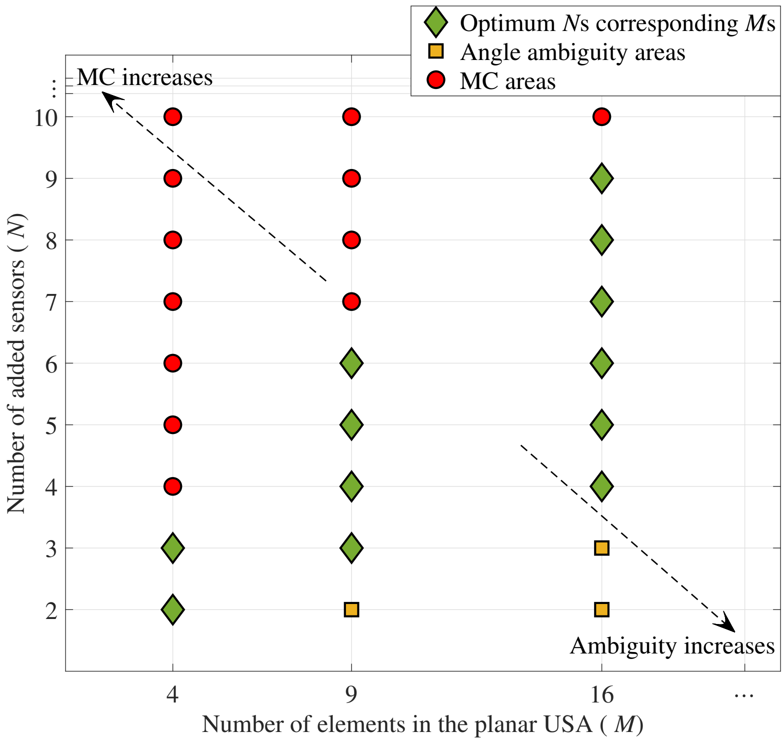

Figure 4.8: Trade-off between M and N for 3-D USA

4.4.3. *M* and *N* Trade-off for 3-D Cross Array

Substituting (4.37) into (4.40) yields,

$$\frac{d}{2} \leq d\sqrt{\frac{1}{8}\frac{(M-1)(M+1)(M+3)}{N\left(N^2-1\right)}} \leq 2d \tag{4.45}$$

thus, the relation between the number of sensors on the planar array M and the orthogonal branch N must hold following conditions

$$\begin{aligned} &2N\left(N^2-1\right) \leq (M-1)(M+1)(M+3) \leq 16N\left(N^2-1\right) \\ &\text{where } M = 1+4a,\ 1 \leq a \text{ and } 2 \leq N \end{aligned} \tag{4.46}$$

The graphical representation of the trade-off between M and N for 3-D cross array is given in Figure 4.9.

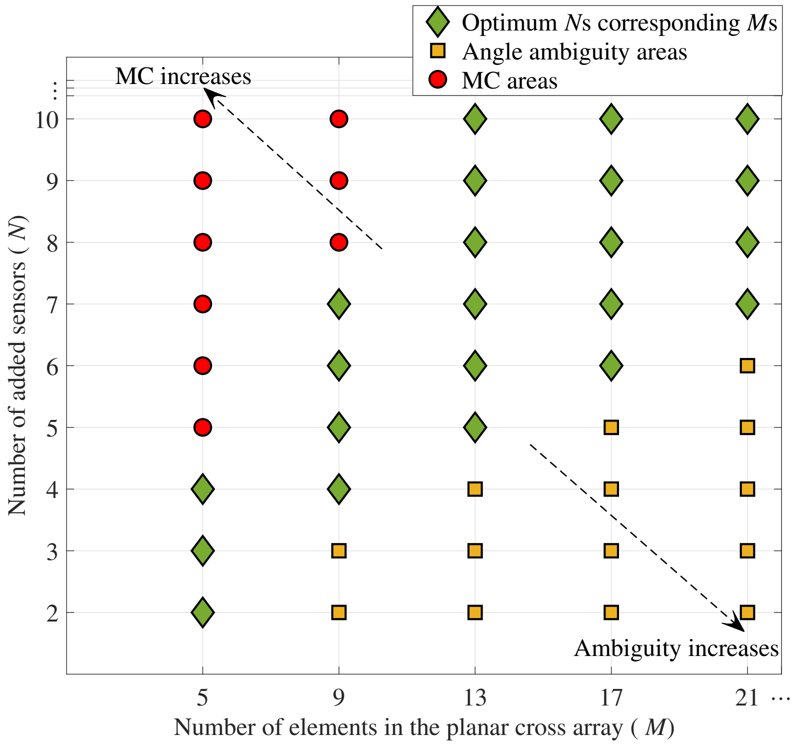

Figure 4.9: Trade-off between M and N for 3-D cross array

In Figures 4.7, 4.8, and 4.9, the green diamond markers represent the optimum number of added sensors on the z-axis corresponding to the number of the sensor in the given planar sensor arrays. The red circle markers mean that the MC effect occurs due to the selection of large Ns corresponding to the M. In other words, the distance between the two neighbor sensors added to the z-axis is less than a quarter-wavelength. The orange square markers show the angle ambiguity caused due to the selection of small Ns corresponding to the Ms. This means that adding too few additional sensors leads to high ambiguities when the number of elements in the given planar array is high.

4.5. Experimental Results

In this section, we compare the well-known centrosymmetric planar arrays after applying the proposed procedure to make them both azimuth and elevation isotropic 3-D arrays. Furthermore, we demonstrate that the proposed method, confirmed by analytical results in the previous sections, are also validated by different simulations. The simulations are taken with the same parameter settings for the array geometries handled. For the sake of fairness, we do take the equal overall number of sensor elements in the arrays. The elements of 3-D sensor arrays are located in $\mathbb{R}^3$ and are used to estimate the DOA of the single far-field narrow-band source signal. $\Psi = [\phi, \theta]^T$ denotes DOAs of the source signal, where $\phi \in [0, 180°]$ and $\theta \in [0, 90°]$ represent its azimuth and elevation angles, respectively, as demonstrated in Figure 2.2. Simulation of each array is fulfilled for the following parameter settings; The number of snapshots $T = 256$, SNR=10 dB, and $f_c = 500$ MHz.

For performance comparison of designed array geometries, we use the CRLB, which states the lower achievable variance on the azimuth and elevation performance as given in (2.22) and (2.23), which is illustrated as in Figures 4.10 and 4.11, respectively. Since the planar array geometries handled have two-axes symmetrical structure, they have azimuth isotropic performance throughout azimuth angles as seen in Figure 4.10 and satisfy sufficient conditions (4.2) and (4.3). Additionally, their DOA estimation errors converge to infinity as the elevation angle approaches $90°$ due to the fact that they do not satisfy (3.4). On the contrary, the proposed volumetric array geometries have fully isotropic performance throughout all elevation angle with equal CRLB level after the applied method.

The main contribution of the proposed method can be seen in Figure 4.11. The planar arrays fail to estimate the source signal accurately after a certain elevation degree, even though they have an isotropic performance on the azimuth estimation as shown in Figure 4.10. Notwithstanding, the proposed array geometries can estimate the source signals successfully with the same error level at all azimuth and elevation degrees, as shown in Figures 4.10 and 4.11, respectively.

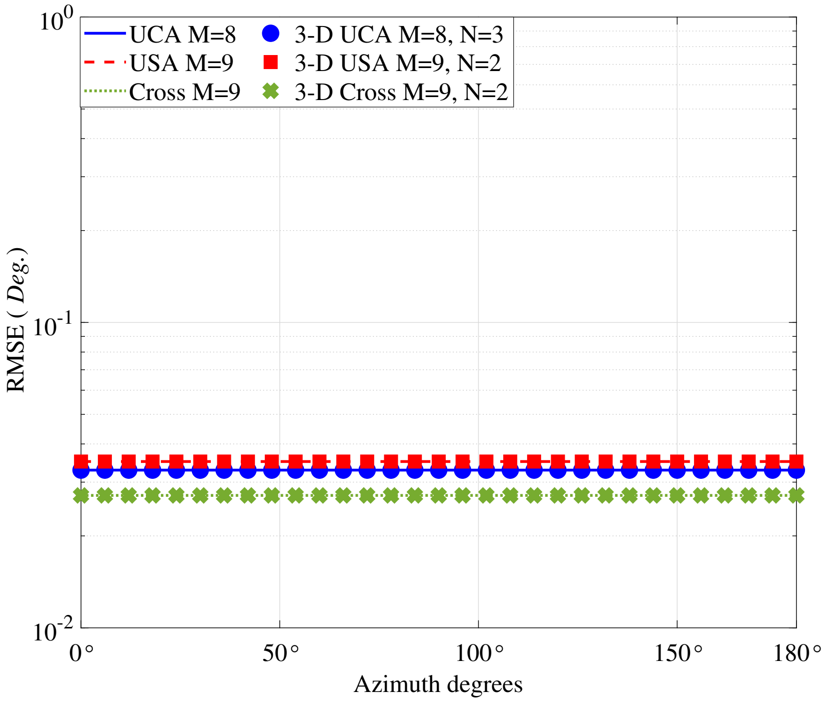

Figure 4.10: CRLB results: Azimuth DOA performance of the centrosymmetric arrays and the proposed extended version of them for the single-source case when the elevation angle is fixed ($\theta_{fix} = 80°$), and the azimuth angle is swept between $0°$ and $180°$.

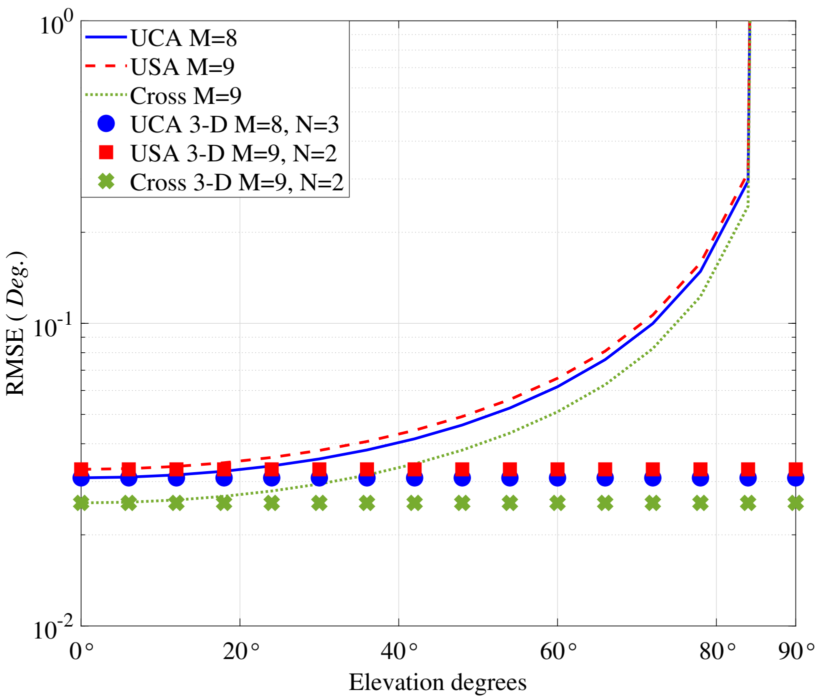

Figure 4.11: CRLB results: Elevation DOA performance of the centrosymmetric arrays and the proposed extended version of them for the single-source case when the azimuth angle is fixed ($\phi_{fix} = 20°$), and the elevation angle is swept between $0°$ and $90°$.

Since sensor array geometry affects output covariance matrix (2.13) and subspace-based DOA estimation algorithms depend on it, we investigate DOA estimation performance of the proposed 3-D arrays by computing 2-D MUSIC pseudo spectrum (2.24). In order to evaluate the DOA estimation performance of the arrays, we employ the root mean squared error (RMSE) for the azimuth and elevation DOAs as follows,

$$RMSE\left(\phi\right) = \sqrt{\frac{1}{J}\sum_{j=1}^{J}\left(\hat{\phi}_j - \phi\right)^2} \tag{4.47}$$

$$RMSE\left(\theta\right) = \sqrt{\frac{1}{J}\sum_{j=1}^{J}\left(\hat{\theta}_j - \theta\right)^2} \tag{4.48}$$

where $\hat{\phi}$ and ϕ are the estimated and actual azimuth DOA of the source, respectively. Similarly, $\hat{\theta}$ and θ are the estimated and actual elevation DOA of the source, respectively. Figure 4.12 shows that the 2-D MUSIC Estimation performance comparison with CRLB for the planar UCA and the proposed 3-D UCA. These simulations are fulfilled for the following parameter settings; The number of Monte-Carlo trials $J = 200$, the number of snapshots $T = 256$, SNR=20 dB, and $f_c = 500$ MHz.

When azimuth performance is obtained in simulations, all elevation angles are averaged for each azimuth angle with 0.1° intervals. Similarly, when elevation performance is obtained, all azimuth angles are averaged for each elevation angle with 0.1° intervals. As can be seen, the 2-D MUSIC performance of the proposed 3-D UCA exhibits isotropic performance similar to CRLB, although there are small deviations. Therefore, as a consequence, the proposed sensor arrays also provide 2-D isotropic DOA estimation performance in practical scenarios.

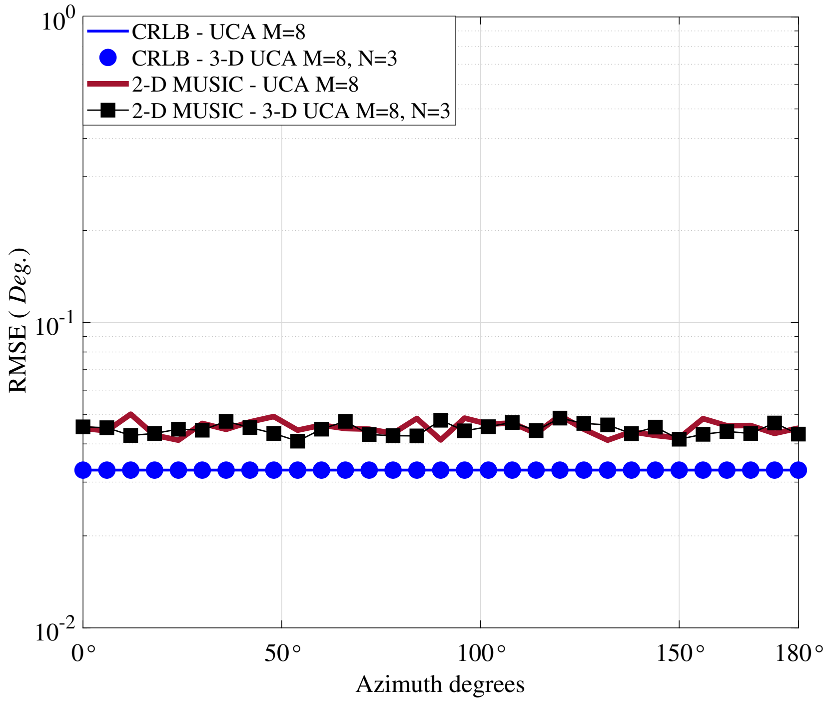

(a)

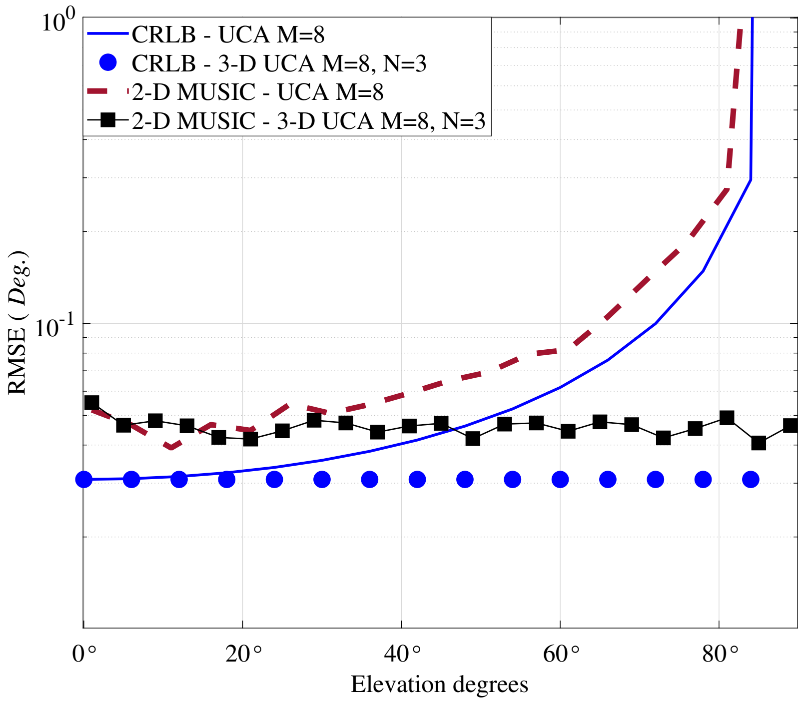

(b)

Figure 4.12: 2-D MUSIC Estimation performance comparison with CRLB: (a) the planar UCA and (b) the proposed 3-D UCA

In order to show the superiority of 3-D arrays obtained by the proposed method over planar arrays, a comparison of DOA estimation performance with the MUSIC algorithm is made. In this simulation, $J = 100$ Monte-Carlo trials are performed to estimate $L = 2$ uncorrelated far-field narrow-band sources positioned at $(40°, 85°)$ and $(120°, 15°)$ directions when SNR is 5 dB. Figure 4.13 shows the DOA estimation performance comparison of the planar UCA and the proposed 3-D UCA. Since the planar UCA and the proposed 3-D UCA have almost the same performance for all azimuth angles when the elevation angle is low $(\theta_1 = 15°)$, it is seen in Figures 4.13(a) and (b) that both of them can accurately estimate the first source signal $(\phi_1 = 120°, \theta_1 = 15°)$ without creating any side-lobes. However, the proposed volumetric array is overwhelmingly superior to the planar UCA after a certain elevation degree. Although the proposed 3-D UCA accurately estimates the second source $(\phi_2 = 40°, \theta_2 = 85°)$ without the side-lobes (see Figure 4.13(b)), the planar UCA can not estimate accurately as well as creating a high side-lobe at $(\phi_2^* = 40°, \theta_2^* = 95°)$, as shown in Figure 4.13(a). Note that elevation angles are swept up to $120°$ in this particular example to indicate the target's false peak.

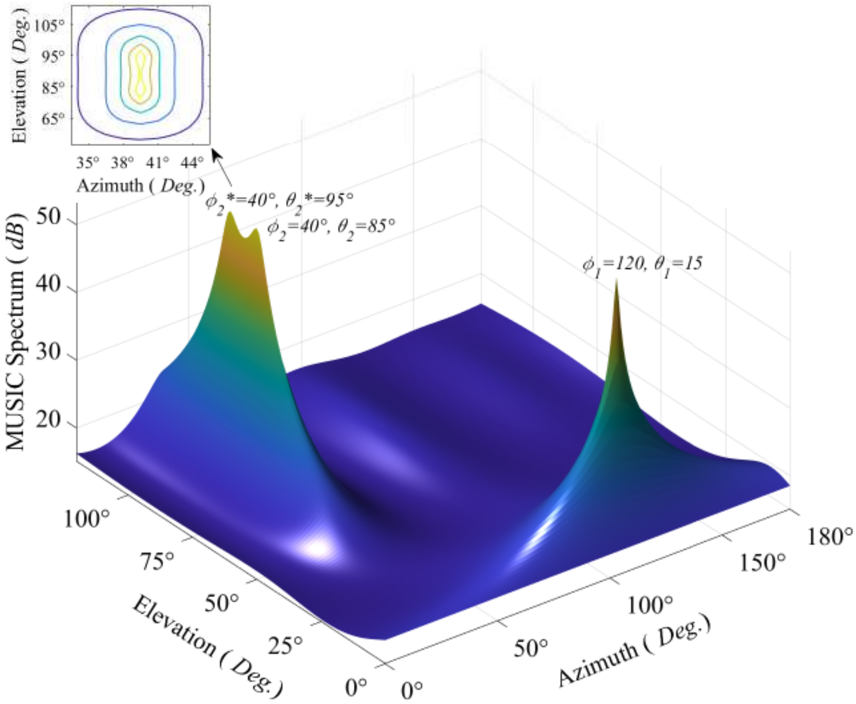

(a)

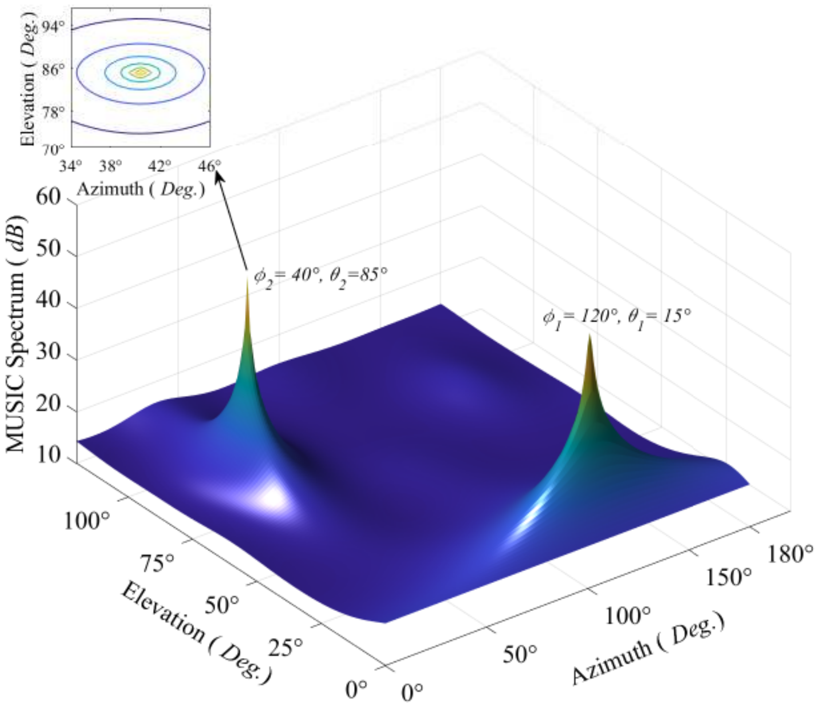

(b)

Figure 4.13: 2-D MUSIC Spectrum of (a) the planar UCA and (b) the proposed 3-D UCA

5. OPTIMUM 2-D ISOTROPIC VOLUMETRIC ARRAY DESIGN PROCEDURE

In this chapter, an optimum linear/planar array extension approach with adding the minimum number of sensors for the 2-D isotropic DOA estimation performance is investigated. Suppose any arbitrary planar array with M sensors is placed in the x-y plane (x-axis for linear arrays). ULA, UCA, V-shaped, and an arbitrary array is used as a test array, as shown in Figure 5.1. The proposed array extension approach is based on a two-phase method that extends any given arbitrary array into 3-D arrays by adding a minimum number of sensors to meet the 2-D isotropic DOA estimation conditions given in (3.3) and (3.4).

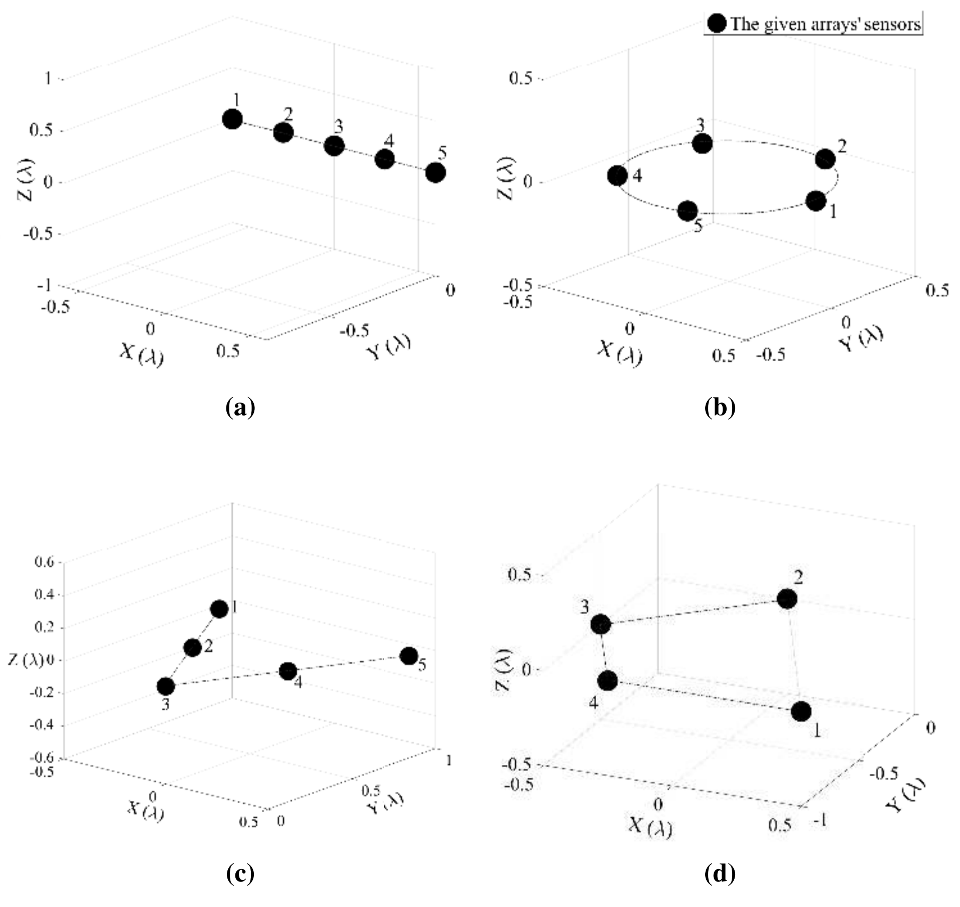

Figure 5.1: The given arrays: (a) ULA, (b) UCA, (c) V-shaped, and (d) Arbitrary array.

5.1. Phase-1

This phase verifies whether the cross moment-of-inertia, I_{xy}, of the given planar array is zero. If I_{xy} is already zero, then we can start Phase-2. Therefore, in this case, there is no need to add a new sensor to the *x*-*y* plane in the first phase. If I_{xy} is not zero, then a new sensor with (ζ_x, ζ_y) coordinates must be added to the *x*-*y* plane to make I_{xy} zero. Note that if the array was given on the *x*-*z* plane, this phase would be done for the I_{xz} by adding a new sensor with (ζ_x, ζ_z) coordinates. In our case, the updated planar array coordinates of the given array (4.1) as a result of the addition of this new sensor are defined as follows,

$$\mathbf{x}^{(1)} = [\mathbf{x}\ \ \zeta_x],\ \mathbf{y}^{(1)} = [\mathbf{y}\ \ \zeta_y],\ \mathbf{z}^{(1)} = [\mathbf{z}\ \ 0] \tag{5.1}$$

where $(\cdot)^{(1)}$ represents the updated parameter at the first phase. After some computational efforts detailed in Appendix C.1, the updated cross moment-of-inertia, $I_{xy}^{(1)}$ is obtained as,

$$I_{xy}^{(1)} = \sum_{m=1}^{M} x_m y_m + \frac{M}{M^{(1)}}\zeta_x\zeta_y - \frac{M^2}{M^{(1)}}\mu_{\mathbf{x}}\mu_{\mathbf{y}} - \frac{M}{M^{(1)}}\mu_{\mathbf{y}}\zeta_x - \frac{M}{M^{(1)}}\mu_{\mathbf{x}}\zeta_y \tag{5.2}$$

where $M^{(1)} = M + 1$. $\mu_{\mathbf{x}^{(1)}}$ and $\mu_{\mathbf{y}^{(1)}}$ are the updated mean of coordinates,

$$\mu_{\mathbf{x}^{(1)}} = \frac{M\mu_{\mathbf{x}} + \zeta_x}{M^{(1)}},\ \ \mu_{\mathbf{y}^{(1)}} = \frac{M\mu_{\mathbf{y}} + \zeta_y}{M^{(1)}} \tag{5.3}$$

Here (5.2) is a nonlinear equation with infinitely many solutions. Thus, the solution set which makes $I_{xy}^{(1)} = 0$, is a curve on the *x*-*y* plane as shown by the dotted blue line in Figure 5.2.

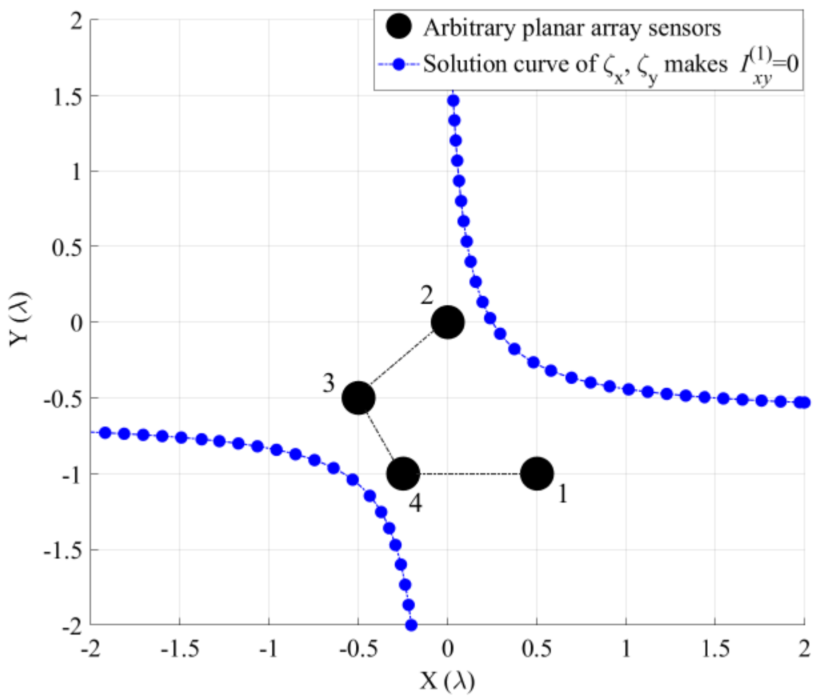

Figure 5.2: The solution curve which makes $I_{xy}^{(1)} = 0$ in Phase-1 for the given arbitrary array.

The two important design criteria are considered to find the optimum point on this curve. The first is the angular ambiguity, under which the steering vectors in (2.11) should be different for different DOAs. There are likely to be major angle ambiguities if any columns of the steering matrix ($\mathbf{A}$) are similar for different DOAs. Thus, when looking for the best solution for $I_{xy}^{(1)} = 0$, the azimuth and elevation angular ambiguity functions defined in [65], which measure the similarity between steering vectors, should be minimized. This analysis is made in detail in Section 5.2.

The second is the MC effect between the array elements. If array elements are closer to each other than $\lambda/4$, the array model in (2.9) is deviated and some special arrays and DOA estimation techniques are required [66]. We define the MC constraint in order to find a more general solution for arbitrary arrays, as the added sensor should not be closer than $\lambda/4$ to any sensor in the array. This distance limits the MC effect to a reasonable level [62] and can be adjusted more precisely in practical situations. The MC effect has been considered in all new sensor insertion phases.

5.2. Ambiguity Analysis

Array geometry design should deal with the ambiguity problem. Angle ambiguity arises when steering vectors in (2.11) with distinct DOAs are linearly dependent. In Phase-1, we determine the optimum coordinate of the added sensor by performing an azimuth angular ambiguity performance analysis. Then we observe the effect on the elevation angular ambiguity performance of the sensors added on the z-axis in Phase-2. The normalized azimuth angle ambiguity function is defined as, [13, 14, 65],

$$\mathbf{\Lambda}^{\theta}\left(\phi, \Delta\phi\right) = \frac{tr\left\{\mathbf{A}\left(\phi + \Delta\phi\right)^{H}\mathbf{A}\left(\phi\right)\right\}}{M^{(1)}L} \tag{5.4}$$

The elevation angle ambiguity function, $\mathbf{\Lambda}^{\phi}\left(\theta, \Delta\theta\right)$, can be written in a similar manner. The ambiguity function in (5.4) ranges from 0 to 1 which means perfect orthogonal and collinear, respectively. If the function takes a value between zero and one, that is, it is not perfectly collinear, then undesirable (false) peaks will occur. The search step sizes of azimuth $\phi \in [0°,\ 180°)$ and elevation $\theta \in [0°,\ 90°)$ are defined with $\Delta = 0.01°$. In practical applications, since targets can be in any direction, the calculation of azimuth ambiguity functions is carried out at all elevation angles and averaged. Vice versa, the elevation ambiguity functions are calculated at all azimuth angles and averaged. Thus, a square matrix $\mathbf{\Lambda}^{\theta}\left(\phi, \Delta\phi\right)$ and $\mathbf{\Lambda}^{\theta}\left(\phi, \Delta\phi\right)$ of order $180/\Delta$ and $90/\Delta$ is obtained, respectively. An example of low and high azimuth ambiguity results are shown in Figures 5.4 (a) and (b), respectively.

In order to find the optimum sensor location (ζ_x, ζ_y) in Phase-1, we evaluate (5.4) for each ζ_x, with a step of $\delta = 0.001\,(\lambda)$. Note that Figures 5.4 (a) and (b) are only two visualizations of all ζ_x values that create the Figures 5.5(a) and (b). The gain of the highest false peak and the number of false peaks are shown in Figures 5.5(a) and (b), respectively. Hereby, to get the optimum sensor location, (ζ_x, ζ_y), the following constrained optimization problem is defined as,

$$\begin{aligned} &\underset{\zeta_x,\zeta_y}{\text{minimize}} : \text{secondmax}\left\{\mathbf{\Lambda}^{\theta}\left(\phi, \Delta\phi\right)\right\} \\ &\text{subject to} : \|(\zeta_x, \zeta_y) - (x_i, y_i)\| > \frac{\lambda}{4}, \quad i = 1, \ldots, M \\ &I_{xy}^{(1)} = 0 \end{aligned} \tag{5.5}$$

The optimum location (ζ_x, ζ_y) minimizes the estimated sources' side-lobe-levels (SLLs) or false peaks subject to the constraints of MC and zero cross moment-of-inertia. Regions for low ambiguity and high MC determined as a result of (5.5) are shown with hexagram and triangle markers, respectively, in Figure 5.3. In fact, the optimization problem given in (5.5) creates constraints that keep the added sensor location (ζ_x, ζ_y) on the solution curve and avoid the region with a high MC area. Then it forces the added sensor location to select in the green region (see Figure 5.3), where the array has the lowest angle ambiguity gain with the minimum number of false peaks, as shown in Figure 5.5. As a result of this optimization, the sensor's optimum position selected on the solution curve in the first phase is shown with a square (■) marker in simulations.

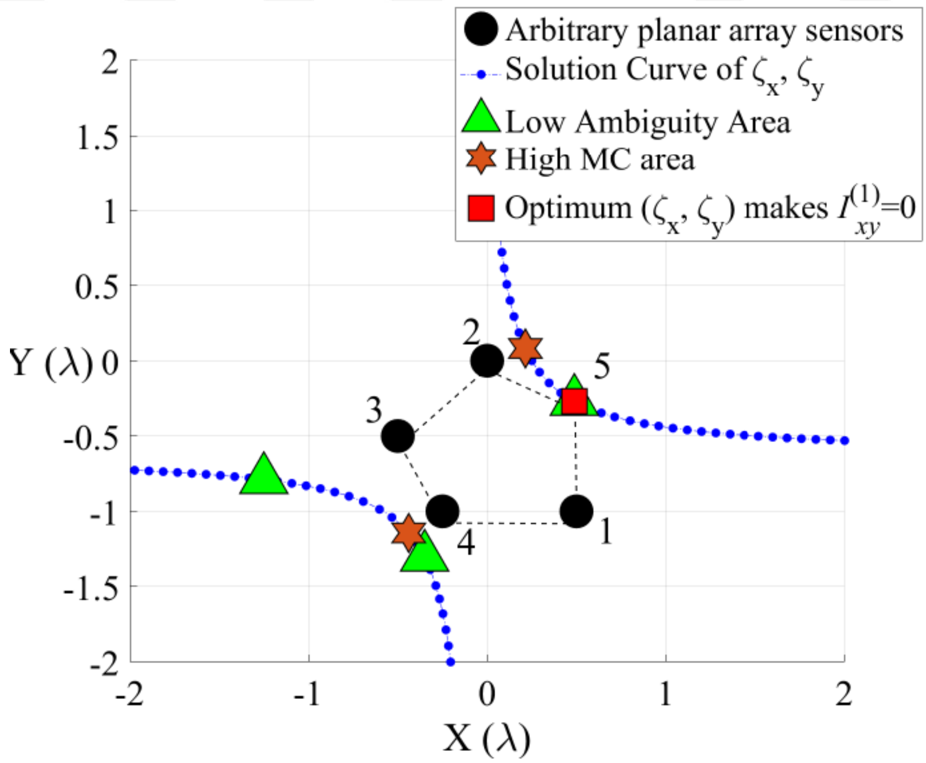

Figure 5.3: Areas on the solution curve obtained by 2 in Phase-1, showing high MC, low azimuth ambiguity, and selected optimum sensor location.

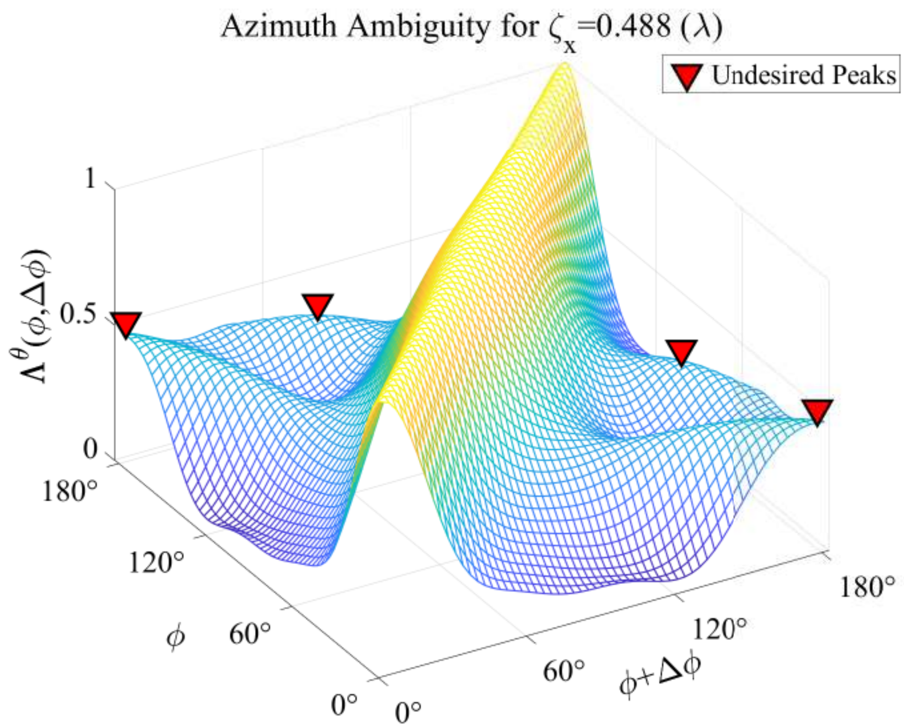

(a)

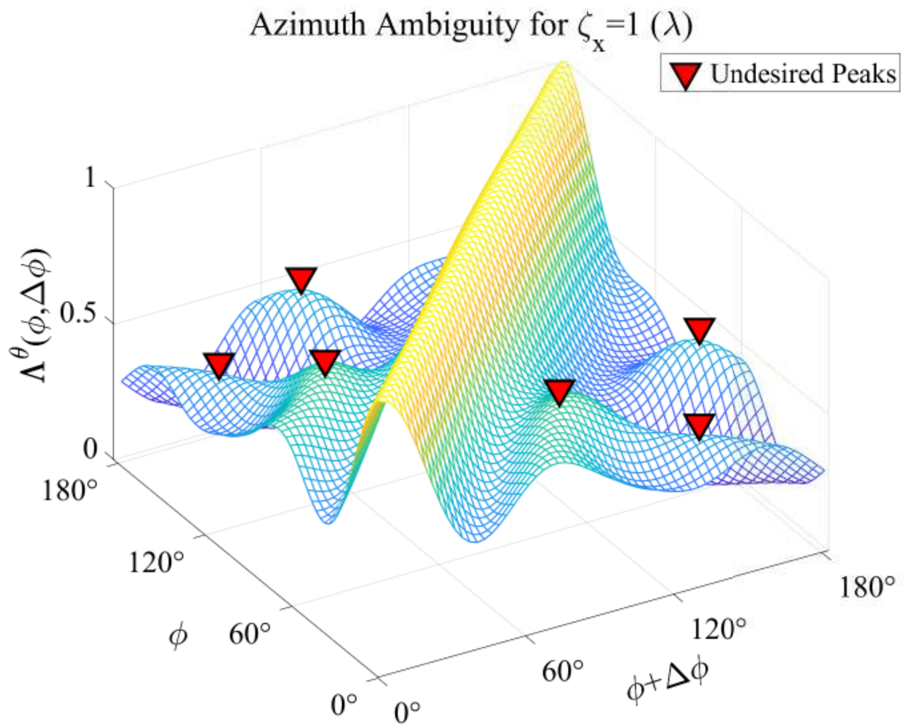

(b)

Figure 5.4: Azimuth ambiguity comparison of the array resulting from the sensor added to the planar array in Phase-1 for (a) Optimum location $\zeta_x = 0.488\,(\lambda)$ and (b) High ambiguity location $\zeta_x = 1\,(\lambda)$

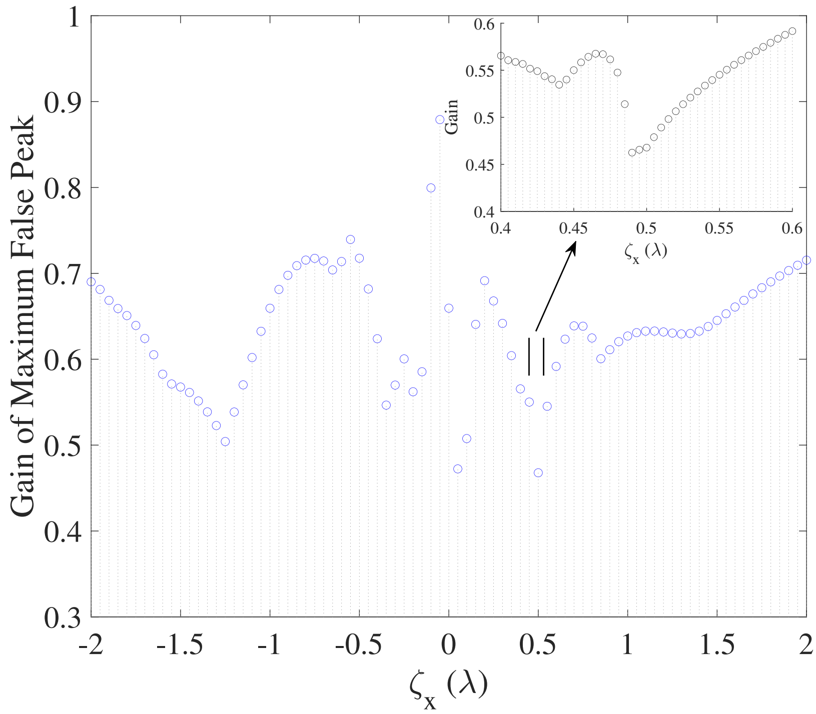

(a)

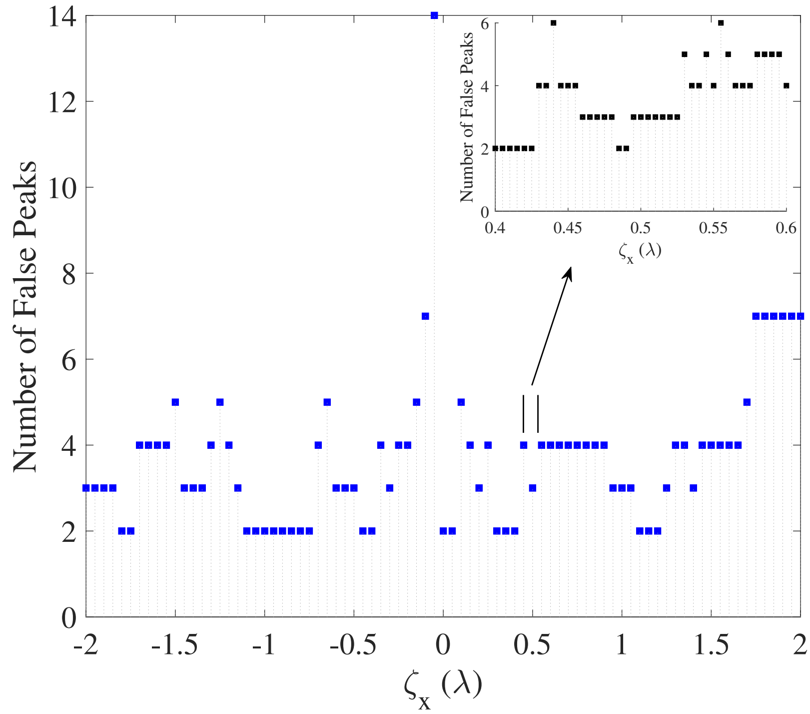

(b)

Figure 5.5: Azimuth angle ambiguity analysis for the arbitrary array given in Figure 5.2: (a) The gain of the highest false peak (b) The number of false peaks, corresponding the selected ζ_x locations on the solution curve in Phase-1

5.3. Phase-2

In this phase, we have to equalize the auto moment-of-inertia of coordinates (I_{xx}, I_{yy}, and I_{zz}) while still keeping the cross-moments (I_{xy}, I_{xz}, and I_{yz}) fixed at zero. Therefore, we first find the largest auto moment-of-inertia between *x*,*y*, and *z* coordinates and bring the rest to this value by adding new sensors.

$$\mathbb{I} = \max \left\{ I_{xx}^{(1)},\ I_{yy}^{(1)},\ I_{zz}^{(1)} \right\} \tag{5.6}$$

where $\mathbb{I}$ is the largest auto moment-of-inertia among $\mathbf{x}^{(1)}$, $\mathbf{y}^{(1)}$, and $\mathbf{z}^{(1)}$ coordinates.

Then, to equalize $I_{xx}^{(1)}$, $I_{yy}^{(1)}$, and $I_{zz}^{(1)}$ without altering the mean of *z*, we need to insert *N* new sensors as follows,

$$\begin{aligned} \mathbf{x}^{(2)} &= \left[\mathbf{x}^{(1)} \ \ d_x \mathbf{1}_N\right] \\ \mathbf{y}^{(2)} &= \left[\mathbf{y}^{(1)} \ \ d_y \mathbf{1}_N\right] \\ \mathbf{z}^{(2)} &= \left[\mathbf{z}^{(1)} \ \ d_z \left(\frac{(N+1)}{2} - i\right)\right] \end{aligned} \tag{5.7}$$

where $i = 1, \ldots, N$. The updated parameters at the second phase are denoted by $(\cdot)^{(2)}$. The updated auto moment-of-inertia of $\mathbf{x}^{(2)}$, $\mathbf{y}^{(2)}$, and $\mathbf{z}^{(2)}$ coordinates are presented in Appendix C.2 as follows,

$$I_{xx}^{(2)} = \frac{M^{(1)}N}{M^{(2)}} {d_x}^2 - \frac{{M^{(1)}}^2}{M^{(2)}} \mu_{\mathbf{x}^{(1)}}^2 - \frac{2M^{(1)}N}{M^{(2)}} \mu_{\mathbf{x}^{(1)}} d_x + \|\mathbf{x}^{(1)}\|^2 \tag{5.8}$$

$$I_{yy}^{(2)} = \frac{M^{(1)}N}{M^{(2)}} {d_y}^2 - \frac{{M^{(1)}}^2}{M^{(2)}} \mu_{\mathbf{y}^{(1)}}^2 - \frac{2M^{(1)}N}{M^{(2)}} \mu_{\mathbf{y}^{(1)}} d_y + \|\mathbf{y}^{(1)}\|^2 \tag{5.9}$$

$$I_{zz}^{(2)} = \frac{N\left(N^2 - 1\right)}{12} {d_z}^2 - \frac{{M^{(1)}}^2}{M^{(2)}} \mu_{\mathbf{z}^{(1)}}^2 + \|\mathbf{z}^{(1)}\|^2 \tag{5.10}$$

where $M^{(2)} = M^{(1)} + N$. $\mu_{\mathbf{x}^{(2)}}$, $\mu_{\mathbf{y}^{(2)}}$, and $\mu_{\mathbf{z}^{(2)}}$ are the updated mean of coordinates at the second phase,

$$\begin{aligned} \mu_{\mathbf{x}^{(2)}} &= \frac{M^{(1)}\mu_{\mathbf{x}^{(1)}} + N d_x}{M^{(2)}}, \quad \mu_{\mathbf{y}^{(2)}} = \frac{M^{(1)}\mu_{\mathbf{y}^{(1)}} + N d_y}{M^{(2)}} \\ \mu_{\mathbf{z}^{(2)}} &= \frac{M^{(1)}\mu_{\mathbf{z}^{(1)}}}{M^{(2)}} \end{aligned} \tag{5.11}$$

The following three equations are solved for the unknowns d_x, d_y, and d_z,

$$I_{xx}^{(2)} - \mathbb{I} = 0, \;\; I_{yy}^{(2)} - \mathbb{I} = 0, \;\; I_{zz}^{(2)} - \mathbb{I} = 0 \tag{5.12}$$

The locations of the new additional *N* sensors found by (5.12) are substituted into (5.7) to equalize the auto moment-of-inertia of coordinates. These sensors added in Phase-2 are marked with a diamond (♦) marker in the simulations. Note that at the beginning of the second phase, we find the coordinate with the largest auto moment-of-inertia in the first phase, and the other coordinates are updated according to this value. Obviously, it could be $\mathbb{I} = I_{xx}^{(1)}$ or $\mathbb{I} = I_{yy}^{(1)}$ here. For instance, if $I_{xx}^{(1)}$ has the largest auto moment-of-inertia, then $d_x = 0$ and $d_y,\ d_z \in \mathbb{R}^+$ from (5.12). Therefore, the cross moment-of-inertia between *x* and *y* coordinates, which is zeroed in the first phase, will remain zero because one of the d_x or d_y coordinates of the newly added sensors in the second phase will already be zero. Consequently, without proof, but also conjectured because of numerical evidence, at the end of the second phase the cross moments-of-inertia between *x* and *y* coordinates remain zero. Finally, at the end of the procedure, the extended volumetric sensor array design will have a 2-D isotropic DOA estimation performance satisfying MC constraint with minimum azimuth and elevation angular ambiguity.

The proposed array extension algorithm is valid for all uniform/nonuniform linear and planar arrays. The proposed two-phase algorithm is presented in Appendix C.4 in Algorithm 1 for the arrays placed on the *x*-*y* plane. If an array is given on different planes, then the subscripts should be changed accordingly in the algorithm.

5.4. The Selection of *N*

In order to extend any given array with this approach, the number of sensors inserted to the *z*-axis and the number of sensors in the given array must be at least two. That is $2 \leq N$ and $2 \leq M$. When designing a volumetric array, we may choose to add a minimum number of additional sensors *N* to a linear or planar array of at least two sensors. On the other hand, even if the number of sensors *N* added to the *z*-axis does not affect the azimuth ambiguity, the elevation ambiguity is significantly affected. The elevation angle ambiguity function, i.e., $\mathbf{\Lambda}^{\phi}\left(\theta, \Delta\theta\right)$, is obtained similarly to (5.4) using $M^{(2)}$ instead of $M^{(1)}$ and replacing θ and ϕ. This function is used as a performance criterion to decide

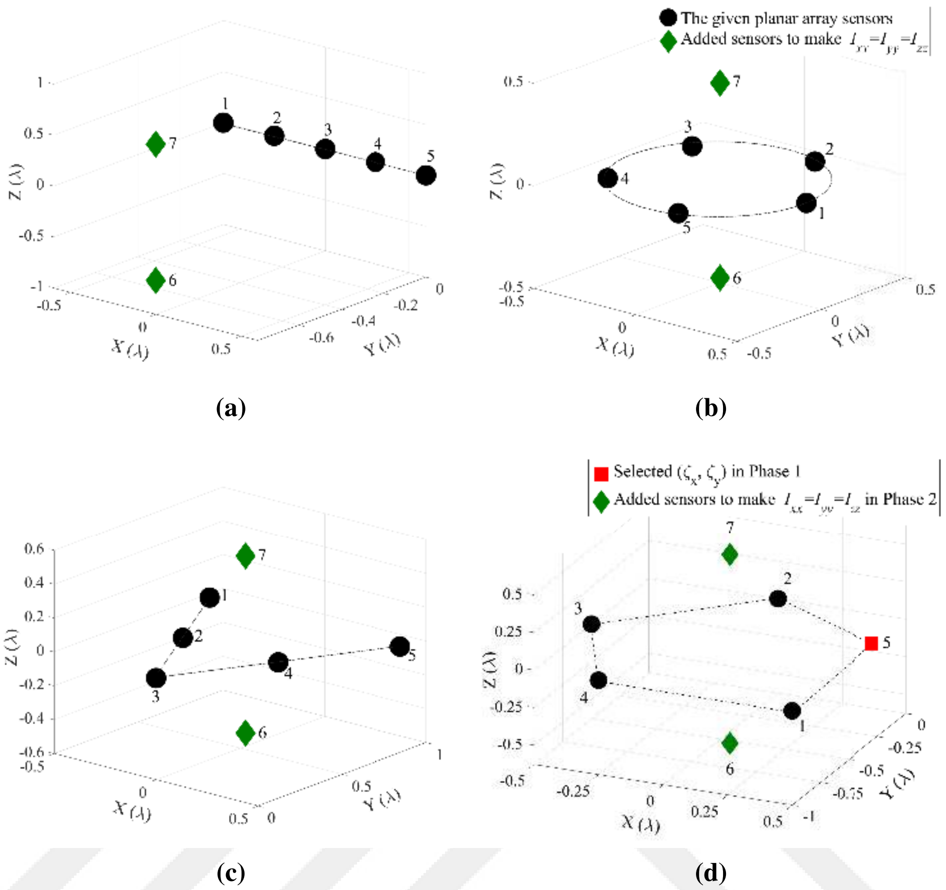

Figure 5.6: The proposed 2-D isotropic volumetric arrays with sensors (♦) added to the z-axis of (a) ULA, (b) UCA, (c) V-shaped arrays, and (d) arbitrary array

the convenient number of sensors added in Phase-2. If we choose a small N, the elevation angle ambiguity (the number or gains of side-lobe peaks) may increase too much as the distance between the sensors increases. However, if we choose a large N, the sensors on the z-axis become close. Thus, the MC effect occurs. As a consequence, there is a trade-off in choosing Ns, according to Ms. The graphical representation of the elevation angle ambiguity analysis for the arbitrary array given in Figure 5.1(d) is shown in Figure 5.7. As one can see, the distance between the sensors decreases while the number of sensors added to the z-axis increases. The effect of the MC, therefore, increases, even though the elevation angle ambiguity decreases.

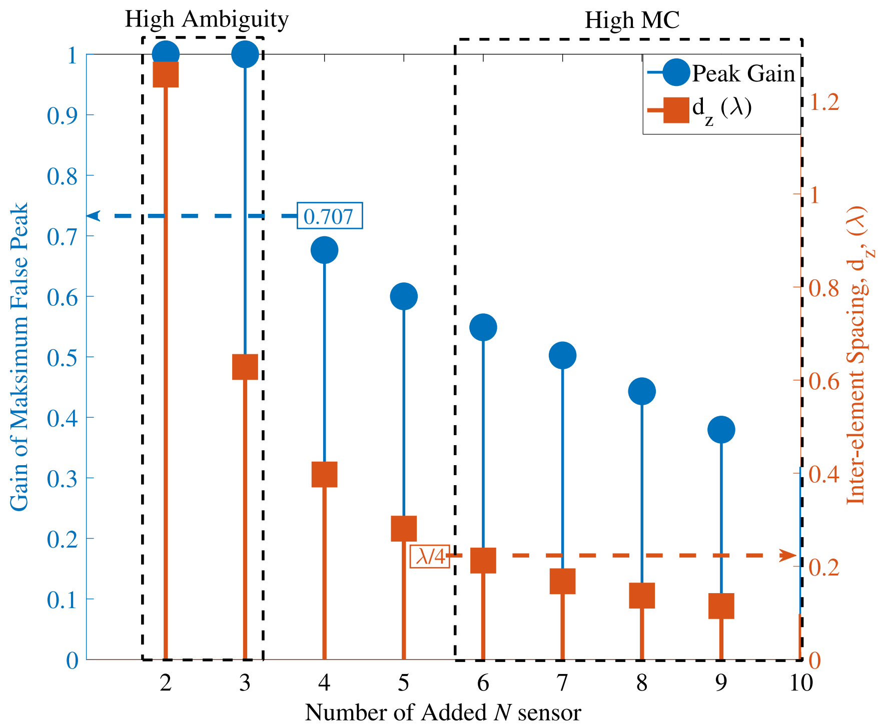

Figure 5.7: The ambiguity and MC regions corresponding to the number of the added sensors, N, on the z-axis in Phase-2. Left and right y-axes represent the gain of the highest false peak and inter-element spacing, d_z, respectively

5.5. Experimental Results and Discussions

In this section, the improvements in the 2-D DOA estimation performance of the arrays obtained with the proposed design method shown in Figure 5.6 are illustrated with various simulations. The proposed design approach is applied to ULA, UCA, and V-shaped arrays commonly used in the literature shown in Figures 5.1(a), (b), and (c), respectively. We also applied it to an arbitrary planar array shown in Figure 5.1(d) to show that the proposed method is applicable for all linear/planar arrays. The sensor coordinates for the tested arrays are given in Appendix C.3 in Table C.1. For clarity, the given planar array elements are indicated with circle markers (●) for $M = 5$ sensors. In Phase-1, when a sensor is added, it is indicated as a square marker (■). Diamond markers (◆) indicate each sensor added in Phase-2. Furthermore, we do take the equal overall number of sensor elements in the arrays for the sake of fairness.

The elements of sensor array geometries are located in $\mathbb{R}^3$ and are used to estimate the DOA of the single far-field narrow-band source signal. $\Psi = [\phi, \theta]^T$ denotes DOAs of the source signal, where $\phi \in [0, 180°]$ and $\theta \in [0, 90°]$ represent its azimuth and elevation angles, respectively, as demonstrated in Figure 2.2. Simulation of each array is fulfilled for the following parameter settings; The number of snapshots $T = 256$, SNR=20 dB, and $f_c = 500$ MHz.

For performance comparison of designed array geometries, we use the CRLB, which states the lower achievable variance on the azimuth and elevation DOA estimation performances as given in (2.22) and (2.23), which is illustrated as in Figures 5.8(a) and (b), respectively. The azimuth and elevation DOA estimation performance comparisons of the arrays given in Figure 5.1 and their 3-D versions given in Figure 5.6 are shown in Figure 5.8.

The proposed two-phase array design approach adds new sensors to any linear/planar arrays to obtain a 2-D isotropic volumetric array, i.e., equalize CRLB levels across the entire azimuth/elevation angle. Whereby ULA, UCA, and V-shaped arrays' cross moments-of-inertia are zero, equation (3.3) is already satisfied. Hence the first phase of Algorithm 1 is skipped the second phase proceeds. In this phase, the new additional *N* sensors' positions, (5.7), are solved for the minimum possible $N = 2$. The inserted new sensors in the second phase are marked with the diamond markers (◆) in order to fulfill (3.4) for ULA, UCA, and V-shaped arrays are shown in Figures 5.6(a), (b), and (c), respectively.

As seen in Figure 5.8(a), ULA's azimuth estimation performance, which has low estimation error in broad-side, reaches infinite error towards end-fires. Besides, ULA's elevation estimation error approaches infinity as the elevation angle approaches $90°$, as shown in Figure 5.8(b). However, when new sensors are added with the proposed method, the 3-D ULA has equal estimation performance across all azimuth and elevation angles, as shown in Figures 5.8(a) and (b), respectively.

Furthermore, inserting new additional sensors to the already azimuth isotropic planar arrays such as UCA and V-shaped [31] arrays does not adversely affect azimuth DOA estimation performance, as seen in Figure 5.8(a). However, the elevation estimation errors approach infinity for the given planar arrays when the elevation angle approaches $90°$, as seen in Figure 5.8(b). Hereby, inserting new additional sensors to the given planar arrays does not affect azimuth performance as well as improves elevation performance. As a result, 3-D arrays obtained by the proposed method have 2-D isotropic performance.

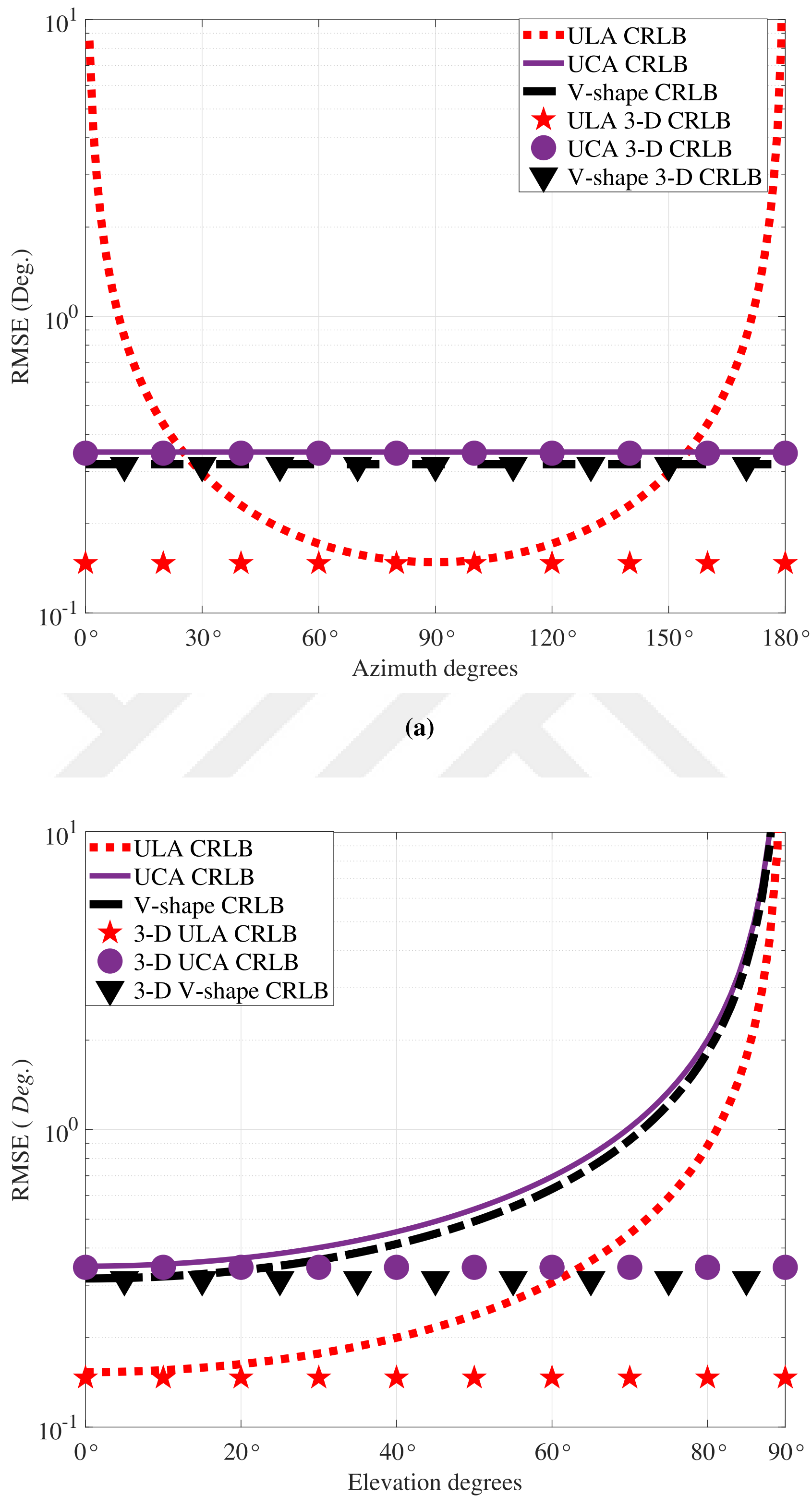

(a)

(b)

Figure 5.8: CRLB results: (a) Azimuth Performance ($\theta_{fixed} = 85°$) (b) Elevation performance ($\phi_{fixed} = 15°$)

In order to verify that the proposed algorithm creates a volumetric array that satisfies 2-D isotropy conditions for all given linear or planar arrays, we consider a planar array consisting of four sensors whose coordinates are randomly selected as shown by circle markers (●) in Figure 5.3. This planar arbitrary array is not centrosymmetric, and therefore it does not fulfill both the (3.3) and (3.4) conditions. If we apply the proposed algorithm to this arbitrary array, in the first phase, a solution curve is created on the *x*-*y* plane that equalizes the planar arrays' cross moment-of-inertia to zero. Then, the solution of (5.5) gives the optimum sensor location (ζ_x, ζ_y), which is marked with a square marker (■) on this curve, as shown in Figure 5.3. This solution gives the added sensor's optimum location on the first phase that provides the minimum azimuth angle ambiguity with satisfying the MC and $I_{xy} = 0$ constraints. After that, in the second phase of the algorithm, two new sensors marked as diamond (♦) are added, as shown in Figure 5.6(d), to equalize the *x*, *y*, and *z* coordinates' auto moments-of-inertia. In this phase, while adding new sensors, the number of sensors to be added (*N*) according to the number of sensors in the array (*M*) is taken into account for the elevation angle ambiguity, $\mathbf{\Lambda}^{\phi}\left(\theta, \Delta\theta\right)$. To sum up, a sensor is added in the first phase to make the cross moment-of-inertia to zero, and two more sensors are added in the second phase to equalize the auto moments-of-inertia of the coordinates.

The azimuth and elevation DOA estimation performances before and after applying the proposed array design method to the given arrays are shown in Figures 5.9(a) and (b), respectively. The sensors' effect gradually added in the first and second phases on CRLB levels is shown in Figures 5.9(a) and (b).

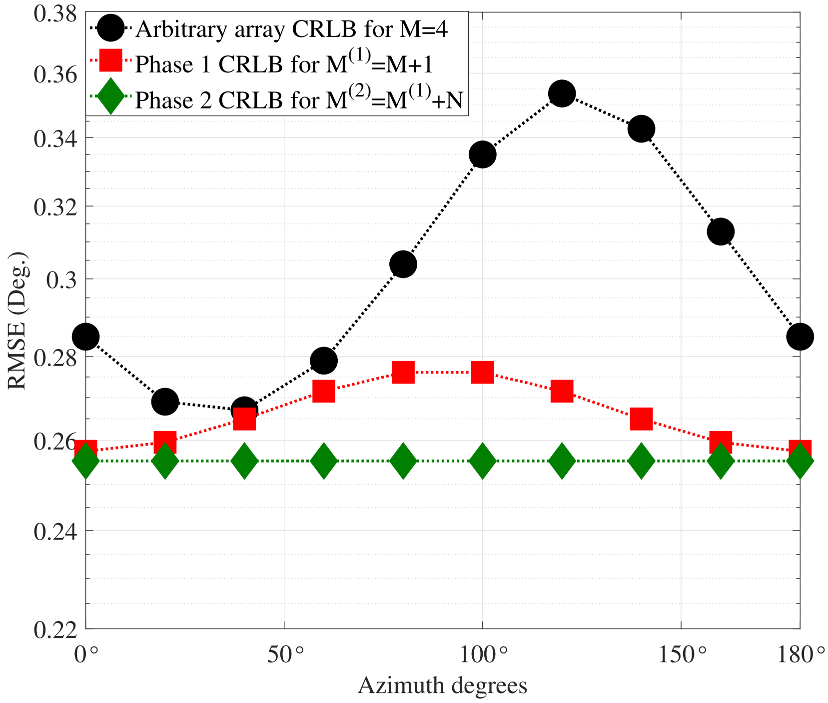

(a)

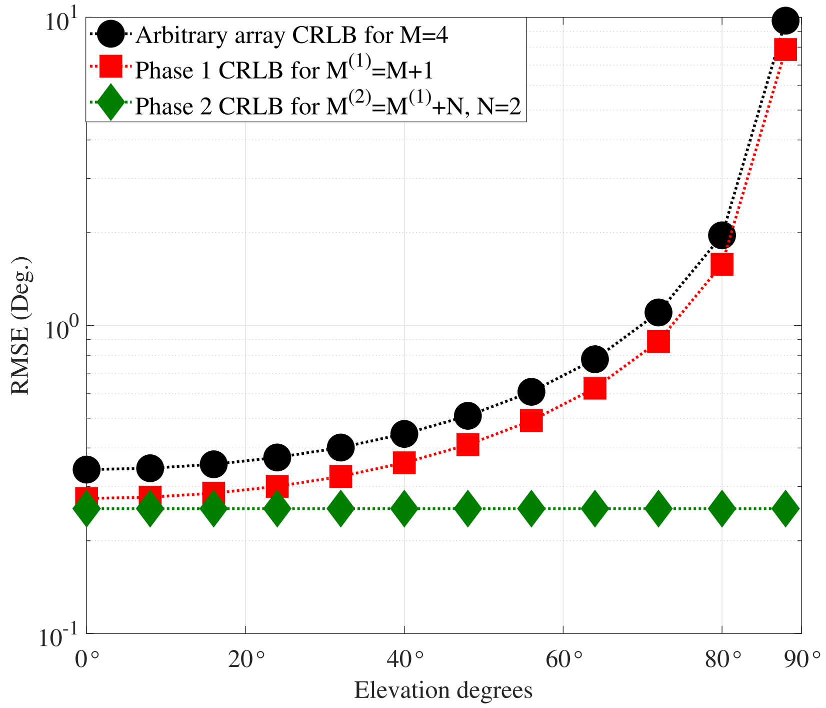

(b)

Figure 5.9: CRLB results of each phase: (a) Azimuth performances ($\theta_{fixed} = 85°$) (b) Elevation performances ($\phi_{fixed} = 15°$)

Here, we investigate the DOA estimation performance of the proposed 3-D array by computing the 2-D MUSIC pseudo spectrum (2.24). In simulations, 100 Monte-Carlo trials are performed to estimate $K = 2$ uncorrelated far-field narrow-band source positioned at $(40°, 85°)$ and $(120°, 15°)$ directions when SNR is 5 dB. In order to show the superiority of 3-D arrays obtained by the proposed method over planar arrays, a comparison of DOA estimation performance with the MUSIC algorithm is made. Figure 5.10 shows the DOA estimation performance comparison of the planar V-shaped array and the proposed 3-D V-shaped array. Since the planar V-shaped array and the proposed 3-D V-shaped array have almost the same performance for all azimuth angles when the elevation angle is low $(\theta_1 = 15°)$, it is seen in Figures 5.10(a) and (b) that both of them can accurately estimate the first source signal $(\phi_1 = 120°, \theta_1 = 15°)$ without creating any side-lobes. However, the proposed volumetric array is overwhelmingly superior to the planar V-shaped array after a certain elevation degree. Although the proposed 3-D V-shaped array accurately estimates the second source $(\phi_2 = 40°, \theta_2 = 85°)$ without the side-lobes (see Figure 5.10(b)), the planar V-shaped array can not estimate accurately as well as creating a high side-lobe at $(\phi_2^* = 40°, \theta_2^* = 95°)$ as shown in Figure 5.10(a).

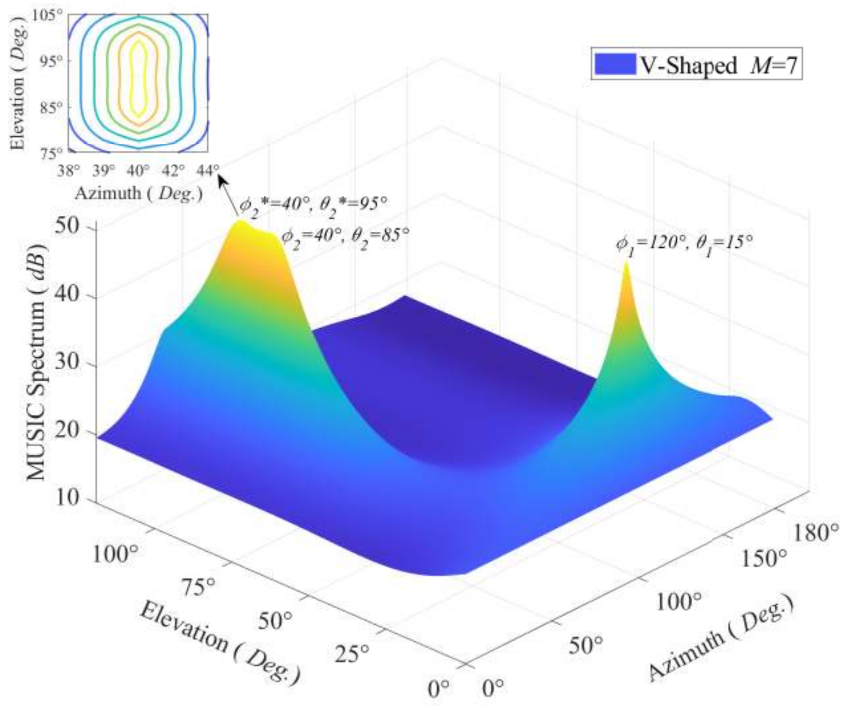

(a)

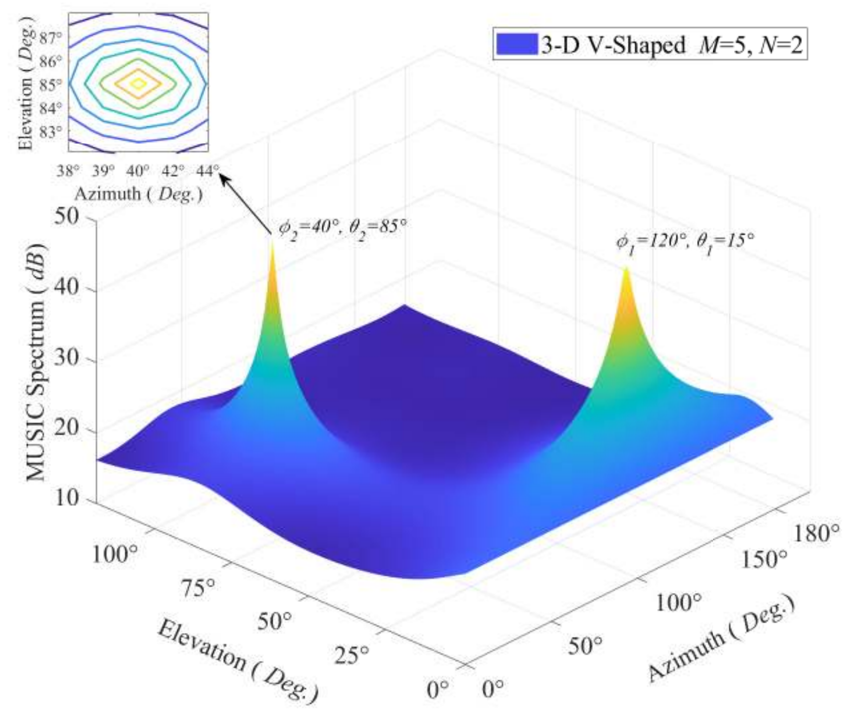

(b)

Figure 5.10: 2-D MUSIC spectrum for (a) the planar V-shaped and (b) proposed 3-D V-shaped arrays

5.6. Proof by Contradiction: Adding at least *N*=2 sensors is optimal

This chapter has proposed an array design approach that needs at least two additional sensors so as to satisfy both azimuth and elevation isotropic conditions. In this section, we have shown that a contradiction proof in order to determine the required minimum number of additional sensors for 2-D isotropic volumetric array extension. Seeing that a common solution may not exist for a nonlinear set of equations of any given linear or planar arrays, we concluded that our earlier volumetric array design approach proved to be reasonable. Let us assume that we have given a planar array with the following coordinates,

$$\begin{aligned} \mathbf{x} &= [x_1, x_2, \ldots, x_M] \\ \mathbf{y} &= [y_1, y_2, \ldots, y_M] \\ \mathbf{z} &= [z_1, z_2, \ldots, z_M] \end{aligned} \tag{5.13}$$

Assume that we add *N* additional sensors, then the updated coordinates are denoted by $(\cdot)^u$ as follows,

$$\begin{aligned} \mathbf{x}^u &= [x_1, x_2, \ldots, x_M,\ d_{x1}, d_{x2}, \ldots, d_{xN}] \\ \mathbf{y}^u &= [y_1, y_2, \ldots, y_M,\ d_{y1}, d_{y2}, \ldots, d_{yN}] \\ \mathbf{z}^u &= [z_1, z_2, \ldots, z_M,\ d_{z1}, d_{z2}, \ldots, d_{zN}] \end{aligned} \tag{5.14}$$

Mean of updated coordinates,

$$\begin{aligned} \mu_{\mathbf{x}}^u &= \frac{1}{M+N} \sum_{m=1}^{M+N} x_m^u = \frac{M\mu_{\mathbf{x}} + \sum_{n=1}^{N} d_{xn}}{M+N} \\ \mu_{\mathbf{y}}^u &= \frac{1}{M+N} \sum_{m=1}^{M+1} y_m^u = \frac{M\mu_{\mathbf{y}} + \sum_{n=1}^{N} d_{y_n}}{M+N} \\ \mu_{\mathbf{z}}^u &= \frac{1}{M+N} \sum_{m=1}^{M+1} z_m^u = \frac{M\mu_{\mathbf{z}} + \sum_{n=1}^{N} d_{zn}}{M+N} \end{aligned} \tag{5.15}$$

Cross moment-of-inertia between the updated *x* and *y* coordinates is,

$$\begin{aligned} I_{xy}^{u} &= \sum_{m=1}^{M} \left(x_m^u - \mu_{\mathbf{x}}^u\right)\left(y_m^u - \mu_{\mathbf{y}}^u\right) \\ &= \sum_{m=1}^{M} x_m y_m + \sum_{n=1}^{N} d_{xn} d_{y_n} - \mu_{\mathbf{y}}^u \left(\sum_{m=1}^{M} x_m + \sum_{n=1}^{N} d_{xn}\right) \\ &- \mu_{\mathbf{x}}^u \left(\sum_{m=1}^{M} y_m + \sum_{n=1}^{N} d_{y_n}\right) + (M+N)\,\mu_{\mathbf{x}}^u \mu_{\mathbf{y}}^u \\ &= \sum_{m=1}^{M} x_m y_m + \sum_{n=1}^{N} d_{xn} d_{y_n} - (M+N)\,\mu_{\mathbf{x}}^u \mu_{\mathbf{y}}^u \end{aligned} \tag{5.16}$$

Similarly, cross moments-of-inertia between the updated *x*-*z* and *y*-*z* coordinates are,

$$I_{xz}^{u} = \sum_{m=1}^{M} x_m z_m + \sum_{n=1}^{N} d_{xn} d_{zn} - (M+N)\,\mu_{\mathbf{x}}^u \mu_{\mathbf{z}}^u \tag{5.17}$$

$$I_{yz}^{u} = \sum_{m=1}^{M} y_m z_m + \sum_{n=1}^{N} d_{y_n} d_{zn} - (M+N)\,\mu_{\mathbf{y}}^u \mu_{\mathbf{z}}^u \tag{5.18}$$

Auto moment-of-inertia of the updated *x*-coordinate is,

$$\begin{aligned} I_{xx}^{u} &= \left(x_1^u - \mu_{\mathbf{x}}^u\right)^2 + \left(x_2^u - \mu_{\mathbf{x}}^u\right)^2 + \cdots + \left(x_M^u - \mu_{\mathbf{x}}^u\right)^2 \\ &+ \left(d_{x1} - \mu_{\mathbf{x}}^u\right)^2 + \left(d_{x2} - \mu_{\mathbf{x}}^u\right)^2 + \cdots + \left(d_{xN} - \mu_{\mathbf{x}}^u\right)^2 \\ &= {x_1}^2 + {x_2}^2 + \cdots + {x_M}^2 - 2\mu_{\mathbf{x}}^u \left(x_1 + x_2 + \cdots + x_M\right) + M\mu_{\mathbf{x}}^{u2} \\ &+ {d_{x1}}^2 + {d_{x2}}^2 + \cdots + {d_{xN}}^2 - 2\mu_{\mathbf{x}}^u \left(d_{x1} + d_{x2} + \cdots + d_{xN}\right) + N\mu_{\mathbf{x}}^{u2} \\ &= \sum_{m=1}^{M} {x_m}^2 + \sum_{n=1}^{N} {d_{xn}}^2 - 2\mu_{\mathbf{x}}^u \left(\sum_{m=1}^{M} x_m + \sum_{n=1}^{N} d_{xn}\right) + (M+N)\,\mu_{\mathbf{x}}^{u2} \\ &= \sum_{m=1}^{M} {x_m}^2 + \sum_{n=1}^{N} {d_{xn}}^2 - (M+N)\,\mu_{\mathbf{x}}^{u2} \end{aligned} \tag{5.19}$$

Similarly, auto moments-of-inertia of the updated *x*, *y*, and *z* coordinates are,

$$I_{yy}^{u} = \sum_{m=1}^{M} {y_m}^2 + \sum_{n=1}^{N} {d_{y_n}}^2 - (M+N)\,\mu_{\mathbf{y}}^{u2} \tag{5.20}$$

$$I_{zz}^{u} = \sum_{m=1}^{M} {z_m}^2 + \sum_{n=1}^{N} {d_{zn}}^2 - (M+N)\,\mu_{\mathbf{z}}^{u2} \tag{5.21}$$

5.6.1. Examination of Adding Single Sensor

Proposition: In order to extend any arbitrary linear or planar arrays into both azimuth and elevation isotropic volumetric arrays, we need at least one additional sensor.

Proof. Assume that this proposition is *true*.

If we add one additional sensor with $(\zeta_x, \zeta_y, \zeta_z)$ coordinate, then updated coordinates,

$$\begin{aligned} x^u &= [x_1, x_2, \ldots,\ x_M,\ \zeta_x] \\ y^u &= [y_1, y_2, \ldots,\ y_M,\ \zeta_y] \\ z^u &= [z_1, z_2, \ldots,\ z_M,\ \zeta_z] \end{aligned} \tag{5.22}$$

Cross moment-of-inertia of updated coordinates,

$$\begin{aligned} I^u_{xy} &= \sum_{m=1}^{M} x_m y_m + \zeta_x \zeta_y - (M+1)\,\mu^u_{\mathbf{x}}\mu^u_{\mathbf{y}} \\ I^u_{xz} &= \sum_{m=1}^{M} x_m z_m + \zeta_x \zeta_z - (M+1)\,\mu^u_{\mathbf{x}}\mu^u_{\mathbf{z}} \\ I^u_{yz} &= \sum_{m=1}^{M} y_m z_m + \zeta_y \zeta_z - (M+1)\,\mu^u_{\mathbf{y}}\mu^u_{\mathbf{z}} \end{aligned} \tag{5.23}$$

Auto moment-of-inertia of updated coordinates,

$$\begin{aligned} I^u_{xx} &= \sum_{m=1}^{M} {x_m}^2 + {\zeta_x}^2 - (M+1)\,\mu^{u2}_{\mathbf{x}} \\ I^u_{yy} &= \sum_{m=1}^{M} {y_m}^2 + {\zeta_y}^2 - (M+1)\,\mu^{u2}_{\mathbf{y}} \\ I^u_{zz} &= \sum_{m=1}^{M} {z_m}^2 + {\zeta_z}^2 - (M+1)\,\mu^{u2}_{\mathbf{z}} \end{aligned} \tag{5.24}$$

If an array holds (3.3) and (3.4) constraints, then this array has both azimuth and elevation isotropic DOA estimation performance. Then common solution sets of the following nonlinear equations give added sensor coordinates $(\zeta_x, \zeta_y, \zeta_z)$,

$$
\begin{aligned}
I^u_{xx} - I^u_{yy} &= 0 \\
I^u_{xx} - I^u_{zz} &= 0 \\
I^u_{xy} &= 0 \\
I^u_{xz} &= 0 \\
I^u_{yz} &= 0
\end{aligned}
\tag{5.25}
$$

Whereas there is no always a common solution for this set of equations. Therefore, we have reached a *contradiction*. This means that we need at least two additional sensors to extend any given linear or planar arrays that satisfy 2-D isotropy conditions.

5.6.2. Simulations for Contradiction

In this section, a new sensor is added to the coordinates obtained by the common solution of the nonlinear equation set given in (5.25) for a given array to have 2-D isotropic performance. As an example, a volumetric array (cubic array with missing sensor shown in Figure 5.11(a)) and the UCA, as shown in Figure 5.11(b), are used. UCAs with different numbers of sensors were tested to prove that the minimum number of additional sensors should be $N = 2$ for the proposed design method. As a result of trials, it is seen that (5.25) does not always have a solution. Therefore, the use of at least two sensors is optimum for our proposed design method. However, interestingly, for some UCAs with different sensor numbers, it is sufficient to add a single sensor to satisfy isotropic conditions.

The elements of sensor array geometries are located in $\mathbb{R}^3$ and are used to estimate the DOA of the single far-field narrow-band source signal. $\Psi = [\phi, \theta]^T$ denotes DOAs of the source signal, where $\phi \in [0, 180°]$ and $\theta \in [0, 90°]$ represent its azimuth and elevation angles, respectively, as demonstrated in Figure 2.2. Simulation of each array is fulfilled for the following parameter settings; The number of snapshots $T = 256$, SNR=5 dB, and $f_c = 500$ MHz.

In order to test the performance of the arrays, we use the CRLB. The azimuth and elevation DOA estimation performance comparisons of the cubic array with a missing sensor and completed version are shown in Figures 5.12(a) and (b). As expected, when the missing sensor is added, both azimuth and elevation performances are isotropic since the array provides the 2-D isotropy conditions. On the other hand, for a UCA of $M = 6$ sensors, adding an $N = 1$ sensor has a solution to (5.25). Therefore, by adding a single sensor to this array, 2-D isotropy conditions are fulfilled. This result is confirmed by simulations, as shown in Figures 5.13(a) and (b). As seen in Figure 5.13(a), the azimuth estimation performance of the given UCA is isotropic. In the case of adding a new sensor, it is seen that the azimuth isotropic structure of the array has not deteriorated. On the contrary, with only adding one sensor, the elevation estimation performance becomes isotropic, as seen in Figure 5.13(b).

Note that for $M = 5$ or some other values, (5.25) does not have a solution. Therefore, the only way to make isotropy by extending any given arrays is to add at least $N = 2$ sensors. This shows that the array extension approach based on the addition of at least two sensors proposed in this chapter is optimal.

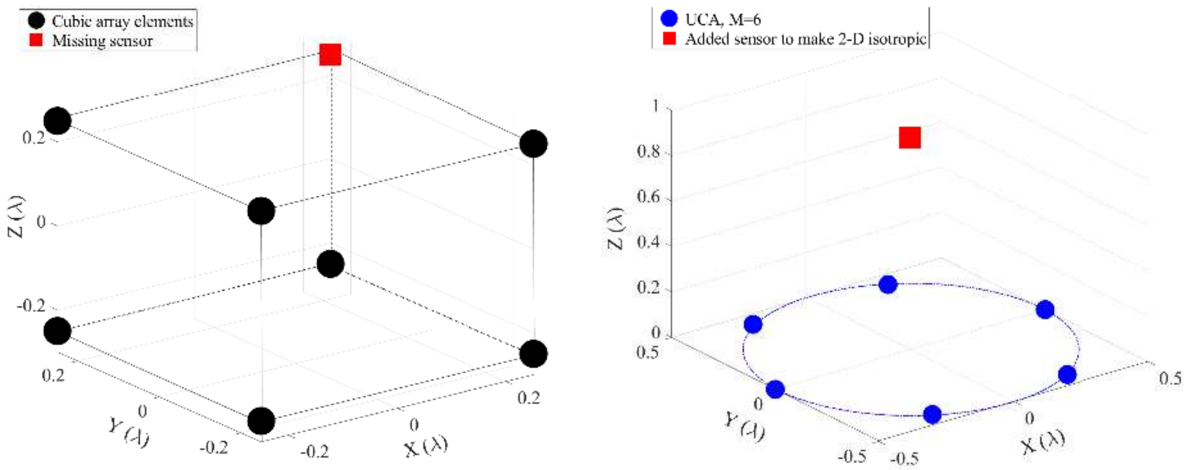

(a) (b)

Figure 5.11: (a) Cubic Array and (b) UCA.

5.7. DOA Estimation via Swarm of UAVs: A Case Study of Airborne DF System

The swarm of autonomous unmanned aerial vehicles (UAVs, Drones) can work together to achieve a specific goal [67–74]. Swarm of UAVs has a wide range of applications for security, survey, monitoring, and surveillance of a wide area. They also planned to be used for disaster management, search, and rescue operations. It is also possible to use multiple UAVs for localization and DOA estimation of moving targets. In this chapter, we defined a scenario where a group of UAVs is coordinated for DOA estimation. Localization of emitters with unknown locations is an important requirement and known as hidden target localization.

In this chapter, we considered multiple airborne (dynamic) UAVs as volumetric sensor arrays for 2-D DOA estimation of hidden emitters.

5.7.1. Modeling The Swarm UAVs-based Sensor Array Formation

In this scenario, it is necessary to scan a restricted area of 2 km $\times$ 2 km with a swarm of M UAVs for surveillance purposes. We assumed that an identical isotropic antenna is mounted on each UAV of the swarm. The scenario is defined as follows,

- A1. Swarm UAVs start spontaneously to take off from their initial positions on the helipad from an area of 10 m $\times$ 10 m.
- A2. The M, the number of UAVs in the swarm, is determined by the designated mission requirements.
- A3. The swarm elements' positions, including the leader, in the next desired formation, are known in advance during the re-formation phases.
- A4. In the flight zone, there are no obstacles. The ultrasonic sensors are assumed to prevent collisions of swarm elements with each other and with the target.
- A5. The swarm elements are slightly faster than the target UAV, and the swarm speed changes according to the target speed.
- A6. A magnetometer and barometer are used to very accurately measure movement and altitude in real-time, respectively.
- A6. The Global Positioning System (GPS) is used for swarm formation stabilization, swarm member localization, and path planning.

The proposed approach consists of a four-phase design framework: Initial Phase, Surveillance Phase, Tracking (Localization) Phase, and Intervention Phase as follows,

1. UAVs are ready to take off from arbitrary initial positions as previously stated in the A1.

2. During the surveillance phase, 3-D swarm UAVs formation flies with 2-D isotropic DOA estimation performance. The formation geometry of the swarm UAVs chosen for this particular problem is the tetrahedron array.

3. In the tracking phase, ULA formation is preferred for high array directivity and low CRLB level. According to the azimuth and elevation DOA angles of the target, the ULA formation rotates towards the target UAV to hold it always on the broad-side.

4. For the intervention phase, the UCA formation is started to surround the target. After a predetermined secure range from the target, the swarm begins the intervention phase.

In order to formulate the collide distance (also MC) and array's angle ambiguity constraints, the distance between the i$^{\text{th}}$ and j$^{\text{th}}$ UAVs are defined as follow,

$$d_{ij} = \|\mathbf{p}_i - \mathbf{p}_j\|, \; \forall_{i,j} \in \{1, \ldots, K\}, i \neq j \tag{5.26}$$

Therefore, collide distance and angle ambiguity constraints are,

$$d_{safe} = \frac{\lambda}{4} \leq d_{ij} \leq \lambda = d_{amb.} \tag{5.27}$$

5.7.2. Re-formations and Steady Formations of Swarm UAVs

We use an efficient position assignment method to ensure that each UAV in the swarm is placed in its predetermined positions with the total shortest path during re-formation phases. In other words, we determine which position each UAV will go to in the next formation to reduce the total path of the swarm elements as they move to their new location during the re-formation.

Here we use the Jonker-Volgenant (JV) global nearest neighbor assignment algorithm [75] given in (5.28) as follows, which has lower computational complexity than the others in the literature [67], ensuring the swarm paths have the shortest total path in re-formation phases.

$$
\begin{aligned}
\min_{s} : & \sum_{i=1}^{K}\sum_{j=1}^{K}\mathbf{D}_{ij}\mathbf{S}_{ij} \\
\text{subject to} : & \sum_{j=1}^{K}\mathbf{S}_{ij} = 1 \quad (i = 1, \ldots, K) \\
& \sum_{i=1}^{K}\mathbf{S}_{ij} = 1 \quad (j = 1, \ldots, K) \\
& \mathbf{S}_{ij} \geq 1 \quad (i, j = 1, \ldots, K)
\end{aligned}
\tag{5.28}
$$

where $\mathbf{S}_{ij}$ represents the UAVs' assignment status. Therefore, it indicates that with 1, the UAV is assigned to a certain position in the next formation, or with 0 that it is not assigned to any position.

$$
\mathbf{S}_{ij} = \begin{cases} 1, & \text{if } i^{\text{th}} \text{ UAV assign to } j^{\text{th}} \text{ position} \\ 0, & \text{otherwise} \end{cases}
\tag{5.29}
$$

where subscripts *i* and *j* represent UAVs' locations in the current and next swarm formation (i.e., row and column of the distance matrix, $\mathbf{D}$), respectively.

Swarm elements' total path reduced by 15.4% during the re-formation from initial to surveillance phase, as shown in Figure 5.14. Therefore, the same reduction in energy consumption was achieved.

The transition equation from the initial location to the final location, i.e., movement of each UAV along its direction vector, is defined for the steady flight and re-formation phases as follow,

$$
\mathbf{P}_{current}^{des.} = \mathbf{P}_{start}^{jv} + t\left(\mathbf{P}_{end}^{jv} - \mathbf{P}_{start}^{jv}\right), \ (t = 0, \ \ldots, \ 1)
\tag{5.30}
$$

where $\mathbf{P}_{start}^{jv}$ and $\mathbf{P}_{end}^{jv}$ represent that the start and end coordinates are sorted with optimum pairing using (5.28). $\mathbf{P}_{current}^{des.}$ denotes UAVs' current positions.

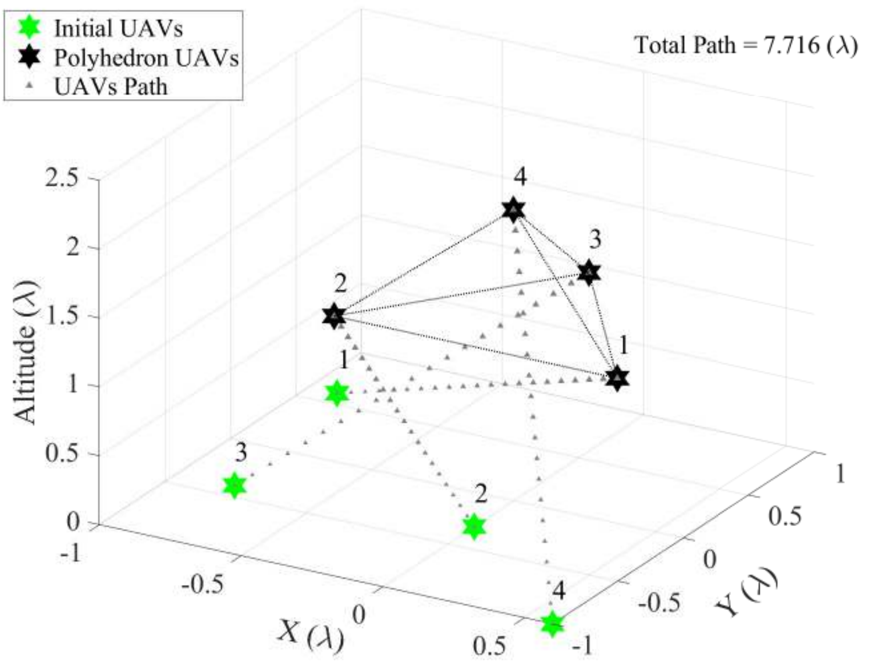

(a)

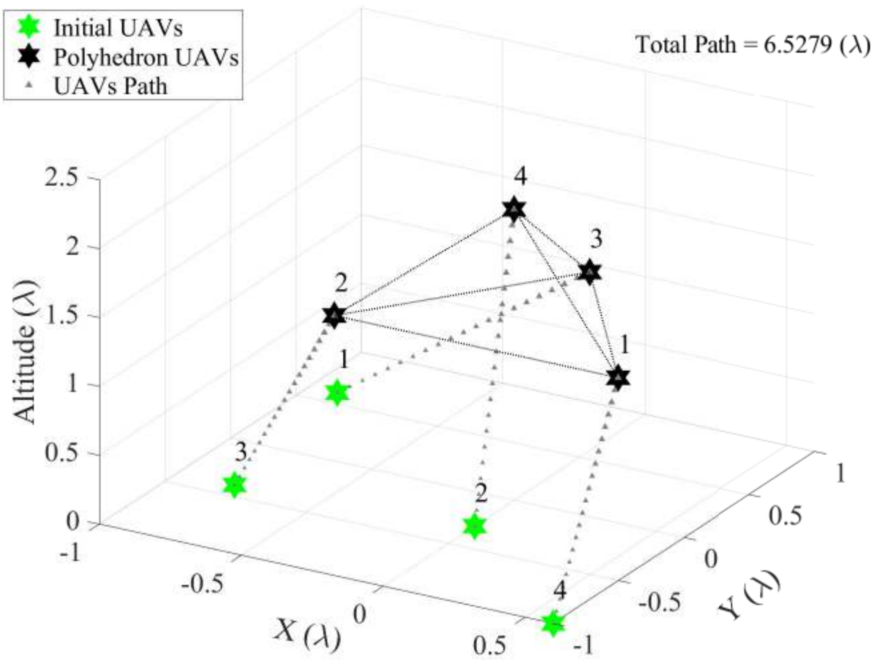

(b)

Figure 5.14: Initial to Polyhedron re-formation with (a) non-optimal pairing and (b) optimum pairing.

5.7.3. Polyhedron Swarm UAVs Surveillance Phase

In our scenario, during the surveillance flight, the swarm UAVs have uniform rectilinear motion, and they follow a semi-circle trajectory in the turning phase. Furthermore, the target has a curvilinear motion with variable-velocity. Note that the swarm preserves the formation of polyhedron throughout the surveillance flight. The UAV swarm simultaneously searches for any threatening target during the surveillance flight using the 2-D MUSIC algorithm (2.24). We chose the polyhedron form for swarm UAVs formation in the surveillance phase since it has a 2-D isotropic DOA estimation performance. This means it does not matter where the target is because tetrahedron formation with isotropic formation can estimate the DOA of the target with an equal error level regardless of where the target is.

5.7.4. ULA Swarm UAVs Target Tracking Phase

Once the target is detected during the surveillance, the swarm changes its formation from tetrahedron to ULA. The main reason for doing this is that the ULA formation tries to keep the target on the broadside when the first instant target's direction is detected. In this case, the ULA formation moves towards the target by estimating only the azimuth angle with high accuracy when the elevation angle is now low. Then the swarm rotates around the y and z coordinates of the ULA's local coordinate system in order to keep its flight towards the target continuously concerning this 2-D angle knowledge. To be more precise, the swarm velocity vector is always directed towards the target in the pure pursuit of guidance, and the turn rate of the swarm is always kept equal to the Line of Sight (LOS) turn rate. In summary, the swarm UAVs always flies directly towards the target along its pure pursuit trajectory. Thus, the swarm UAVs' direction is preserved by 2-D DOA angle knowledge along the LOS between the swarm and the target. As ULA is considered to be on the x-axis on the swarm's relative coordinate system, only the rotation matrices around the y and z-axes are given as follows, respectively.

$$R_y(\theta_u) = \begin{bmatrix} \cos\theta_u & 0 & \sin\theta_u \\ 0 & 1 & 0 \\ -\sin\theta_u & 0 & \cos\theta_u \end{bmatrix} \tag{5.31}$$

$$R_z(\phi_u) = \begin{bmatrix} \cos\phi_u & -\sin\phi_u & 0 \\ \sin\phi_u & \cos\phi_u & 0 \\ 0 & 0 & 1 \end{bmatrix} \tag{5.32}$$

Since the swarm UAVs in ULA formation follows the direction vector of the target, the direction of flight changes according to the target's DOA angles. Recall (5.30) as,

$$\mathbf{P}^{des.}_{current} = \left(\mathbf{P}^{jv}_{ULA} + t\left(\mathbf{P}^{jv}_{end} - \mathbf{P}^{jv}_{ULA}\right)\right) R_y(\theta_u) R_z(\phi_u) \tag{5.33}$$

The Swarm begins to re-formation from the ULA to the UCA formation phase after reaching a predetermined safe distance from the target.

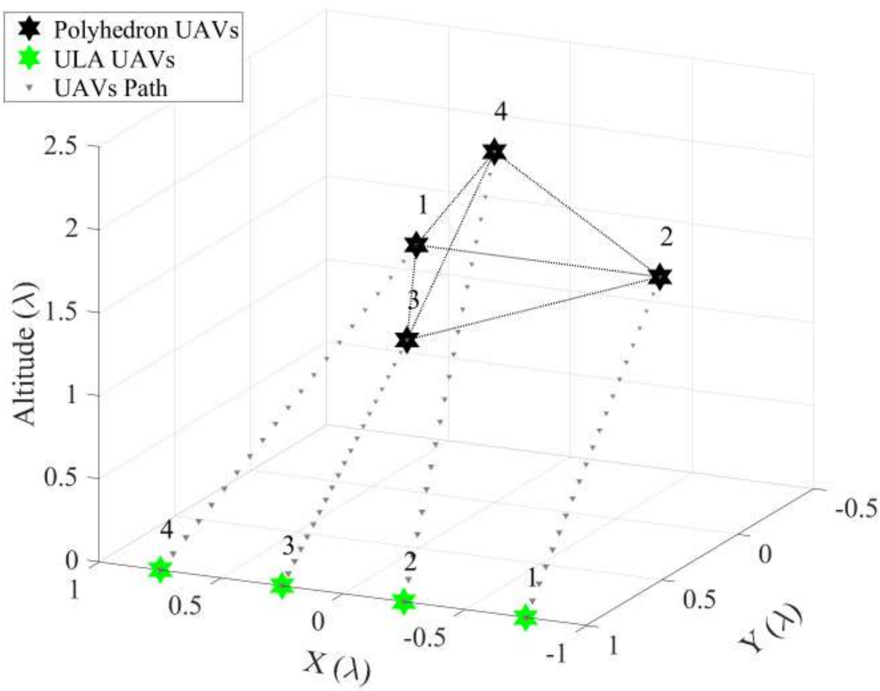

Figure 5.15: Tracking phase: Polyhedron to ULA re-formation when the target detected first.

5.7.5. UCA Swarm UAVs Target Intervention Phase

The UCA formation surrounds the target as the swarm reaches a predetermined safe distance. Figure 5.16 shows the transition of the swarm from the ULA to the UCA formation. At this phase, it is assumed that the ultrasonic sensors determine the target's distance to each UAV. Surrounding the target is carried out to provide mandatory prevention of the target.

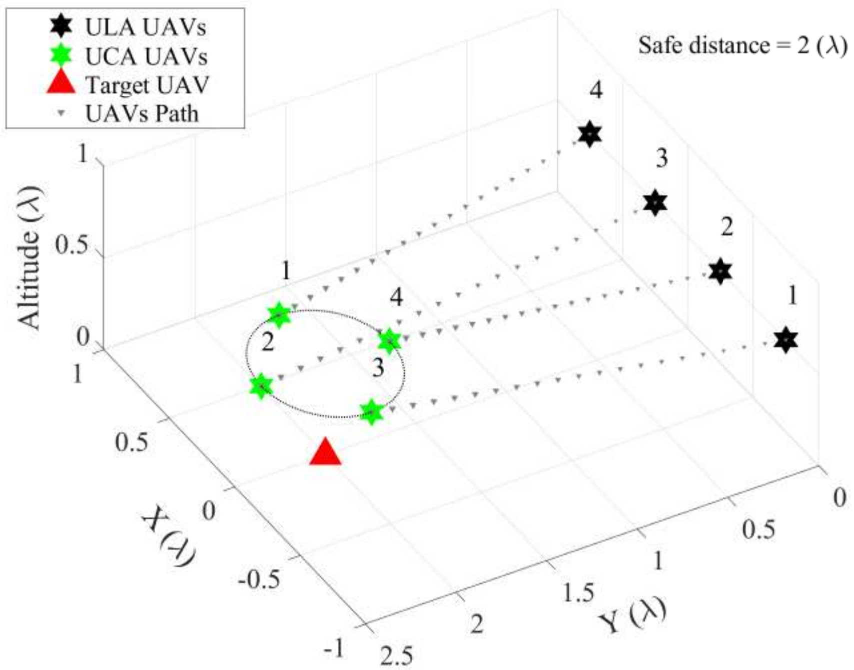

Figure 5.16: Intervention phase:ULA to UCA re-formation when getting close to the target with 2 λ safe distance.

5.7.6. Simulation Results

This section simulates a swarm UAVs-based sensor array that carries out the detection, tracking, and intervention of an unwelcome target in a restricted area. The results are presented in order to illustrate the efficiency of the proposed method.

The swarm UAVs-based sensor array elements consisting of $M = 4$ UAVs are located in $\mathbb{R}^3$ with $d = \lambda/2$ distancing and is used to estimate the DOA of the single far-field narrow-band target's signal. $(\phi_u,\ \theta_u)$ denotes DOAs of the target signal, where $\phi_u \in [0, 180°]$ and $\theta_u \in [0, 90°]$ represent its azimuth and elevation angles, respectively, as demonstrated in Figure 2.2. Simulations throughout the scenario are fulfilled for the following parameter settings; The number of snapshots $T = 256$, SNR=20 dB, and $f_c = 500$ MHz.

First, we examine the azimuth and elevation CRLB performances of the swarm UAVs-based sensor arrays to explain the reason for the flight formation choice at each phase. While the azimuth performance of the swarm formation is obtained, the elevation angle of the target is kept at a certain angle, and the azimuth angle is scanned from $0°$ to

$180°$. Similarly, while obtaining elevation performance, the azimuth angle of the source is kept at a certain angle, and the elevation angle is scanned from $0°$ to $90°$. Figure 5.17 shows swarm UAVs-based sensor arrays' the azimuth and elevation CRLB levels at each phase. Figure 5.17(a) shows the azimuth performance of the arrays when the elevation angle of the source is fixed at $80°$, and Figure 5.17(b) shows the elevation performance of the arrays when the azimuth angle of the source is fixed at $20°$.

As shown in Figure 5.17(b), the elevation estimation errors go to infinity for the linear and planar arrays when the elevation angle approaches $90°$. Nevertheless, tetrahedron formation has 2-D isotropic DOA estimation performance. For this reason, volumetric 2-D isotopic arrays are most suitable for surveillance purposes. Moreover, ULA formation has the lowest estimation error when the target is on broadside with zero elevation. For this reason, the ULA is most suitable for target tracking.

The proposed approach follows a design framework that implements four phases: Initial, Surveillance, Tracking (Localization), and Intervention phases, as seen in Figures 5.14, 5.15, and 5.16. Firstly, it is assumed that UAVs wait on their arbitrary initial positions in a specific field. Then they pass to tetrahedron formation in order to initiate the surveillance phase with the shortest total path by JV algorithm. A surveillance flight will be performed via the 2-D isotropic swarm UAVs-based sensor array formation in this phase. Figure 5.18 shows the 2-D MUSIC spectrum when the target is detected for the first time with the swarm UAVs-based sensor array in tetrahedron formation. In case of detection of any target, tracking is initiated by rotating LOS of the array to the target by (5.33) using azimuth and elevation angle information received from the 2-D MUSIC algorithm given in (2.24). Rotations are made instantly concerning this angle information during target tracking. The swarm UAVs-based sensor array initiates the intervention phase and alters its formation to UCA formation in order to surround the target when approaching the target within a predetermined distance. Figure 5.19 illustrates all phases of the scenario.

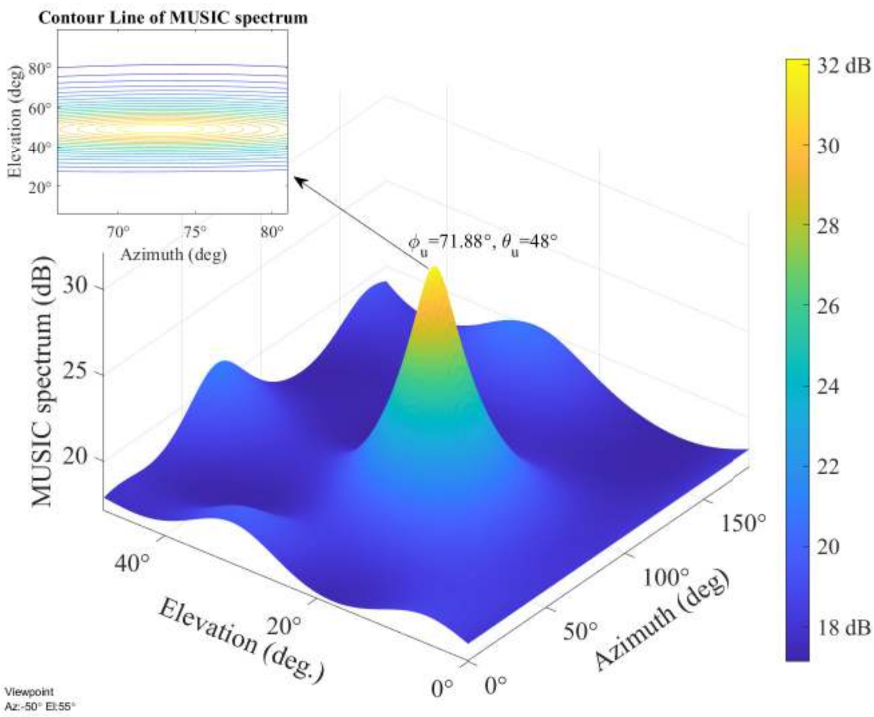

Figure 5.18: 2-D MUSIC spectrum for swarm UAVs-based sensor array in a tetrahedron formation.

Figure 5.18 shows that the undesired target enters the forbidden area at $\phi_u = 71.88°$ and $\theta_u = 48°$ with respect to the swarm UAVs-based sensor array coordinate system. Note that the target has a curvilinear motion with variable-velocity. As shown in Figures 5.17(a) and (b), at all azimuth and elevation angles, a swarm UAVs-based sensor array in tetrahedron formation has 2-D isotropic DOA estimation performance with equal error level. Therefore, the DOA angle at which the target enters the restricted area will not affect the array's performance. Moreover, when the target enters the no-fly zone area with a clear boundary violation, the swarm UAVs-based sensor array in polyhedron form will immediately alter its formation to ULA formation with optimum path re-formation and take the target to the broadside. And it performs target tracking with high sensor array gain and low estimation error. As shown in Figure 5.17(a), ULA has a minimum azimuth CRLB level at $90°$, i.e., broadside, so it performs more accurate DOA estimation performance than other arrays.

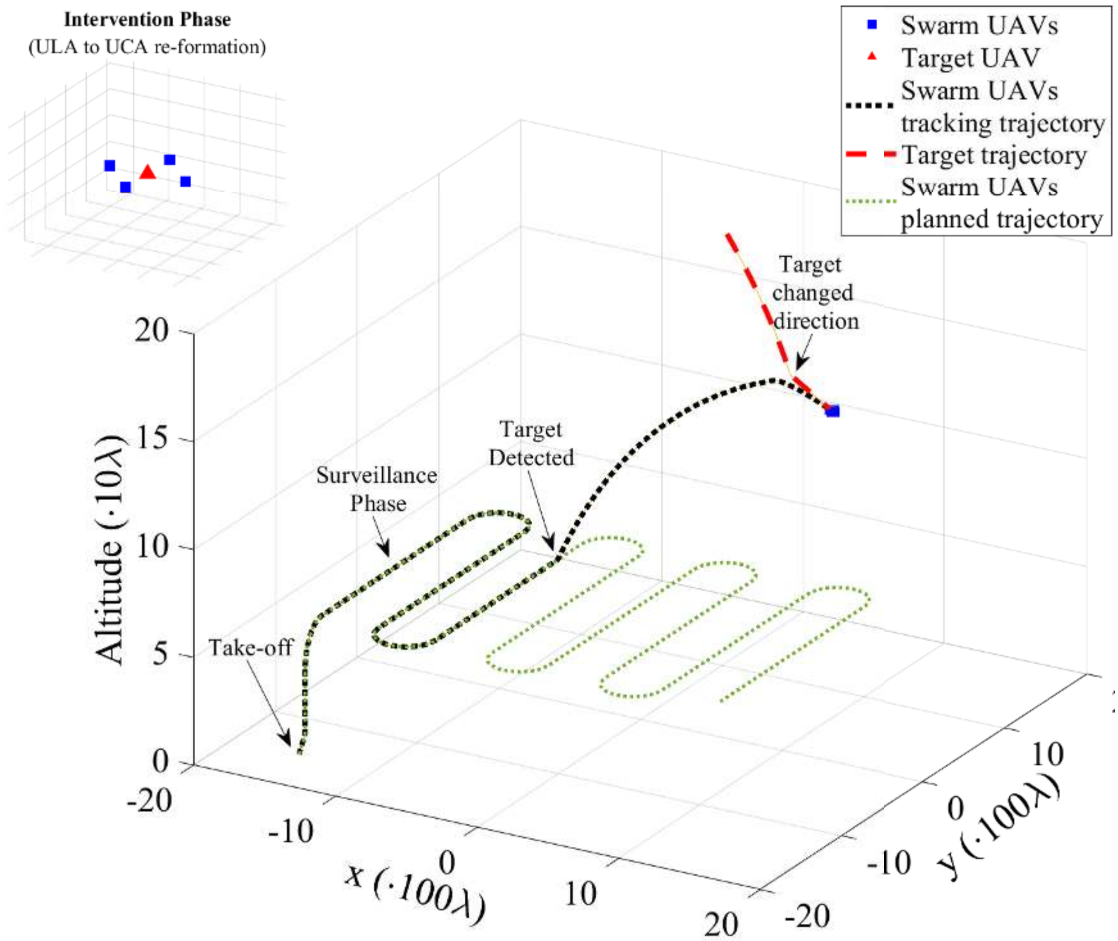

Figure 5.19: Simulation scenario for swarm UAVs-based sensor array: 2-D DOA estimation of an undesired target, tracking, and intervention.

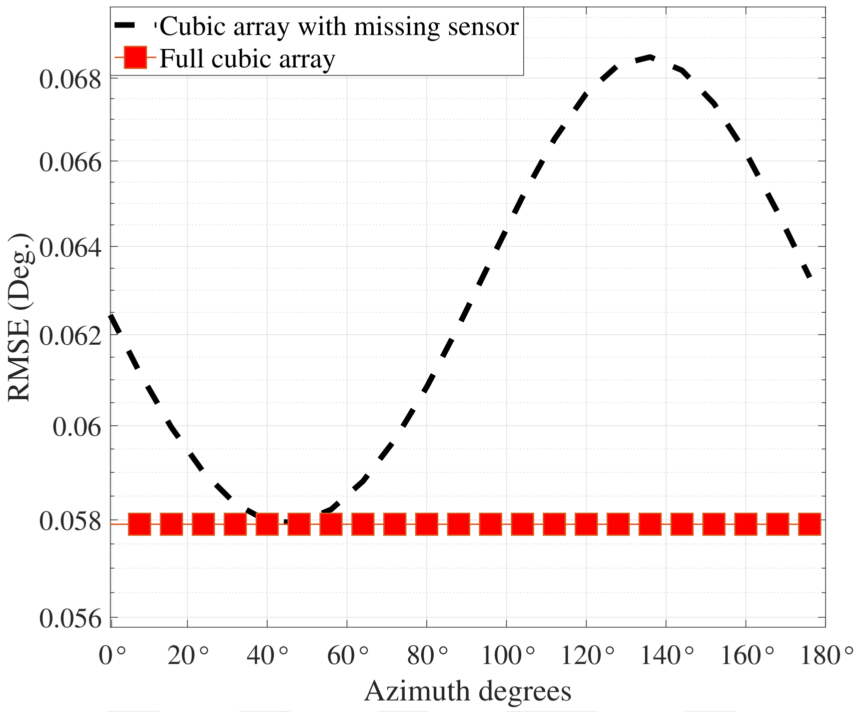

(a)

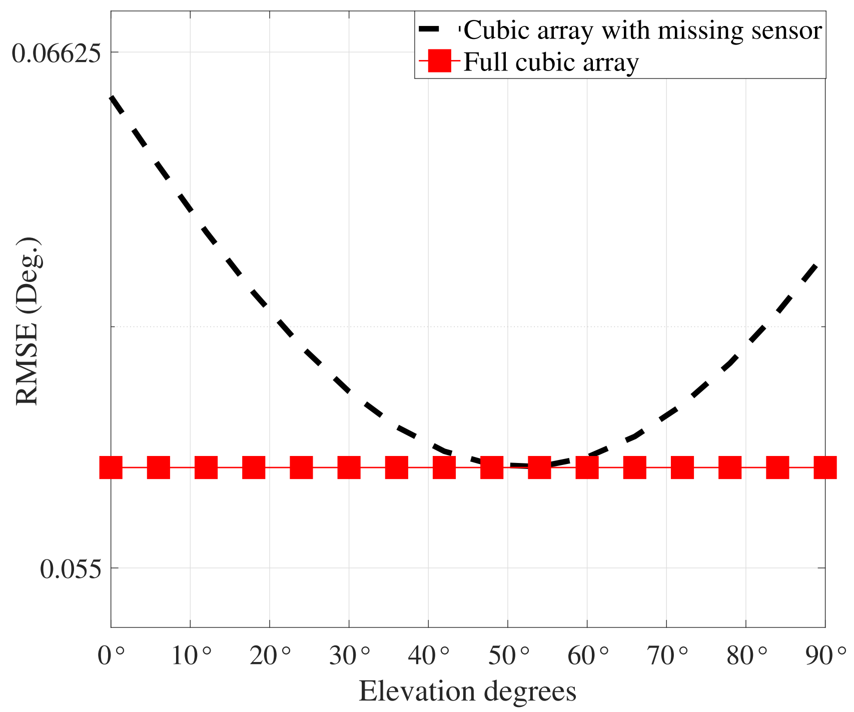

(b)

Figure 5.12: CRLB results for Cubic Array: (a) Azimuth Performance ($\theta = 85°$) (b) Elevation performance ($\phi = 15°$).

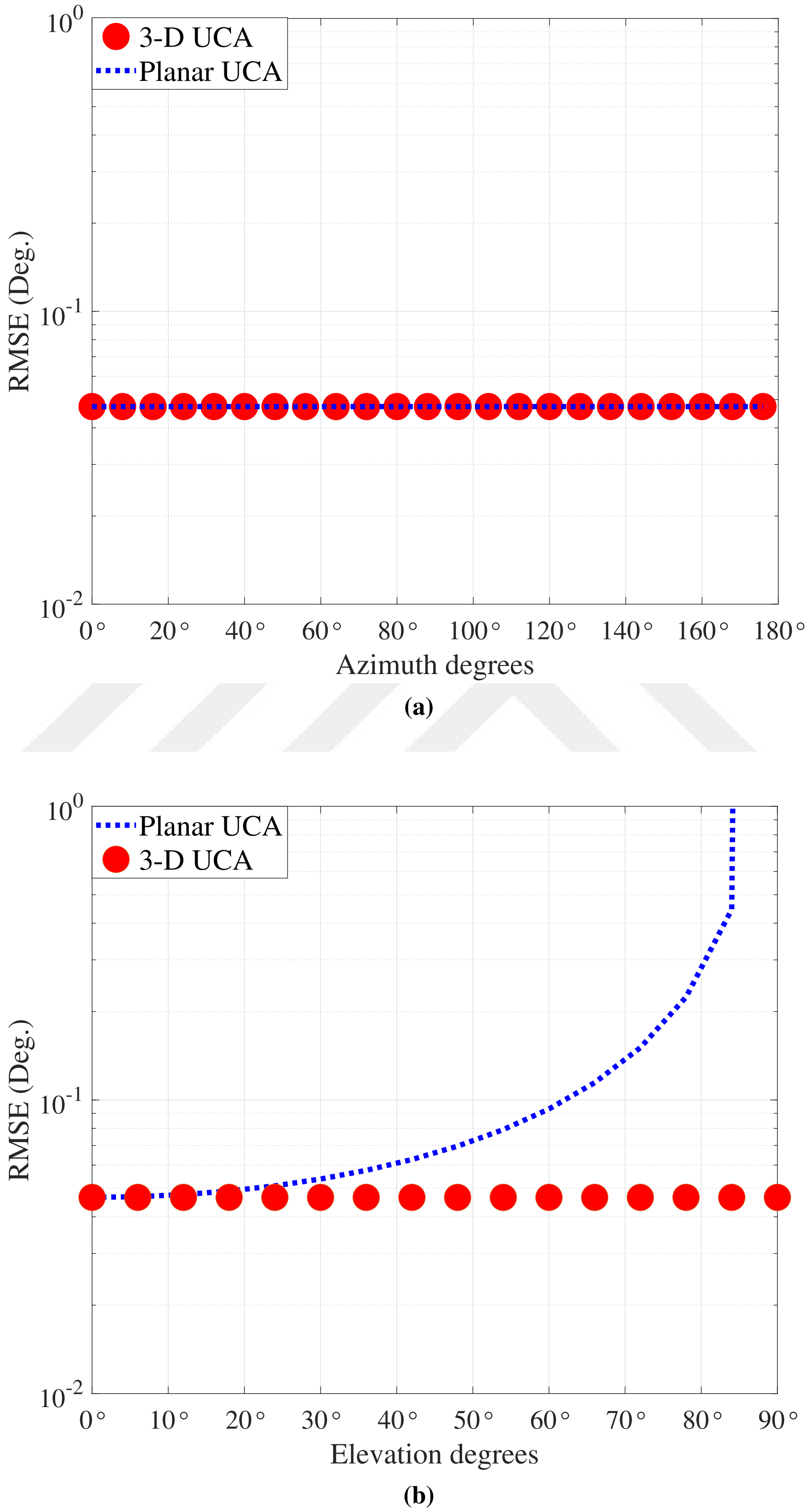

Figure 5.13: CRLB results for 3-D UCA: (a) Azimuth Performance ($\theta = 85°$) (b) Elevation performance ($\phi = 15°$).

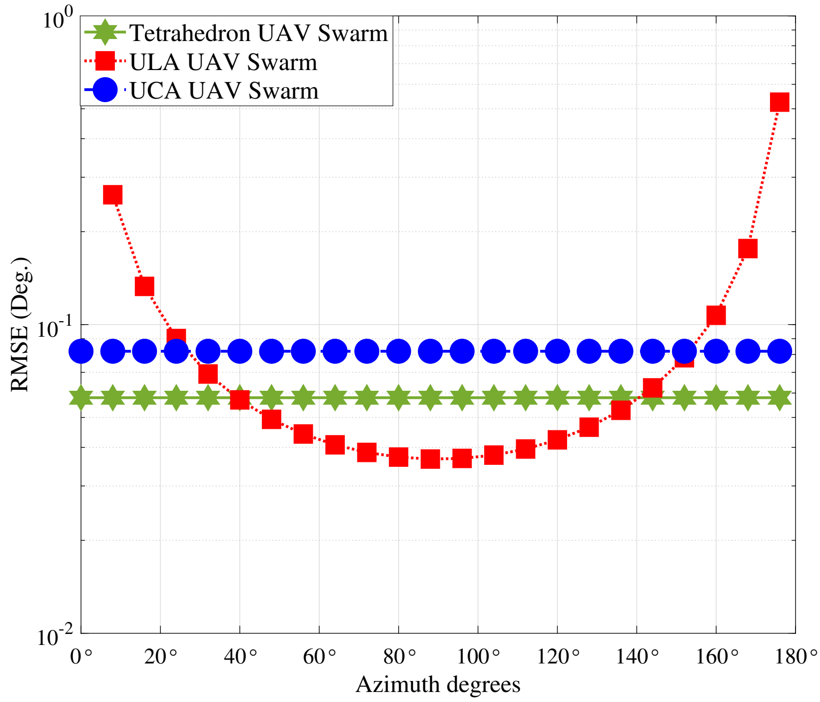

(a)

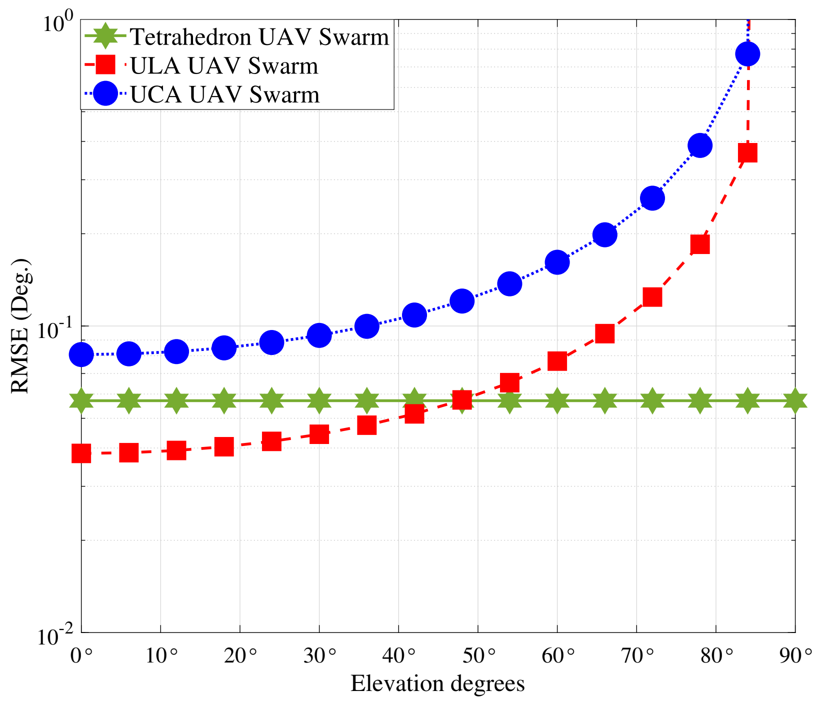

(b)

Figure 5.17: CRLB results of each phase: (a) Azimuth performances ($\theta_{fix} = 80°$) (b) Elevation performances ($\phi_{fix} = 20°$).

6. CONCLUSION

Nowadays, DF systems need not only azimuth but also elevation DOA estimation. Especially in mobile wireless communication, mobile users are in high buildings or underground, or DOA estimation is important in all directions when it comes to UAVs.

In this thesis, 3-D sensor array geometry designs with both azimuth and elevation DOA estimation performance are discussed from different perspectives. In the first design method, a new 3-D V-shaped array is created by combining two of the V-shaped planar array, which has been investigated extensively in terms of azimuth isotropy in the literature. The angles between the sub-arrays and the planes of the V-shaped arrays in the created array have been optimized to meet the 2-D isotropy conditions. It is known that adding a sensor to the z-axis improves elevation estimation performance. However, it could not provide a fully isotropic 2-D DOA estimation performance. Thus, fewer sensors were used in the second design method than in the previous method to extend the V-shaped planar array. The positions of the sensors to be added in this method are obtained analytically. The resulting new 3-D V-shaped array, in this case, provided fully 2-D isotropic DOA estimation performance.

A 3-D extension method is proposed for centrosymmetric planar sensor array geometries that already have azimuth isotropic DOA estimation performance. This method adds new sensors symmetric to the origin with equal inter-element spacing to the z-axis under isotropy conditions. With the addition of these sensors, the planar sensor arrays are transformed into a 3-D array with 2-D isotropic DOA estimation performance. Then, in the fourth design method, we present a design procedure that transforms all linear/planar sensor arrays into 3-D arrays with 2-D isotropic DOA estimation performance by adding the least number of new sensors. The newly added sensors have been added under the constraints of MC and angle ambiguity. Moreover, the contradiction proof method is utilized to verify that adding at least two sensors is optimal.

As a final study, an airborne DF scenario is considered for intelligence, surveillance, and reconnaissance purposes with 3-D sensor array-based swarm UAVs.

A. APPENDIX A

A.1. V-shaped Array Equations for Section 3.2

In this appendix, we derive closed-form expressions for the equations between (3.16) and (3.26). $k_1 = \frac{M+3}{4}$ and $k_2 = \frac{3M+5}{4}$ are the reference sensor index of the first and second planar V-Shaped sensor arrays, respectively.

$$\sum_{m=1}^{\frac{M+1}{2}} (m-k_1) = \sum_{m=1}^{\frac{M+1}{2}} \left(m - \frac{M+3}{4}\right) = 0 \tag{A.1}$$

$$\sum_{m=\frac{M+3}{2}}^{M+1} (m-k_2) = \sum_{m=\frac{M+3}{2}}^{M+1} \left(m - \frac{3M+5}{4}\right) = 0 \tag{A.2}$$

$$\sum_{m=1}^{\frac{M+1}{2}} |m-k_1| = \sum_{m=1}^{\frac{M+1}{2}} \left|m - \frac{M+3}{4}\right| = \frac{(M-1)(M+3)}{16} \tag{A.3}$$

$$\sum_{m=\frac{M+3}{2}}^{M+1} |m-k_2| = \sum_{m=\frac{M+3}{2}}^{M+1} \left|m - \frac{3M+5}{4}\right| = \frac{(M-1)(M+3)}{16} \tag{A.4}$$

$$\begin{aligned}\sum_{m=1}^{\frac{M+1}{2}} (m-k_1)^2 &= \sum_{m=1}^{\frac{M+1}{2}} \left(m - \frac{M+3}{4}\right)^2 = \sum_{m=1}^{\frac{M+1}{2}} m^2 - 2\left(\frac{M+3}{4}\right)\sum_{m=1}^{\frac{M+1}{2}} m + \sum_{m=1}^{\frac{M+1}{2}} \left(\frac{M+3}{4}\right)^2 \\ &= \frac{\left(\frac{M+1}{2}\right)\left(\frac{M+1}{2}+1\right)\left(2\frac{M+1}{2}+1\right)}{6} - 2\left(\frac{M+3}{4}\right)\frac{\left(\frac{M+1}{2}\right)\left(\frac{M+1}{2}+1\right)}{2} \\ &\quad - \left(\frac{M+3}{4}\right)^2\left(\frac{M+1}{2}\right) = \frac{(M-1)(M+1)(M+3)}{96}\end{aligned} \tag{A.5}$$

$$\begin{aligned}\sum_{m=\frac{M+3}{2}}^{M+1} (m-k_2)^2 &= \sum_{m=\frac{M+3}{2}}^{M+1} \left(m - \frac{3M+5}{4}\right)^2 = \sum_{m=\frac{M+3}{2}}^{M+1} m^2 - 2\left(\frac{3M+5}{4}\right)\sum_{m=\frac{M+3}{2}}^{M+1} m \\ &\quad + \sum_{m=\frac{M+3}{2}}^{M+1} \left(\frac{3M+5}{4}\right)^2 = \frac{(M-1)(M+1)(M+3)}{96}\end{aligned} \tag{A.6}$$

$$\sum_{m=1}^{M} {y_m}^2 = d^2\cos^2\left(\frac{\gamma_1}{2}\right)\sum_{m=1}^{\frac{M+1}{2}} (m-k_1)^2 + d^2\cos^2\left(\frac{\gamma_2}{2}\right)\cos^2(\beta)\sum_{m=\frac{M+3}{2}}^{M+1} (m-k_2)^2 \tag{A.7}$$

Substituting (A.5) and (A.6) into (A.7) gives,

$$\sum_{m=1}^{M} {y_m}^2 = \frac{d^2}{96}\left(M-1\right)\left(M+1\right)\left(M+3\right)\left(\cos^2\left(\frac{\gamma_1}{2}\right)+\cos^2\left(\frac{\gamma_2}{2}\right)\cos^2\left(\beta\right)\right) \quad \text{(A.8)}$$

$$\sum_{m=\frac{M+3}{2}}^{M+1} {z_m}^2 = \sum_{m=\frac{M+3}{2}}^{M+1} \left(m-k_2\right)^2 d^2 \cos^2\left(\frac{\gamma_2}{2}\right)\sin^2\left(\beta\right) \quad \text{(A.9)}$$

Substituting (A.6) into (A.9) gives,

$$\sum_{m=\frac{M+3}{2}}^{M+1} {z_m}^2 = \frac{d^2}{96}\left(M-1\right)\left(M+1\right)\left(M+3\right)\cos^2\left(\frac{\gamma_2}{2}\right)\sin^2\left(\beta\right) \quad \text{(A.10)}$$

A.2. V-shaped Array Equations for Section 3.3

In this appendix, we derive closed-form expressions for the equations between (3.31) and (3.36). $k = \frac{M+1}{2}$ is the reference sensor index of the planar V-Shaped sensor array, respectively.

$$\sum_{m=1}^{M}\left(m-k\right) = \sum_{m=1}^{M}\left(m-\frac{M+1}{2}\right) = 0 \quad \text{(A.11)}$$

$$\sum_{m=1}^{M}\left|m-k\right| = \sum_{m=1}^{M}\left|m-\frac{M+1}{2}\right| = \left\lceil\frac{M^2-1}{4}\right\rceil \quad \text{(A.12)}$$

$$\begin{aligned}\sum_{m=1}^{M}\left(m-k\right)^2 &= \sum_{m=1}^{M}\left(m-\frac{M+1}{2}\right)^2 \\ &= \left(\frac{1-M}{2}\right)^2+\left(\frac{3-M}{2}\right)^2+\cdots+\left(\frac{-3}{2}\right)^2+\left(\frac{-1}{2}\right)^2 \\ &+\left(\frac{1}{2}\right)^2+\left(\frac{3}{2}\right)^2+\cdots+\left(\frac{M-3}{2}\right)^2+\left(\frac{M-1}{2}\right)^2 \\ &= \frac{1}{2}\left(1^2+3^2+5^2\cdots+\left(M-1\right)^2\right)\end{aligned} \quad \text{(A.13)}$$

By using Sums of Squares of Consecutive Odd Integers formula, we obtain

$$\sum_{m=1}^{M}\left(m-k\right)^2 = \frac{1}{12}M\left(M^2-1\right) \quad \text{(A.14)}$$

B. APPENDIX B

B.1. 3-D UCA's Proofs

Note that the proofs given in the Appendix B.1.1 and B.1.2 are also validate for *y* coordinate.

B.1.1. Proof of (4.14)

Substituting (4.10) into (3.13) gives,

$$\begin{aligned}\mu_{\mathbf{x}} = \frac{1}{M}\sum_{m=1}^{M} x_m &= \frac{1}{M}\sum_{m=1}^{M} \frac{d\cos\left(\frac{2\pi(m-1)}{M}\right)}{\sqrt{2\left(1-\cos\left(\frac{2\pi}{M}\right)\right)}} \\ &= \frac{d}{M\sqrt{2\left(1-\cos\left(\frac{2\pi}{M}\right)\right)}}\sum_{m=1}^{M}\cos\left(\frac{2\pi\left(m-1\right)}{M}\right)\end{aligned} \tag{B.1}$$

Let rewrite the cosine term in the summation as the real part of exponential form as,

$$\sum_{m=1}^{M}\cos\left(\frac{2\pi\left(m-1\right)}{M}\right) = \Re\left\{\sum_{m=1}^{M} e^{\frac{j2\pi(m-1)}{M}}\right\} \tag{B.2}$$

Let $r = e^{\frac{j2\pi}{M}}$. Then this is very similar to the formula for the geometric series as,

$$\Re\left\{\sum_{m=1}^{M} r^{(m-1)}\right\} = \Re\left\{\frac{1-r^M}{1-r}\right\} = \Re\left\{\frac{1-\overbrace{e^{j2\pi}}^{1}}{1-e^{\frac{j2\pi}{M}}}\right\} = 0 \tag{B.3}$$

Substituting (B.3) into (B.1) gives,

$$\mu_{\mathbf{x}} = 0 \tag{B.4}$$

This completes the proof.

B.1.2. **Proof of** (4.11)

Substituting (4.10) into (3.8) gives,

$$I_{xx} = \sum_{m=1}^{M} (x_m - \mu_{\mathbf{x}})^2 = \frac{d^2}{2\left(1 - \cos\left(\frac{2\pi}{M}\right)\right)} \sum_{m=1}^{M} \cos^2\left(\frac{2\pi(m-1)}{M}\right) \tag{B.5}$$

By using double-angle trigonometric identity, $\cos^2(\alpha) = (1 + \cos(2\alpha))/2$, as,

$$\begin{aligned} \sum_{m=1}^{M} \cos^2\left(\frac{2\pi(m-1)}{M}\right) &= \sum_{m=1}^{M} \left(\frac{1}{2} + \frac{1}{2}\cos\left(\frac{4\pi(m-1)}{M}\right)\right) \\ &= \sum_{m=1}^{M} \frac{1}{2} + \sum_{m=1}^{M} \frac{1}{2}\cos\left(\frac{4\pi(m-1)}{M}\right) \end{aligned} \tag{B.6}$$

Let rewrite the cosine term in the summation as the real part of exponential form and by using the geometric series formula as,

$$\sum_{m=1}^{M} \cos\left(\frac{4\pi(m-1)}{M}\right) = \Re\left\{\sum_{m=1}^{M} e^{\frac{j4\pi(m-1)}{M}}\right\} = \Re\left\{\frac{1 - \overbrace{e^{j4\pi}}^{1}}{1 - e^{\frac{j4\pi}{M}}}\right\} = 0 \tag{B.7}$$

Now substitute back (B.7) into (B.6) and then (B.6) into (B.5), and do some trigonometric manipulation, finally we get,

$$I_{xx} = \frac{d^2}{2\left(1 - \cos\left(\frac{2\pi}{M}\right)\right)} \frac{M}{2} = \frac{1}{8} d^2 M \csc^2\left(\frac{\pi}{M}\right) \tag{B.8}$$

This completes the proof.

B.1.3. **Proof of** (4.18)

$$\mu_{\mathbf{z}} = \frac{1}{M} \sum_{m=1}^{M} z_m = \frac{d}{M+N} \sqrt{\frac{3M}{2N(N^2-1)}} \csc\left(\frac{\pi}{M}\right) \sum_{i=1}^{N} \left(\frac{(N+1)}{2} - i\right) \tag{B.9}$$

Let rewrite the summation part of (B.9) as,

$$\sum_{i=1}^{N} \left(\frac{(N+1)}{2} - i\right) = \sum_{i=1}^{N} \left(\frac{(N+1)}{2}\right) - \sum_{i=1}^{N} i = N\frac{(N+1)}{2} - N\frac{(N+1)}{2} = 0 \tag{B.10}$$

Now substitute back (B.10) into (B.9), we get,

$$\mu_{\mathbf{z}} = 0 \tag{B.11}$$

This completes the proof.

B.1.4. Proof of (4.19)

$$I_{zz} = \sum_{m=1}^{M} \left(z_m - \mu_{\mathbf{z}}\right)^2 = \frac{3Md^2}{2N\left(N^2-1\right)} \csc^2\left(\frac{\pi}{M}\right) \sum_{i=1}^{N} \left(\frac{(N+1)}{2} - i\right)^2 \tag{B.12}$$

Let rewrite the summation part of (B.12) as,

$$\begin{aligned} \sum_{i=1}^{N} \left(\frac{(N+1)}{2} - i\right)^2 &= \sum_{i=1}^{N} \left(\frac{(N+1)}{2}\right)^2 + \sum_{i=1}^{N} i^2 - \sum_{i=1}^{N} (N+1)\, i \\ &= \frac{N\,(N+1)^2}{4} + \frac{N\,(N+1)\,(2N+1)}{6} - \frac{N\,(N+1)^2}{2} \\ &= \frac{1}{12} N \left(N^2-1\right) \end{aligned} \tag{B.13}$$

Now substitute back (B.13) into (B.12), finally we get,

$$\begin{aligned} I_{zz} = \sum_{m=1}^{M} \left(z_m - \mu_{\mathbf{z}}\right)^2 &= \frac{3Md^2}{2N\left(N^2-1\right)} \csc^2\left(\frac{\pi}{M}\right) \frac{1}{12} N \left(N^2-1\right) \\ &= \frac{1}{8} d^2 M \csc^2\left(\frac{\pi}{M}\right) \end{aligned} \tag{B.14}$$

This completes the proof.

C. APPENDIX C

C.1. Derivation of Cross Moment-of-Inertia (5.2)

Suppose a planar array is given with coordinates as in (3.1). And then suppose we add new sensors and update the coordinates as in (5.1).

Mean of updated coordinates,

$$\mu_{\mathbf{x}^{(1)}} = \frac{\mathbf{x}^{(1)}\mathbf{1}_{M^{(1)}}^T}{M^{(1)}} = \frac{M\mu_{\mathbf{x}} + \zeta_x}{M^{(1)}} \tag{C.1}$$

$$\mu_{\mathbf{y}^{(1)}} = \frac{\mathbf{y}^{(1)}\mathbf{1}_{M^{(1)}}^T}{M^{(1)}} = \frac{M\mu_{\mathbf{y}} + \zeta_y}{M^{(1)}} \tag{C.2}$$

The cross moment-of-inertia between updated $\mathbf{x}^{(1)}$ and $\mathbf{y}^{(1)}$ coordinates is,

$$\begin{aligned}
I_{xy}^{(1)} &= \left(\mathbf{x}^{(1)} - \mu_{\mathbf{x}^{(1)}}\mathbf{1}_{M^{(1)}}\right)\left(\mathbf{y}^{(1)} - \mu_{\mathbf{y}^{(1)}}\mathbf{1}_{M^{(1)}}\right)^T \\
&= \left(x_1 - \mu_{\mathbf{x}^{(1)}}\right)\left(y_1 - \mu_{\mathbf{y}^{(1)}}\right) + \dots \\
&+ \left(x_M - \mu_{\mathbf{x}^{(1)}}\right)\left(y_M - \mu_{\mathbf{y}^{(1)}}\right) + \left(\zeta_x - \mu_{\mathbf{x}^{(1)}}\right)\left(\zeta_y - \mu_{\mathbf{y}^{(1)}}\right) \\
&= x_1y_1 - x_1\mu_{\mathbf{y}^{(1)}} - y_1\mu_{\mathbf{x}^{(1)}} + \mu_{\mathbf{x}^{(1)}}\mu_{\mathbf{y}^{(1)}} + \dots + x_My_M \\
&- x_M\mu_{\mathbf{y}^{(1)}} - y_M\mu_{\mathbf{x}^{(1)}} + \mu_{\mathbf{x}^{(1)}}\mu_{\mathbf{y}^{(1)}} + \zeta_x\zeta_y - \zeta_x\mu_{\mathbf{y}^{(1)}} \\
&- \zeta_y\mu_{\mathbf{x}^{(1)}} + \mu_{\mathbf{x}^{(1)}}\mu_{\mathbf{y}^{(1)}} \\
&= \mathbf{x}\mathbf{y}^T - \mu_{\mathbf{y}^{(1)}}\mathbf{x}\mathbf{1}_M^T - \mu_{\mathbf{x}^{(1)}}\mathbf{y}\mathbf{1}_M^T + M^{(1)}\mu_{\mathbf{x}^{(1)}}\mu_{\mathbf{y}^{(1)}} \\
&+ \zeta_x\zeta_y - \zeta_x\mu_{\mathbf{y}^{(1)}} - \zeta_y\mu_{\mathbf{x}^{(1)}}
\end{aligned} \tag{C.3}$$

Substitute (C.1) and (C.2) into (C.3), and recall (3.13) as $\mathbf{x}\mathbf{1}_M^T = M\mu_{\mathbf{x}}$, thus,

$$
\begin{aligned}
I_{xy}^{(1)} &= \mathbf{x}\mathbf{y}^T - \frac{M\mu_{\mathbf{y}} + \zeta_y}{M^{(1)}} M\mu_{\mathbf{x}} - \frac{M\mu_{\mathbf{x}} + \zeta_x}{M^{(1)}} M\mu_{\mathbf{y}} + M^{(1)} \frac{M\mu_{\mathbf{x}} + \zeta_x}{M^{(1)}} \frac{M\mu_{\mathbf{y}} + \zeta_y}{M^{(1)}} \\
&+ \zeta_x\zeta_y - \zeta_x \frac{M\mu_{\mathbf{y}} + \zeta_y}{M^{(1)}} - \zeta_y \frac{M\mu_{\mathbf{x}} + \zeta_x}{M^{(1)}} \\
&= \mathbf{x}\mathbf{y}^T - \frac{M^2\mu_{\mathbf{x}}\mu_{\mathbf{y}}}{M^{(1)}} - \frac{M\mu_{\mathbf{x}}\zeta_y}{M^{(1)}} - \frac{M^2\mu_{\mathbf{x}}\mu_{\mathbf{y}}}{M^{(1)}} \\
&- \frac{M\mu_{\mathbf{y}}\zeta_x}{M^{(1)}} + \frac{M^2\mu_{\mathbf{x}}\mu_{\mathbf{y}}}{M^{(1)}} + \frac{M\mu_{\mathbf{x}}\zeta_y}{M^{(1)}} + \frac{M\mu_{\mathbf{y}}\zeta_x}{M^{(1)}} \\
&+ \frac{\zeta_x\zeta_y}{M^{(1)}} + \zeta_x\zeta_y - \frac{M\mu_{\mathbf{y}}\zeta_x}{M^{(1)}} - \frac{\zeta_x\zeta_y}{M^{(1)}} - \frac{M\mu_{\mathbf{x}}\zeta_y}{M^{(1)}} - \frac{\zeta_x\zeta_y}{M^{(1)}} \\
&= \mathbf{x}\mathbf{y}^T + \frac{M}{M^{(1)}}\zeta_x\zeta_y - \frac{M^2}{M^{(1)}}\mu_{\mathbf{x}}\mu_{\mathbf{y}} - \frac{M}{M^{(1)}}\mu_{\mathbf{y}}\zeta_x - \frac{M}{M^{(1)}}\mu_{\mathbf{x}}\zeta_y
\end{aligned}
\tag{C.4}
$$

This completes the proof.

C.2. Derivation of Auto Moment-of-Inertia (5.8)

The auto moment-of-inertia of $\mathbf{x}^{(2)}$, is,

$$
\begin{aligned}
I_{xx}^{(2)} &= \|\mathbf{x}^{(2)} - \mu_{\mathbf{x}^{(2)}} \mathbf{1}_{M^{(2)}}\|^2 \\
&= \left(x_1 - \mu_{\mathbf{x}^{(2)}}\right)^2 + \left(x_2 - \mu_{\mathbf{x}^{(2)}}\right)^2 + \cdots + \left(x_M - \mu_{\mathbf{x}^{(1)}}\right)^2 \\
&+ \left(\zeta_x - \mu_{\mathbf{x}^{(2)}}\right)^2 + N\left(d_x - \mu_{\mathbf{x}^{(2)}}\right)^2 \\
&= x_1^2 + x_2^2 + \cdots + x_M^2 + \zeta_x^2 + N d_x^2 \\
&- 2\mu_{\mathbf{x}^{(2)}}^2 \underbrace{\left(x_1 + x_2 \ldots x_M + \zeta_x + N d_x\right)}_{M^{(2)}\mu_{\mathbf{x}^{(2)}}^2} + M^{(2)}\mu_{\mathbf{x}^{(2)}}^2 \\
&= \|\mathbf{x}^{(1)}\|^2 + N d_x^2 - M^{(2)}\mu_{\mathbf{x}^{(2)}}^2
\end{aligned}
\tag{C.5}
$$

Substituting (5.11) into (C.5) yields,

$$
I_{xx}^{(2)} = \frac{M^{(1)}N}{M^{(2)}} {d_x}^2 - \frac{{M^{(1)}}^2}{M^{(2)}} \mu_{\mathbf{x}^{(1)}}^2 - \frac{2M^{(1)}N}{M^{(2)}} \mu_{\mathbf{x}^{(1)}} d_x + \|\mathbf{x}^{(1)}\|^2 \tag{C.6}
$$

This completes the proof. $I_{yy}^{(1)}$ and $I_{zz}^{(1)}$ can be obtained in the same way.

C.3. Sensor Array Coordinates for Chapter 5

Table C.1: The Coordinates of Sensors in Terms of the wavelength (λ).

		Planar array sensors (●)					Added sensor(♦)	
Arrays		*1st*	*2nd*	*3rd*	*4th*	*5th*	*6th*	*7th*
	x	-1.00	-0.50	0.00	0.50	1.00	0.00	0.00
3-D	y	0.00	0.00	0.00	0.00	0.00	-1,32	-1,32
ULA	z	0.00	0.00	0.00	0.00	0.00	1,11	-1,11
	x	0.42	0.13	-0.34	-0.34	0.13	0.00	0.00
3-D	y	0.00	0.40	0.25	-0.25	-0.40	0.00	0.00
UCA	z	0.00	0.00	0.00	0.00	0.00	-0.47	0.47
	x	-0.46	-0.23	0.00	0.23	0.46	0.00	0.00
3-D	y	0.88	0.44	0.00	0.44	0.88	0.53	0.53
V	z	0.00	0.00	0.00	0.00	0.00	-0.52	0.52
						(■)	(♦)	(♦)
	x	0.50	0.00	-0.50	-0.25	0.488	0.047	0.047
3-D	y	-1.00	0.00	-0.50	-1.00	-0.27	-0.526	-0.526
Arb.	z	0.00	0.00	0.00	0.00	0.00	-0.628	0.628

C.4. Optimum 2-D Isotropic Volumetric Array Design Algorithm

Algorithm 1: Pseudo-code for the proposed algorithm

Phase 1: Check cross moment-of-inertia between *x* and *y* coordinates
Input: $\mathbf{x},\ \mathbf{y},\ \mathbf{z},\ M$
Output: $\mathbf{x}^{(1)},\ \mathbf{y}^{(1)},\ \mathbf{z}^{(1)},\ M^{(1)}$
if $I_{xy} = 0$ **then**
    $\mathbf{x}^{(1)} = \mathbf{x},\ \mathbf{y}^{(1)} = \mathbf{y},\ \mathbf{z}^{(1)} = \mathbf{z},\ M^{(1)} = M$
    go to **Phase 2**
    else
        Find the optimum (ζ_x, ζ_y) using (5.5)
        Update sensor coordinates (5.1) and other parameters (5.2), (5.3)

Phase 2: Equate auto moment-of-inertia of coordinates
Input: $\mathbf{x}^{(1)},\ \mathbf{y}^{(1)},\ \mathbf{z}^{(1)},\ M^{(1)},\ N$
Output: $\mathbf{x}^{(2)},\ \mathbf{y}^{(2)},\ \mathbf{z}^{(2)},\ M^{(2)}$
if $I_{xx}^{(1)} \neq I_{yy}^{(1)} \neq I_{zz}^{(1)}$ **then**
    Find the largest auto moment-of-inertia via (5.6)
    Solve (5.12) to find d_x, d_y, and d_z
    Update sensor coordinates (5.7) and other parameters (5.8)-(5.11)

REFERENCES

[1] H. Krim and M. Viberg, "Two decades of array signal processing research: the parametric approach," *IEEE Signal Processing Magazine*, vol. 13, no. 4, pp. 67–94, 1996.

[2] B. Friedlander, "Wireless direction-finding fundamentals," in *Classical and Modern Direction-of-Arrival Estimation* (T. E. Tuncer and B. Friedlander, eds.), pp. 1 – 51, Boston: Academic Press, 2009.

[3] S. Asgari, A. M. Ali, T. C. Collier, Y. Yao, R. E. Hudson, K. Yao, and C. E. Taylor, "Theoretical and experimental study of DOA estimation using AML algorithm for an isotropic and non-isotropic 3D array," in *Advanced Signal Processing Algorithms, Architectures, and Implementations XVII* (F. T. Luk, ed.), vol. 6697, pp. 172 – 183, International Society for Optics and Photonics, SPIE, 2007.

[4] L. Wan, G. Han, L. Shu, S. Chan, and T. Zhu, "The application of doa estimation approach in patient tracking systems with high patient density," *IEEE Transactions on Industrial Informatics*, vol. 12, pp. 2353–2364, Dec 2016.

[5] S. Tonetti, M. Hehn, S. Lupashin, and R. D'Andrea, "Distributed control of antenna array with formation of uavs," *IFAC Proceedings Volumes*, vol. 44, no. 1, pp. 7848 – 7853, 2011. 18th IFAC World Congress.

[6] J. Zhao, F. Gao, Q. Wu, S. Jin, Y. Wu, and W. Jia, "Beam tracking for uav mounted satcom on-the-move with massive antenna array," *IEEE Journal on Selected Areas in Communications*, vol. 36, pp. 363–375, Feb 2018.

[7] D. Fan, F. Gao, B. Ai, G. Wang, Z. Zhong, Y. Deng, and A. Nallanathan, "Channel estimation and self-positioning for uav swarm," *IEEE Transactions on Communications*, vol. 67, pp. 7994–8007, Nov 2019.

[8] Ülkü Baysal and R. L. Moses, "On the geometry of isotropic arrays," *IEEE Trans. Signal Process.*, vol. 51, pp. 1469–1478, 2003.

[9] H. L. V. Trees, *Optimum Array Processing: Part IV of Detection, Estimation, and Modulation Theory*. New York: Wiley-Interscience, 2002.

[10] Ülkü Baysal and R. L. Moses, "Optimal array geometries for wideband doa estimation," in *Proceedings of the MSS284 Meeting on Battlefield Acoustic and Seismic Sensors*, (Laurel, MD), pp. 1–12, Oct. 2001.

[11] R. O. Nielsen, "Azimuth and elevation angle estimation with a three-dimensional array," *IEEE Journal of Oceanic Engineering*, vol. 19, no. 1, pp. 84–86, 1994.

[12] F. Harabi, A. Gharsallah, and S. Marcos, "Three-dimensional antennas array for the estimation of direction of arrival," *Microwaves, Antennas and Propagation, IET*, vol. 3, pp. 843 – 849, Sept. 2009.

[13] K.-C. Tan, K.-C. Ho, and A. Nehorai, "Linear independence of steering vectors of an electromagnetic vector sensor," *IEEE Trans. Signal Process.*, vol. 44, pp. 3099–3107, 1996.

[14] C. Tan, S. Foo, M. Beach, and A. Nix, "Ambiguity in music and esprit for direction of arrival estimation," *Electronics Letters*, vol. 38, pp. 1598–1600(2), November 2002.

[15] H. Gazzah and S. Marcos, "Analysis and design of (non-)isotropic arrays for 3d direction finding," *IEEE/SP 13th Workshop on Statistical Signal Processing, 2005*, pp. 491–496, 2005.

[16] E. C. Jacobs and E. W. Ralston, "Ambiguity resolution in interferometry," *IEEE Transactions on Aerospace and Electronic Systems*, vol. AES-17, pp. 766–780, 1981.

[17] L. C. Godara and A. Cantoni, "Uniqueness and linear independence of steering vectors in array space," *The Journal of the Acoustical Society of America*, vol. 70, p. 467–475, 1981.

[18] M. Gavish and A. J. Weiss, "Array geometry for ambiguity resolution in direction finding," *IEEE Transactions on Antennas and Propagation*, vol. 44, no. 6, pp. 889–895, 1996.

[19] I. Gupta and A. Ksienski, "Effect of mutual coupling on the performance of adaptive arrays," *IEEE Transactions on Antennas and Propagation*, vol. 31, pp. 785–791, Sep. 1983.

[20] Z. Ye and C. Liu, "2-d doa estimation in the presence of mutual coupling," *IEEE Transactions on Antennas and Propagation*, vol. 56, pp. 3150–3158, Oct 2008.

[21] Z. Ye and C. Liu, "On the resiliency of music direction finding against antenna sensor coupling," *IEEE Transactions on Antennas and Propagation*, vol. 56, pp. 371–380, Feb 2008.

[22] A. M. Elbir, "Direction finding in the presence of direction-dependent mutual coupling," *IEEE Antennas and Wireless Propagation Letters*, vol. 16, pp. 1541–1544, 2017.

[23] H. Unz, "Linear arrays with arbitrarily distributed elements," *IRE Transactions on Antennas and Propagation*, vol. 8, no. 2, pp. 222–223, 1960.

[24] B. P. Kumar and G. R. Branner, "Design of unequally spaced arrays for performance improvement," *IEEE Transactions on Antennas and Propagation*, vol. 47, no. 3, pp. 511–523, 1999.

[25] B. P. Kumar and G. R. Branner, "Generalized analytical technique for the synthesis of unequally spaced arrays with linear, planar, cylindrical or spherical geometry," *IEEE Transactions on Antennas and Propagation*, vol. 53, no. 2, pp. 621–634, 2005.

[26] A. Manikas, *Differential Geometry in Array Processing*, pp. 81–83. London, UK: Imperial College Press, 2004.

[27] M. Lin and Y. Luxi, "Reply to the comments on "blind calibration and doa estimation with uniform circular arrays in the presence of mutual coupling"," vol. 5, pp. 568–569, 2006.

[28] A. Sleiman and A. Manikas, "The impact of sensor positioning on the array manifold," *IEEE Transactions on Antennas and Propagation*, vol. 51, pp. 2227–2237, Sep. 2003.

[29] Y. Hua, T. K. Sarkar, and D. D. Weiner, "An l-shaped array for estimating 2-d directions of wave arrival," *IEEE Transactions on Antennas and Propagation*, vol. 39, pp. 143–146, Feb 1991.

[30] T. Filik and T. E. Tuncer, "Uniform and nonuniform v-shaped isotropic planar arrays," in *2008 5th IEEE Sensor Array and Multichannel Signal Processing Workshop*, pp. 99–103, 2008.

[31] T. Filik and T. E. Tuncer, "Uniform and nonuniform v-shaped planar arrays for 2-d direction-of-arrival estimation," *Radio Science*, vol. 44, no. 5, pp. 1–12, 2009.

[32] H. Gazzah and S. Marcos, "Cramer-rao bounds for antenna array design," *IEEE Transactions on Signal Processing*, vol. 54, pp. 336–345, 2006.

[33] H. Gazzah and K. Abed-Meraim, "Optimum ambiguity-free directional and omnidirectional planar antenna arrays for doa estimation," *IEEE Transactions on Signal Processing*, vol. 57, pp. 3942–3953, 2009.

[34] N. Tayem and H. M. Kwon, "L-shape 2-dimensional arrival angle estimation with propagator method," *IEEE Transactions on Antennas and Propagation*, vol. 53, pp. 1622–1630, May 2005.

[35] C. A. Balanis, *Antenna Theory: Analysis and Design.* Wiley-Interscience, 2016.

[36] C. P. Mathews and M. D. Zoltowski, "Eigenstructure techniques for 2-d angle estimation with uniform circular arrays," *IEEE Trans. Signal Process.*, vol. 42, pp. 2395–2407, 1994.

[37] M. D. Zoltowski, M. Haardt, and C. P. Mathews, "Closed-form 2-d angle estimation with rectangular arrays in element space or beamspace via unitary esprit," *IEEE Trans. Signal Process.*, vol. 44, pp. 316–328, 1996.

[38] R. Goossens and H. Rogier, "A hybrid uca-rare/root-music approach for 2-d direction of arrival estimation in uniform circular arrays in the presence of mutual coupling," *IEEE Transactions on Antennas and Propagation*, vol. 55, pp. 841–849, 2007.

[39] T. Filik and T. E. Tuncer, “A fast and automatically paired 2-d direction-of-arrival estimation with and without estimating the mutual coupling coefficients,” *Radio Science*, vol. 45, pp. 1–14, June 2010.

[40] T. Filik, T. E. Tuncer, and T. K. Yasar, “Design of v-shaped array geometry,” in *2007 IEEE 15th Signal Processing and Communications Applications*, pp. 1–4, 2007.

[41] D. T. Vu, A. Renaux, R. Boyer, and S. Marcos, “A cramér rao bounds based analysis of 3d antenna array geometries made from ula branches,” *Multidimensional Systems and Signal Processing*, vol. 24, pp. 121–155, 2013.

[42] D. T. Vu, A. Renaux, R. Boyer, and S. Marcos, “Performance analysis of 2d and 3d antenna arrays for source localization,” in *2010 18th European Signal Processing Conference*, pp. 661–665, Aug. 2010.

[43] U. Oktel and R. L. Moses, “A bayesian approach to array geometry design,” *IEEE Transactions on Signal Processing*, vol. 53, no. 5, pp. 1919–1923, 2005.

[44] A. Manikas, A. Sleiman, and I. Dacos, “Manifold studies of nonlinear antenna array geometries,” *IEEE Transactions on Signal Processing*, vol. 49, pp. 497–506, March 2001.

[45] M. Hawkes and A. Nehorai, “Effects of sensor placement on acoustic vector-sensor array performance,” *IEEE Journal of Oceanic Engineering*, vol. 24, no. 1, pp. 33–40, 1999.

[46] H. Chen, X. Li, and Z. Zhuang, “Antenna geometry conditions for mimo radar with uncoupled direction estimation,” *IEEE Transactions on Antennas and Propagation*, vol. 60, pp. 3455–3465, 2012.

[47] X. Wang, E. Aboutanios, and M. G. Amin, “Adaptive array thinning for enhanced doa estimation,” *IEEE Signal Processing Letters*, vol. 22, pp. 799–803, 2015.

[48] F. Keskin and T. Filik, “Volumetric v-shaped array design for 2-d isotropic doa estimation,” in *2018 26th Signal Processing and Communications Applications Conference (SIU)*, pp. 1–4, May 2018.

[49] F. Keskin and T. Filik, "3d v-shaped array design for fully isotropic azimuth and elevation angle estimation," in *2019 27th Signal Processing and Communications Applications Conference (SIU)*, pp. 1–4, April 2019.

[50] F. Keskin and T. Filik, "Extension of centrosymmetric planar arrays for both azimuth and elevation isotropic (2-d) doa estimation.," *(to be submitted)*, 2021.

[51] F. Keskin and T. Filik, "An optimum volumetric array design approach for both azimuth and elevation isotropic doa estimation," *IEEE Access*, vol. 8, pp. 183903–183912, 2020.

[52] F. Keskin and T. Filik, "Isotropic and directional doa estimation of the target by uav swarm-based 3-d antenna array," in *2020 4th International Symposium on Multidisciplinary Studies and Innovative Technologies (ISMSIT)*, pp. 1–7, Oct 2020.

[53] R. Schmidt, *A Signal Subspace Approach to Multiple Emitter Location and Spectral Estimation*. phdthesis, 1981.

[54] A. J. Weiss and B. Friedlander, "On the cramer-rao bound for direction finding of correlated signals," *IEEE Trans. Signal Process.*, vol. 41, pp. 495–498, 1993.

[55] R. O. Schmidt, "Multiple emitter location and signal parameter estimation," *IEEE Transactions on Antennas and Propagation*, vol. 34, no. 3, pp. 276–280, 1986.

[56] M. Koivisto, A. Hakkarainen, M. Costa, P. Kela, K. Leppanen, and M. Valkama, "High-efficiency device positioning and location-aware communications in dense 5g networks," *IEEE Communications Magazine*, vol. 55, pp. 188–195, Aug 2017.

[57] M. M. Azari, H. Sallouha, A. Chiumento, S. Rajendran, E. Vinogradov, and S. Pollin, "Key technologies and system trade-offs for detection and localization of amateur drones," *IEEE Communications Magazine*, vol. 56, pp. 51–57, 2018.

[58] I. Guvenc, O. Ozdemir, Y. Yapici, H. Mehrpouyan, and D. Matolak, "Detection, localization, and tracking of unauthorized uas and jammers," in *2017 IEEE/AIAA 36th Digital Avionics Systems Conference (DASC)*, pp. 1–10, Sep. 2017.

[59] X. Wang, G. Tan, Y. Dai, F. Lu, and J. Zhao, "An optimal guidance strategy for moving-target interception by a multirotor unmanned aerial vehicle swarm," *IEEE Access*, vol. 8, pp. 121650–121664, 2020.

[60] A. Dogandzic and A. Nehorai, "Cramer-rao bounds for estimating range, velocity, and direction with an active array," *IEEE Transactions on Signal Processing*, vol. 49, pp. 1122–1137, June 2001.

[61] R. Fitzpatrick, *Newtonian Dynamics*, ch. Rigid Body Rotation, pp. 106–107. Lulu, fourth ed., Jan. 2011.

[62] B. Friedlander and A. J. Weiss, "Direction finding in the presence of mutual coupling," *IEEE Transactions on Antennas and Propagation*, vol. 39, pp. 273–284, March 1991.

[63] R. S. Adve and T. K. Sarkar, "Compensation for the effects of mutual coupling on direct data domain adaptive algorithms," *IEEE Transactions on Antennas and Propagation*, vol. 48, pp. 86–94, Jan 2000.

[64] M. Wang, X. Ma, S. Yan, and C. Hao, "An autocalibration algorithm for uniform circular array with unknown mutual coupling," *IEEE Antennas and Wireless Propagation Letters*, vol. 15, pp. 12–15, 2016.

[65] M. Eric, A. Zejak, and M. Obradović, "Ambiguity characterization of arbitrary antenna array: type i ambiguity," in *1998 IEEE 5th International Symposium on Spread Spectrum Techniques and Applications - Proceedings. Spread Technology to Africa (Cat. No.98TH8333)*, vol. 2, pp. 399–403 vol.2, 1998.

[66] T. Filik and T. E. Tuncer, "2-d doa estimation in case of unknown mutual coupling for multipath signals," *Multidimensional Systems and Signal Processing*, vol. 27, pp. 69–86, 2016.

[67] J. Autenrieb, N. Strawa, H. Shin, and J. Hong, "A mission planning and task allocation framework for multi-uav swarm coordination," in *2019 Workshop on Research, Education and Development of Unmanned Aerial Systems (RED UAS)*, pp. 297–304, 2019.

[68] U. Zengin and A. Dogan, "Real-time target tracking for autonomous uavs in adversarial environments: A gradient search algorithm," *IEEE Transactions on Robotics*, vol. 23, pp. 294–307, April 2007.

[69] M. R. Brust, G. Danoy, P. Bouvry, D. Gashi, H. Pathak, and M. P. Gonçalves, "Defending against intrusion of malicious uavs with networked uav defense swarms," in *2017 IEEE 42nd Conference on Local Computer Networks Workshops (LCN Workshops)*, pp. 103–111, Oct 2017.

[70] P. Chandhar and E. G. Larsson, "Massive mimo for connectivity with drones: Case studies and future directions," *IEEE Access*, vol. 7, pp. 94676–94691, 2019.

[71] A. Tahir, J. Böling, M.-H. Haghbayan, H. T. Toivonen, and J. Plosila, "Swarms of unmanned aerial vehicles — a survey," *Journal of Industrial Information Integration*, vol. 16, p. 100106, 2019.

[72] X. Zhang and M. Ali, "A bean optimization-based cooperation method for target searching by swarm uavs in unknown environments," *IEEE Access*, vol. 8, pp. 43850–43862, 2020.

[73] D. I. Koutras, A. C. Kapoutsis, and E. B. Kosmatopoulos, "Autonomous and cooperative design of the monitor positions for a team of uavs to maximize the quantity and quality of detected objects," *IEEE Robotics and Automation Letters*, vol. 5, pp. 4986–4993, July 2020.

[74] S. Shakoor, Z. Kaleem, D. Do, O. A. Dobre, and A. Jamalipour, "Joint optimization of uav 3d placement and path loss factor for energy efficient maximal coverage," *IEEE Internet of Things Journal*, pp. 1–1, 2020.

[75] R. Jonker and A. Volgenant, "A shortest augmenting path algorithm for dense and sparse linear assignment problems," *Computing*, vol. 38, p. 325–340, Nov. 1987.

CURRICULUM VITAE

Name:	Fesih Keskin
Foreign Languages:	English

Education

- PhD (2014–2021), Eskişehir Technical University, Electrical and Electronics Engineering
- MSc (2011–2014), Anadolu University, Electrical and Electronics Engineering
- BSc (2005–2009), Fırat University, Electrical and Electronics Engineering

Employment

- Research Assistant (2018–), Iğdır University
- Research Assistant (2011–2018), Eskişehir Technical University
- Research Assistant (2010–2011), Iğdır University

Publications

- F. Keskin and T. Filik, "An optimum volumetric array design approach for both azimuth and elevation isotropic doa estimation," *IEEE Access*, vol. 8, pp. 183 903–183 912, 2020, ISSN: 2169-3536. DOI: `10.1109/ACCESS.2020.3028929`
- F. Keskin and T. Filik, "Extension of centrosymmetric planar arrays for both azimuth and elevation isotropic (2-d) doa estimation.," *(to be submitted)*, 2021
- F. Keskin and T. Filik, "Isotropic and directional doa estimation of the target by uav swarm-based 3-d antenna array," in *2020 4th International Symposium on Multidisciplinary Studies and Innovative Technologies (ISMSIT)*, 2020, pp. 1–7. DOI: `10.1109/ISMSIT50672.2020.9254341`
- F. Keskin and T. Filik, "3d v-shaped array design for fully isotropic azimuth and elevation angle estimation," in *2019 27th Signal Processing and Communications Applications Conference (SIU)*, 2019, pp. 1–4. DOI: `10.1109/SIU.2019.8806470`
- F. Keskin and T. Filik, "Volumetric v-shaped array design for 2-d isotropic doa estimation," in *2018 26th Signal Processing and Communications Applications Conference (SIU)*, 2018, pp. 1–4. DOI: `10.1109/SIU.2018.8404725`